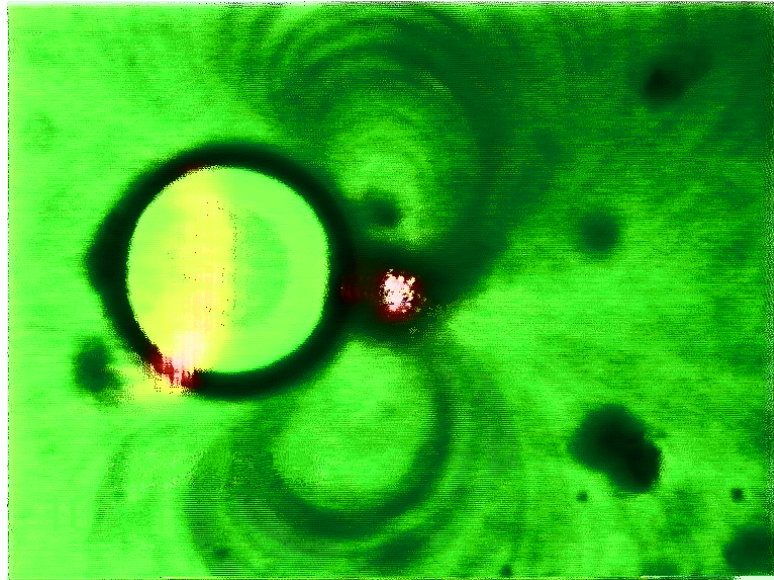# HEATING EFFECTS
IN
OPTICAL TRAPPING

BY
DOMINIC BERRY

Honours Thesis
Department of Physics
The University of Queensland
June 1997

Acknowledgments

Firstly I would like to thank my supervisors, Assoc. Prof. Halina Rubinsztein-Dunlop and Assoc. Prof. Norman Heckenberg, for their help and supervision during the year, and for their help with the drafts of this text.

Huge thanks to Dr Rodney McDuff for his invaluable assistance with digitising the images. Thanks also go to Marlies Friese for her help with the operation of the laser tweezers apparatus, to Malcolm Brimblecombe and Martin Nicholls for their help with the use of Fraser and FIDAP, and to the staff of the physics office for their help with obtaining toner samples.

I would also like to thank the staff of the mechanical workshop for their help with constructing some of the equipment, and the staff of the electrical workshop for providing the equipment required for some of the measurements. Also the chemistry store supplied the chemicals, and Steward supplied the ferromagnetic powders.

Abstract

The effects of superheating of liquids and Marangoni (surface tension driven) convection associated with the laser tweezers apparatus are systematically investigated for the first time. Due to the small size of the heated region, absorbing particles can be heated to well above the normal boiling point of the surrounding liquid. The limits of superheat in various liquids were investigated through the melting of photocopier toner and through the Curie points of ferrite powders. It was found that the temperatures at bubble formation in all liquids investigated were consistent with fluctuation nucleation theory. Also the observed temperature rises were of the same order of magnitude as the theoretical values, but were fairly uniformly lower than predicted due to reflection.

When bubbles are formed there are strong surface tension driven convection currents. The pattern of these convection currents was observed using sub-micron size carbon black particles, and the shape of the convection currents was theoretically investigated by numerical simulations. Numerical estimates of the effect of thermocapillary bubble migration are made, and it is shown to be a very powerful means of trapping bubbles. Also the small thermal convection currents in the absence of a bubble were investigated through numerical simulations.

Contents

Chapter 1: Introduction

Optical tweezers, or the single-beam gradient force optical trap, was first demonstrated by Ashkin *et al* in 1986 [1]. The trap consists of a single laser beam, tightly focussed to a spotsize on the order of an optical wavelength using a high numerical aperture (N.A.) microscope objective lens. Since the discovery that live cells and viruses can be trapped without apparent damage [2], optical tweezers has found many applications in biology, such as manipulation of cells [3] and chromosomes [4].

  Ashkin *et al* [1] used a TEM$_{00}$ (Gaussian) laser beam to trap high refractive index transparent spheres in three dimensions. By scanning a Gaussian laser beam, low index transparent spheres have been trapped in three dimensions, and absorbing particles have been trapped in two dimensions [5]. Gauss-Laguerre (TEM*$_{01}$) beams were first used by Sato *et al* in 1991 [6] for more efficient trapping of high index transparent spheres, and in 1995 He *et al* [7] demonstrated the two dimensional trapping of reflective and absorbing particles using a charge 3 Gauss-Laguerre (LG$_{03}$) beam. TEM*$_{01}$ beams have also been used for the three dimensional trapping of low index transparent spheres [8]. Recently it has been found that it is also possible to trap absorbing particles in two dimensions with a Gaussian beam [9, 10].

  Due to the highly focussed nature of the beam, the beam intensity at the focus is very high, even for relatively low power lasers, and it is therefore possible for quite substantial heating to take place. This is particularly significant in the case of biological materials, as even moderate heating can kill cells. Even for non-biological materials heating effects can be a problem, as bubble formation will disrupt trapping [11]. Also heating effects can be used, for example in the ablative modification of trapped particles [12].

  In this project various heating effects associated with the laser tweezers apparatus are investigated. In Chapter 2 the effect of bubble formation is investigated in detail. Due to the very small size of the region heated by the laser tweezers apparatus, bubble formation does not occur at the normal boiling temperature of the surrounding liquid, but at a higher temperature where bubbles can form spontaneously from thermal fluctuations. This is significant from the point of view of fundamental studies because superheating near the homogeneous nucleation temperature is possible without any of the precautions usually

required for superheating experiments, i.e. cleaning of the surfaces and purification of the liquid. It is also significant in practical applications because it means that higher powers can be used before bubble formation (around 4 times for water).

In Chapter 2 the temperature at bubble formation in various liquids is estimated both through the melting of toner and through the Curie points of ferromagnetic powders. The theoretical calculation of the nucleation rate is discussed, including the homogeneous nucleation rate and the heterogeneous nucleation rates at solid-liquid and liquid-liquid interfaces. The theoretical nucleation temperatures are shown to be consistent with the temperatures at bubble formation. Also the temperature distribution is calculated, and is used to estimate the power required for bubble formation.

In Chapter 3 convection effects are investigated. At the very small scales involved in the laser tweezers apparatus Marangoni (surface tension driven) convection is very strong. In Chapter 3 the Marangoni convection patterns are experimentally observed, and an attempt is made to reproduce these convection patterns theoretically. The surface tension driven convection exerts a force on the bubbles, and this is found to be a very effective means of trapping bubbles, which are normally difficult to trap due to their low refractive index. Also, a small amount of thermal convection is observed in the absence of a bubble. The theoretical thermal convection velocities are calculated, and found to be in order of magnitude agreement with those observed.

Chapter 2: Superheating

This study was prompted by reports that particles could be heated to well above the boiling point of the surrounding liquid without bubble formation by the laser tweezers apparatus. This chapter describes the various nucleation mechanisms for bubble formation, and the limits of superheat in various liquids are measured.

2.1 Apparatus

The single-beam optical gradient trap used in these experiments is based on that used by Cassius D'Helon [13]. Particles were observed using a phase-contrast microscope (Olympus CH2), where the same objective lens was used for both focussing the laser beam to produce the trap and viewing of the trapped particle. The laser beam was coupled to the objective through an opening in the side of the microscope, using two beam-steering mirrors and an IF550 beam-splitting mirror. The laser used is a 13 mW linearly polarised He-Ne laser (Uniphase, model 1135P) with a Gaussian profile.

 The lens used is a high numerical aperture (N.A.=1.3) phase contrast oil-immersion 100× objective (Olympus achromat PCD100×). The N.A. specified corresponds to a maximum convergence angle of 59° using immersion oil of refractive index n_{oil} = 1.5180. The power of the laser beam was controlled using a polarising filter. Recording of observations on video was made possible by the attachment of a CCD camera (Panasonic, model WV-CP410 or WV-CL350) to the microscope. The images taken using the camera were digitised using a Silicon Graphics Indy workstation.

2.2 Calibration Measurements

For quantitative investigation of superheating it is necessary to establish the absolute scale of the images and the absolute power of the laser light which is incident on the trapped particle. The relative scale of images can be determined using either the eyepiece micrometer, or by the

number of pixels in the digitised image. These can then be calibrated absolutely against a stage micrometer. It was found that each division on the eyepiece micrometer was equivalent to 1.11±0.01 μm. For the model WV-CP410 camera 121 pixels in the digitised images were equivalent to 10 μm, and for the model WV-CL350 camera 95 pixels were equivalent to 10 μm. Rough size measurements were made using the eyepiece micrometer, and when more accurate measurements were required these were made using the digitised image.

In order to determine the power that is delivered to the focus of the microscope, it is necessary to make measurements of the attenuation of the beam between the opening at the side of the microscope and the focus, and to make absolute measurements of the beam power. The reduction in power from the input beam to the focus is due to the imperfect reflectance of the IF550 filter (which is internal to the microscope), the imperfect transmittance of the microscope objective, and the reflection of light off the coverslip. In order to determine the proportion of the power at the focus it is not possible to simply put a detector at the focus, as the beam exiting the objective is highly divergent. This means that the detector does not absorb all the light, making readings highly inaccurate.

For this reason the method of Misawa *et al* [12] was used instead. A second 100× objective of the same type was mounted underneath the stage using the mount for the condenser, and special slides were constructed consisting of a plastic slide with a large hole drilled in the centre, and a coverslip glued over the hole. A drop of water was put on a slide and a coverslip was used in order to duplicate normal conditions as closely as possible.

The upper objective was brought to a position such that the focus was between the coverslips (the position was monitored by monitoring the reflections through the eyepieces), and the lower objective was adjusted so that a parallel beam exited the lower objective. No lenses were used to modify the He-Ne beam, but an iris was put very close to the opening at the side of the microscope and closed to the minimum possible radius. This avoids losses due to the light at the extremities of the beam not passing through the objective, which can be a problem for larger beam widths.

Let T_M be the reflectance of the IF550 filter, let T_O be the combined transmittance of the objective and the coverslip (which should be the same for both the upper and lower objectives), let T_{TOT} be the ratio of the power remaining after passing through the entire system, and let T_F be the ratio of the power at the focus. It is obvious that

$$T_F = T_M T_O \tag{2.1}$$

and
$$T_{TOT} = T_M T_O T_O \tag{2.2}$$

The quantities T_M and T_{TOT} can be determined by direct measurements, and in terms of these quantities T_F is

$$T_F = \sqrt{T_M T_{TOT}} \tag{2.3}$$

The power at the input to the side of the microscope and the power reflected off the IF550 filter were measured using a Newport digital power meter (model 815), and the results are given in table A.1 of appendix A. The Newport power meter is equipped with an attenuator, however this was not used as it can cause erratic readings. The reflectance taking into account all of the data is

$$T_M = 0.9542 \pm 0.0014$$

Similar measurements were made of the power input to the side of the microscope and the power passing through the lower objective, and the results are as given in table A.2 of appendix A. The average total transmittance is

$$T_{TOT} = 0.6781 \pm 0.0013$$

The total transmittance between the input at the side of the microscope and the focus is therefore

$$T_F = 0.8044 \pm 0.0012$$

Measurements of the laser power given in following sections were made using a Laserdyne Spectramet power meter (model MV-1) equipped with a model SPH-1 sensor head. The sensor head has a lens and diffuser which are removable, and all measurements were made with these removed. In order to make absolute measurements of the beam power, the Laserdyne Spectramet power meter was calibrated against a Scientech power meter (model 361-002) equipped with three model 360-001 sensor heads. The Scientech power meter operates by heating, and can be independently calibrated by passing a heating current through the head. A current was passed through the power meter and the current was measured using a Fluke true RMS multimeter (model 87), and the voltage was measured using another Fluke true RMS multimeter (model 86). Several measurements were made of the reading on the Scientech power meter simultaneously with the voltage and current. The Spectramet power meter was immediately calibrated against the Scientech power meter after each measurement.

In order to eliminate systematic errors in the detector heads, the calibration was repeated with each of the three heads. The results are as in tables A.3 and A.4 of appendix A. From these measurements, the ratio of the absorbed power to the indicated power for the three heads is

$$P_A/P_{D1} = 0.5016 \pm 0.0032$$

$$P_A/P_{D2} = 1.1440 \pm 0.0063$$

$$P_A/P_{D3} = 0.5233 \pm 0.0030$$

The subscript A is used for power absorbed by the head, the subscript D is used for the power registered on the Scientech power meter, and the subscripts 1, 2 and 3 are used for detector heads with serial numbers 3685, 989 and 3366 respectively. In the following the subscript L is used for the actual laser power, the subscript LS is used for the power registered by the Laserdyne Spectramet power meter, and the subscript F is used for the laser power at the focus.

The manual for the Scientech power meter gives the reflectivity of the absorbing plates as about 2%, so the ratio of the laser power to the detected power for the three heads is

$$P_L/P_{D1} = 0.5118 \pm 0.0033$$

$$P_L/P_{D2} = 1.1673 \pm 0.0064$$

$$P_L/P_{D3} = 0.5340 \pm 0.0030$$

The ratio of the power indicated by the Scientech power meter to the power indicated by the Laserdyne Spectramet power meter for the three heads is

$$P_{D1}/P_{LS} = 1.6091 \pm 0.0050$$

$$P_{D2}/P_{LS} = 0.6819 \pm 0.0033$$

$$P_{D3}/P_{LS} = 1.5018 \pm 0.0028$$

The ratio of the laser power to the power indicated by the Laserdyne Spectramet power meter as determined using each of the three heads is therefore

$$(P_L/P_{LS})_1 = 0.8235 \pm 0.0059$$

$$(P_L/P_{LS})_2 = 0.7960 \pm 0.0038$$

$$(P_L/P_{LS})_3 = 0.8019 \pm 0.0048$$

These calibrations for the three heads are not significantly different. The average of the results from each of the three heads is

$$P_L/P_{LS} = 0.8071 \pm 0.0084$$

The ratio of the power at the focus to the reading on the Laserdyne Spectramet power meter is therefore

$$P_F/P_{LS} = 0.6493 \pm 0.0068$$

This calibration is used to determine the power at the focus for all following power measurements.

In order to determine the total power absorbed by a particle, rather than the power at the

focus, it is necessary to determine the fraction of the beam power that passes through and around the particle. In order to measure this, the second objective was used underneath the microscope stage to collect the laser light passing through and around the particle. The powers passing through the second objective when the particle was in the beam, and when the particle was moved to the side, were measured with the Newport[*] or Laserdyne Spectramet power meter.

2.3 Experiment

In initial experiments it was observed that when trapping with a third order Gauss-Laguerre beam, particles of photocopier toner could be melted in water, and when using a Gaussian beam, particles of copper oxide could be melted in kerosene. Two dimensional trapping is possible with both Gaussian and Gauss-Laguerre beams [7, 9, 10], however it is not essential for observations, as the particles often adhere to the slide, and are not dislodged by the beam.

The melting point of copper oxide is 1326°C, and kerosene is a petroleum fraction and has a boiling point between 200°C and 250°C. Therefore if the copper oxide was being melted in kerosene it would have to be heated to more than 1000°C above the boiling point of the surrounding liquid. After more systematic testing it was found to be impossible to repeat the observations of the melting of copper oxide in kerosene. It was found, however, that if the slide was allowed to dry out, the copper oxide particles could be melted with a power at the focus of around 4 mW (an example of this is shown in figure 2.1). Therefore the early observations of the melting of copper oxide particles in kerosene can be attributed to drying of the slide.

The softening point for the toner given by the manufacturers was 180°C to 190°C, so the melting of the particles indicates that the toner particles were being heated to 80°C higher than the boiling point of the surrounding liquid. It was found that the toner particles could be melted without the production of bubbles with a third order Gauss-Laguerre beam, or with a Gaussian beam once the beam was attenuated to approximately the same intensity as the Gauss-Laguerre beam.

An example of a toner particle melted by a Gaussian beam in water is shown in figure 2.2. The power at the focus required to cause visible softening in the particle shown was

---

[*] This power meter was not calibrated as it was only used for measuring relative powers.
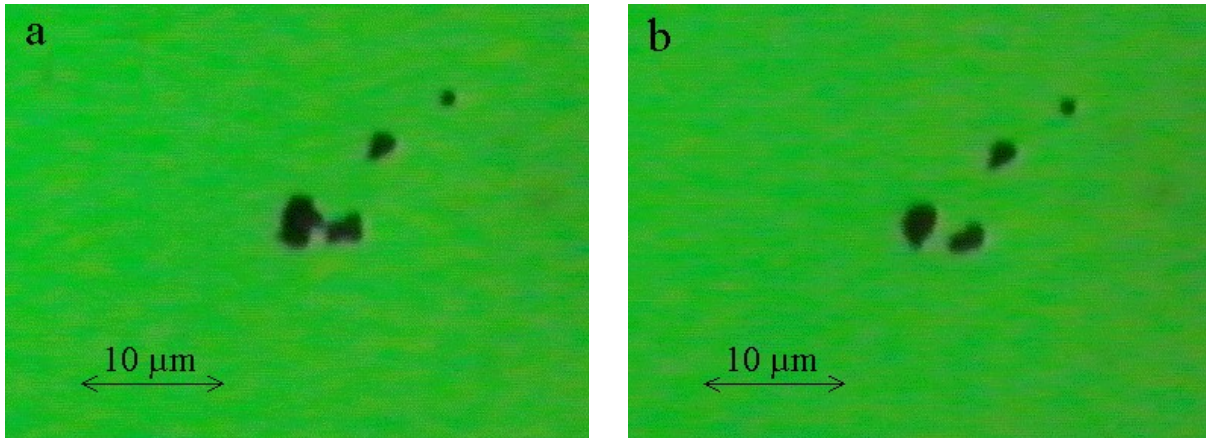
Figure 2.1: An example of a copper oxide particle melted by a Gaussian beam. The particle before it was passed through the beam is shown in (a), and the particle after melting is shown in (b). The power at the focus is 3.5 mW, and the proportion of the beam absorbed is approximately 86%.

1.24±0.05 mW. The diameter of the beam at the input to the side of the microscope was reduced using a 350 mm focal length lens and an iris. This prevents overfilling of the objective, which would result in an inaccurate measurement of the power at the focus.
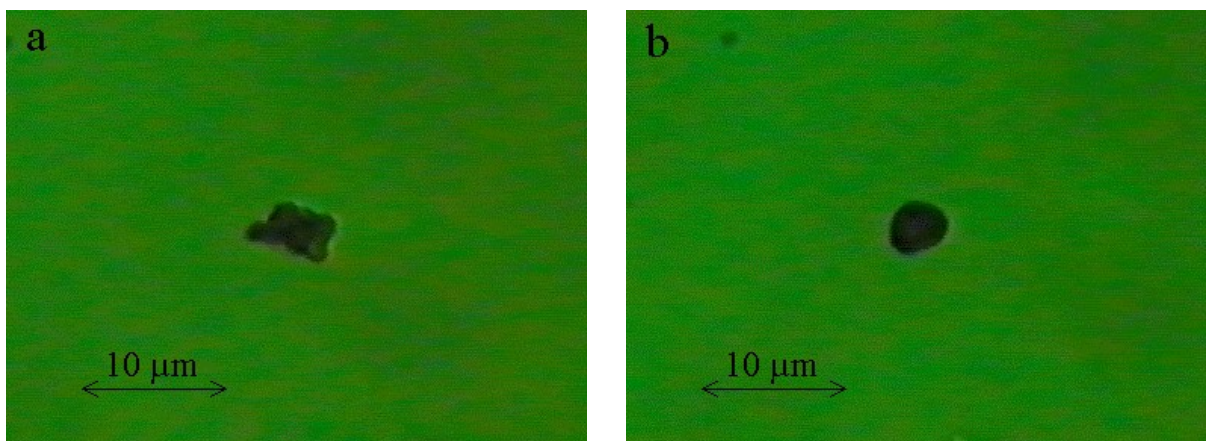

Figure 2.2: An example of a toner particle in water melted by a Gaussian beam. The particle before it was passed through the beam is shown in (a), and the particle after the power was increased sufficiently to cause softening and deformation is shown in (b).

The contributions to the uncertainty in the power are from the uncertainty in the calibration of the power meter and the random variation in the reading of the power meter, as well as the uncertainty in estimating the exact point at which point the softening becomes visible. At the power given above it was possible to partially melt most particles, almost independently of size. This appears to be due to the low thermal conductivity of the toner and the heating pattern, and will be discussed further in section 2.8.

The power required to produce bubbles tended to vary more than the power required for melting. The required power varied by 10% or 20%, and in some cases the power was much

higher, though this was probably because the focus was not directly on the particle, resulting in a smaller portion of the light being absorbed. An example of bubble formation where the power was at an intermediate value is shown in figure 2.3 (the bubble is the lighter region within the particle). This is the same particle as in figure 2.2, and the power required to produce a bubble was 2.73±0.05 mW. Note that this is about 2.2 times the power required to produce visible softening of the particle.
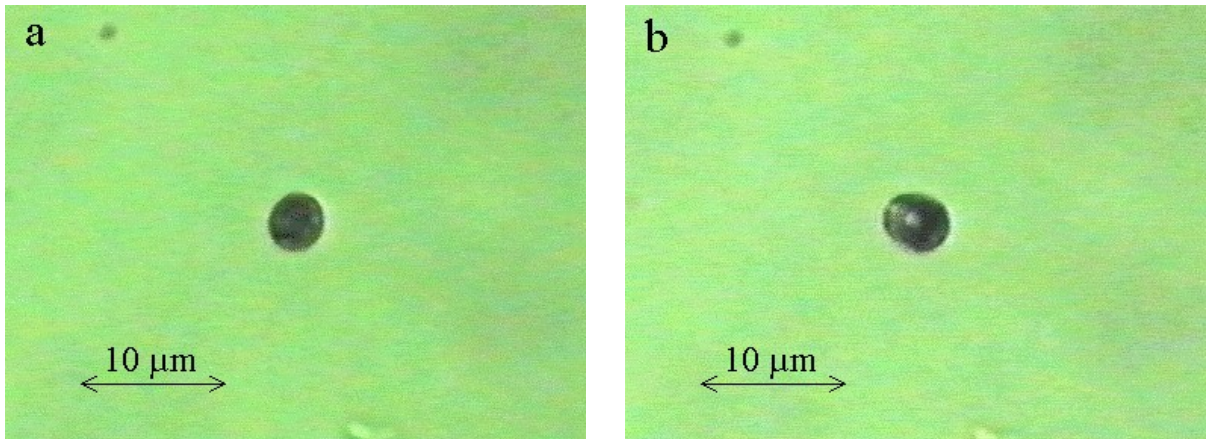

Figure 2.3: Bubble formation when heating with a Gaussian beam. The particle immediately before bubble formation is shown in (a), and the newly formed bubble is shown in (b).

The bubbles observed appeared to form inside the toner particles, as can be seen in figure 2.3. When the position of the beam was moved, the bubble followed the beam focus. Also, as the power was increased, the bubble grew larger than the original size of the toner particle, with a visible layer of toner on its surface. An example of this is shown in figure 2.4. It was observed that when the beam was removed from the particle the bubble tended to remain. This appears to be because the cooling is so rapid that there is no time for the bubble to collapse before the toner solidifies (order of magnitude calculations indicate a cooling time of a few microseconds).

The only conditions under which bubbles could be produced in the water, rather than in the interior of the toner, was when the beam was at maximum intensity (around 9 mW at the focus), and the beam was run quickly over the toner particles. Then small bubbles appeared in the water, and were quickly reabsorbed. If the beam intensity was slowly increased while focussed on a particle, this did not occur. This appears to be due to the distortion of the particle reducing the proportion of the beam absorbed and therefore reducing the heating possible.
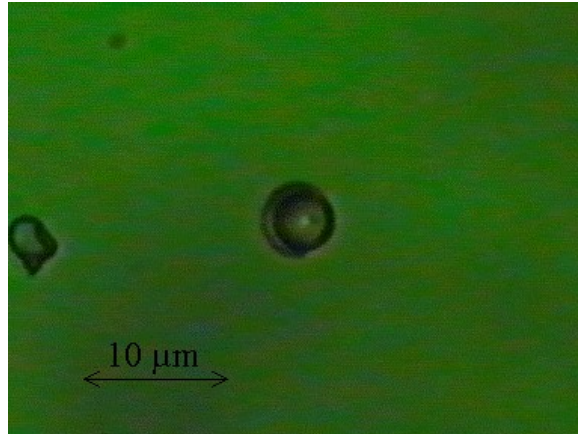
Figure 2.4: Large bubble inside the toner particle at high power.

As the power was increased above that required for bubble formation, the main effect was that the bubble inside the particle increased in size, but occasionally bubbles were observed that were of a qualitatively different type. Several bubbles were present simultaneously, and these bubbles appeared to bubble out into the water and be instantly absorbed (see figure 2.5). This behaviour seems to require a high power for a length of time. It is possible that the bubbles observed are due to gases produced by the decomposition of the toner at high temperatures.
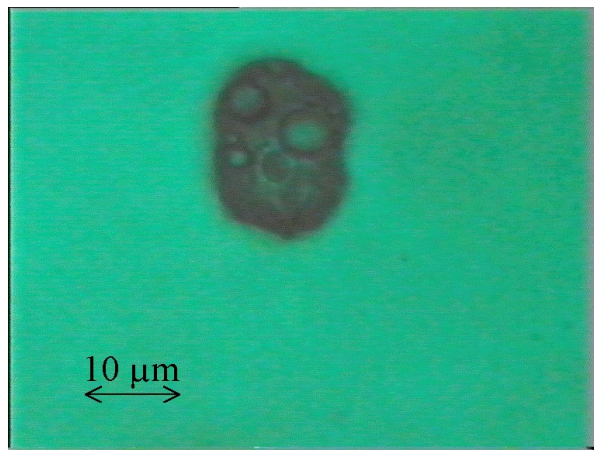
Figure 2.5: Possible decomposition of a toner particle. The power is 6.3 mW at the focus. This image has been processed to enhance the bubbles.

There was no significant difference between the observations using a Gaussian beam and those using a Gauss-Laguerre beam, provided the width of the Gaussian beam and the Gauss-Laguerre beam were about the same. Therefore most measurements were performed for the case of a Gaussian beam, as using a Gauss-Laguerre beam reduces the available power.

2.4 Measurement of Melting Point

In order to verify the melting temperature for the toner given by the manufacturers, the melting point was measured independently. Crude experiments indicated that the toner melted below the boiling point of water, so the toner was mixed in water, and the water was heated to a range of temperatures. The maximum temperature reached was monitored with a Tsuruga digital thermometer (model 3527). It was difficult to interpret the results, as the rounding of the particles changed very gradually with temperature, however the rounding appeared to occur between about 70°C and 80°C.

  This behaviour can be clarified by reference to the data given in [14]. The glass transition temperatures for the styrene acrylate copolymers used in toner resins range from about 60°C to 80°C. At the glass transition temperature polymers change from a solid to a very viscous liquid. It therefore appears that the temperature where the softening becomes visible must be near the glass transition temperature. The temperatures required for fixing of toner are in the range 140°C to 200°C, and so the melting temperatures listed for the toner were probably just the temperatures required for fixing.

  Note that because the power can be more than doubled between melting and the production of bubbles, the results still indicate that the toner particles are heated over the boiling point of water before bubble formation. In the example given in section 2.3, the power was increased by a factor of 2.2 before bubble formation, indicating that the particle is heated to between about 125°C and 145°C before bubble formation, which is still significantly above the melting point of water. This calculation assumes that the surface of the particle is at the melting point when softening of the particle becomes visible. This may not be the case, due to the uneven temperature distribution. This will be discussed further in section 2.8.

2.5 Homogeneous Nucleation

The reason that particles can be heated to temperatures far higher than the boiling point of the surrounding liquid without bubbles forming is that the normal boiling temperature is merely the temperature where the vapour pressure of the liquid matches the atmospheric pressure, and not the temperature where bubbles can form spontaneously in the interior of the liquid (homogeneous nucleation), or spontaneously at an interface (heterogeneous nucleation). For

normal boiling the primary mechanism of bubble nucleation is nucleation from pre-existing nuclei at the solid-liquid interface. There are microscopic pockets of air on the interface, and the liquid needs to be superheated only slightly above the boiling point for these small air pockets to expand from the vapour and produce large bubbles. If the heated region is very small, however, there will be no pre-existing nuclei for nucleation.

An order of magnitude estimate of the density of pre-existing nuclei can be made by reference to the experiments of Iida, Okuyama and Sakurai [15]. In their experiments a heating strip was used, and pre-existing nuclei could be detected because bubbles repeatedly appeared at the same locations in successive heat pulses. The dimensions of the strip were 0.25 mm by 0.1 mm, and there were only two sites where there were pre-existing nuclei. This corresponds to about one nucleus in every 10000 μm². Since the area being heated with the laser tweezers apparatus is on the order of one square micron, if we assume that the materials are similar to the same order of magnitude, there is only on the order of a 0.01% chance of there being a pre-existing nucleus. Therefore it is reasonable to ignore the possibility of pre-existing nuclei in interpreting the above observations.

Firstly the theory of homogeneous nucleation will be considered. The reason why the temperature required for homogeneous nucleation is so much greater than the boiling point is that bubbles require an internal pressure that is higher than the ambient pressure in order to expand the bubble against the resistance of surface tension, and as the radius goes to zero the extra pressure required rises to infinity. To see this, consider that the energy of a bubble of radius r is

$$
\begin{aligned}
E &= A\sigma - \left(P_n - P_L\right)V \\
&= 4\pi r^2\sigma - \tfrac{4}{3}\pi r^3\left(P_n - P_L\right)
\end{aligned}
\tag{2.4}
$$

where A and V are the surface area and volume of the bubble, σ is the surface tension and P_n and P_L are the pressure inside the bubble and the ambient pressure, respectively. Taking the derivative of the energy with respect to r gives

$$
\frac{dE}{dr} = 8\pi r\sigma - 4\pi r^2\left(P_n - P_L\right)
\tag{2.5}
$$

Therefore for small r the derivative is positive, and so the bubble will tend to shrink, and for large r the derivative is negative and the bubble will tend to grow. For a given radius the pressure difference required to maintain the bubble size is

$$
P_n - P_L = \frac{2\sigma}{r}
\tag{2.6}
$$

Therefore the pressure required to maintain a bubble at a given radius is inversely proportional to the radius. From this simple analysis it appears that it requires an infinite pressure to create a bubble, and that homogeneous nucleation is therefore impossible. If the temperature is sufficiently high, however, the critical bubble size is sufficiently small that it can form from thermal fluctuations. We find that when the energy required to create a critical size bubble is approximately equal to kT, a bubble can form by thermal fluctuations of the liquid.

More specifically, substituting (2.6) into (2.4) gives the work of formation of a critical size nucleus as

$$W = 4\pi r^2 \sigma - \tfrac{4}{3}\pi r^3 \frac{2\sigma}{r}$$
$$= \tfrac{4}{3}\pi r^2 \sigma \qquad (2.7)$$

Now rearranging (2.6) gives

$$r = \frac{2\sigma}{P_n - P_L} \qquad (2.8)$$

So in terms of the pressure the work of formation is

$$W = \frac{16\pi\sigma^3}{3\left(P_n - P_L\right)^2} \qquad (2.9)$$

We should expect that the nucleation rate per unit volume of liquid is proportional to $e^{-W/kT}$, where W is as given in equation (2.9). Finding the exact expression for the nucleation rate per unit volume is a complex problem in statistical mechanics, and was first done by Volmer [16]. The expression derived by Volmer is

$$J = N_0 \left[\frac{6\sigma}{\pi m(3-b)} \right]^{\frac{1}{2}} e^{-\lambda/kT} e^{-W/kT} \qquad (2.10)$$

where N_0 is the number of molecules per cubic metre, m is the mass of each molecule, λ is the molecular heat of vaporisation, and b is defined by

$$b = \left(P_n - P_L\right) / P_n \qquad (2.11)$$

The pressure inside the bubble is given by

$$P_n = P_v \exp\left[\frac{P_L - P_v}{N_0 kT} \right] \qquad (2.12)$$

where P_v is the normal vapour pressure at temperature T. The pressure inside the bubble is less than the vapour pressure. This is because the liquid is at ambient pressure rather than saturation pressure [17, 18]. These expressions allow us to find theoretical values for the

nucleation rate, provided we know the surface tension, vapour pressure, molecular heat of vaporisation and number of molecules per cubic metre as a function of temperature.

2.6 Theoretical Nucleation Rates

The surface tension of water, σ_0, is tabulated at every 5 degrees from the triple point to the critical point in [19]. As an interpolating equation we can use

$$\sigma_0 = A\tau^u\left[1 + B\tau\right] \tag{2.13}$$

where
$$\tau = 1 - T/T_c$$
$$A = 235.8 \text{ mN·m}^{-1}$$
$$T_c = 647.126 \text{ K}$$
$$B = -0.625$$
$$u = 1.256$$

This gives values for the surface tension within the uncertainties of the measured values. A more recent equation is [20]

$$\sigma_0 = a\tau^{5/4} + b\tau^{9/4} + c\tau^{13/4} \tag{2.14}$$

where
$$a = 232.713514 \text{ mN·m}^{-1}$$
$$b = -140.186450 \text{ mN·m}^{-1}$$
$$c = -4.890098 \text{ mN·m}^{-1}$$

For water this equation is not quite as accurate as (2.13), however for other liquids it is more accurate than (2.13) (with appropriate values of a, b and c).

The above equations give the surface tension for a flat surface, however the surface tension changes with the curvature of the surface (see Tolman [21]). This is due to the fact that the surface where the surface tension acts is not exactly at the dividing surface between the liquid and the gas. The effect of curvature dependent surface tension on homogeneous nucleation has not been taken account of until recently (see Jayaraaman et. al. 1989 [22]). The surface tension of a bubble is approximately given by

$$\sigma = \sigma_0 \frac{1}{1 - 2\delta/r} \tag{2.15}$$

where σ_0 is the surface tension for a flat surface and δ is a constant. There is no general agreement on the exact value to use for δ, however 2δ is usually taken to be approximately equal to the intermolecular distance. This is equivalent to assuming that the average position

where the surface tension acts is half an intermolecular distance away from the dividing surface. Therefore the value of δ will be estimated here by

$$\delta = \frac{1}{2}\sqrt[3]{\frac{m}{\rho}} \tag{2.16}$$

where ρ is the density of the liquid. Now if we substitute equation (2.6) into equation (2.15) then we get

$$\sigma = \sigma_0 + \delta(P_n - P_L) \tag{2.17}$$

Substituting (2.17) into (2.9) then gives

$$W = \frac{16\pi}{3(P_n - P_L)}(\sigma_0 + \delta(P_n - P_L))^3 \tag{2.18}$$

The vapour pressure of water is tabulated at every degree from 0°C to 373°C in [23]. An interpolating equation is given in [24]

$$P = P_c \exp\left(\frac{T_c}{T}\left(a_1\tau + a_2\tau^{1.5} + a_3\tau^3 + a_4\tau^{3.5} + a_5\tau^4 + a_6\tau^{7.5}\right)\right) \tag{2.19}$$

where
$$P_c = 22.064\text{x}10^6 \text{ Pa}$$
$$a_1 = -7.85823$$
$$a_2 = 1.83991$$
$$a_3 = -11.7811$$
$$a_4 = 22.6705$$
$$a_5 = -15.9393$$
$$a_6 = 1.77516$$

The heat of vaporisation of water is given by the interpolating formula [25]

$$\lambda = a\tau^m + b\tau^{1+m} + c\tau^{2+m} + d\tau^{3+m} \tag{2.20}$$

where
$$m = 3/8$$
$$a = 44.457979 \text{ kJ·mol}^{-1}$$
$$b = 14.635863 \text{ kJ·mol}^{-1}$$
$$c = -27.945633 \text{ kJ·mol}^{-1}$$
$$d = 13.985176 \text{ kJ·mol}^{-1}$$

Also the density of water at atmospheric pressure is given by [26]

$$\rho = \frac{a_0 + a_1 t + a_2 t^2 + a_3 t^3 + a_4 t^4 + a_5 t^5}{1 + bt} \tag{2.21}$$

where
$$t = T - 273.15 \text{ K}$$

$$b = 1.6879850 \text{x} 10^{-2} \text{ K}^{-1}$$
$$a_0 = 999.83952 \text{ kg·m}^{-3}$$
$$a_1 = 16.945176 \text{ kg·m}^{-3}\text{K}^{-1}$$
$$a_2 = -7.9870401 \text{x} 10^{-3} \text{ kg·m}^3\text{K}^{-2}$$
$$a_3 = -4.6170461 \text{x} 10^{-5} \text{ kg·m}^3\text{K}^{-3}$$
$$a_4 = 1.0556302 \text{x} 10^{-7} \text{ kg·m}^3\text{K}^{-4}$$
$$a_5 = 2.8054253 \text{x} 10^{-10} \text{ kg·m}^3\text{K}^{-5}$$

It is important to use the formula for the density of water, rather than assuming that the density is a constant, as the density decreases significantly at very high temperatures, and the formula is moderately sensitive to the density. Equation (2.21) was fitted to the data for the density of water only up to 150°C. The density at higher temperatures can alternatively be obtained by interpolation from the values given in [27], however this has a negligible effect on the results.

The values of the various other constants required to calculate the nucleation rate are
$$k = 1.380658 \text{x} 10^{-23} \text{ J·K}^{-1}$$
$$m = 2.99151962867 \text{x} 10^{-26} \text{ kg}$$
$$P_L = 101325 \text{ Pa}$$

Now using equations (2.10), (2.11), (2.12), (2.13), (2.16), (2.18), (2.19), (2.20) and (2.21) with the above values for the various constants we can calculate the nucleation rate. The nucleation rate calculated from these formulae is plotted as a function of temperature in figure 2.6. The nucleation rate where the change in surface tension with curvature is ignored is also plotted for comparison.

Nucleation can theoretically occur at any temperature (between the boiling point and the critical point), however the nucleation rate varies extremely rapidly with temperature, and in practice nucleation will only occur over a small range of temperatures. In the case of heating by the laser tweezers apparatus, the volume of water being heated is on the order of a cubic micrometre, and the observation time is on the order of seconds, so as a rough order of magnitude estimate, the nucleation rate required for bubble formation to be observed is about $10^{18} \text{ m}^{-3}\text{s}^{-1}$. If we restrict the plot to values near this order of magnitude then we have the plot as in figure 2.7.
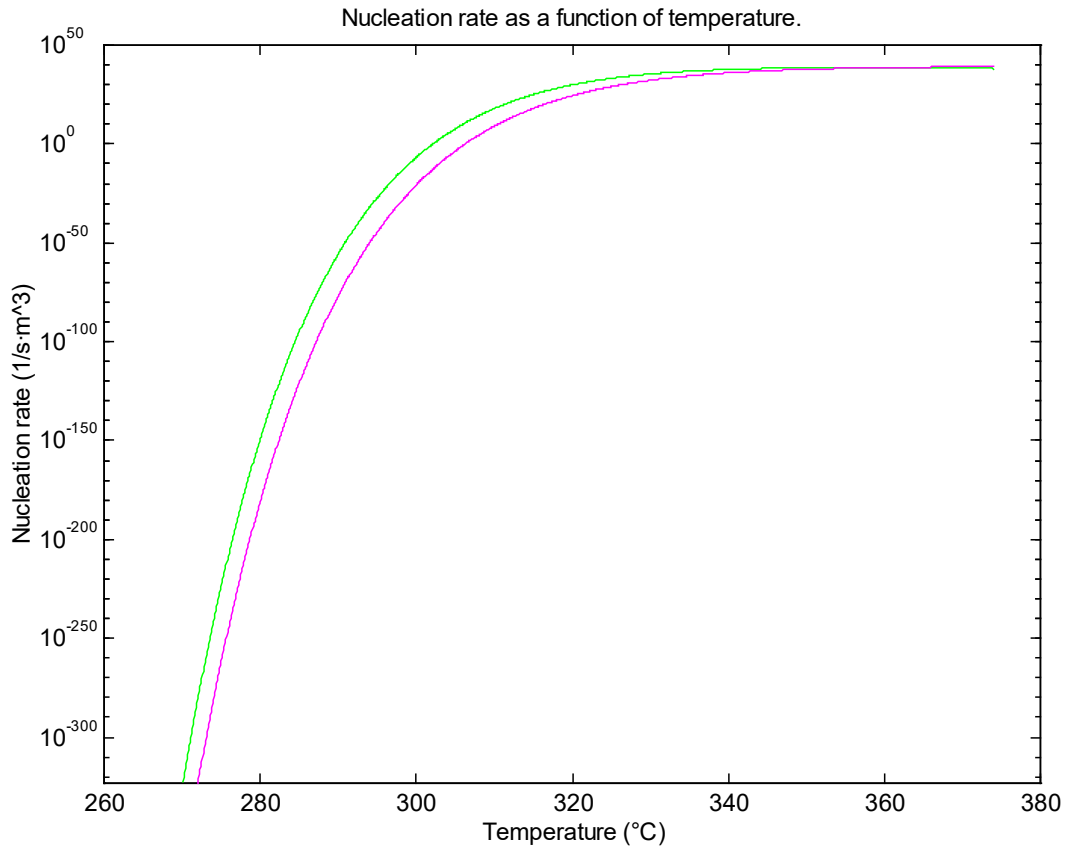
Figure 2.6: The theoretical nucleation rates as a function of temperature. The nucleation rate ignoring the change in surface tension with radius is shown in green, and the nucleation rate taking account of this is shown in red.

From figure 2.7, for volumes on the order of a cubic micrometre the temperature must be increased to about 315°C before homogeneous nucleation can occur. This temperature is remarkably high, over 200°C above the boiling point of water. It is therefore unsurprising that it is possible to heat toner particles above the boiling point of water without the production of bubbles.

If the change in surface tension with curvature is ignored, then the theoretical homogeneous nucleation temperatures are about 5°C less. Firstly, note that although this difference in temperature is significant, it is not sufficiently great to affect the observations. Secondly, it must be emphasised that the value of δ was only roughly estimated, and may be incorrect by as much as a factor of two. Therefore, the predicted nucleation temperatures have an uncertainty of a few degrees due to the uncertainty in the value of δ.

A slight complication is the presence of dissolved gases in the liquid. This is taken into account by subtracting the partial pressure of dissolved gas from the ambient liquid pressure in the formula for the nucleation rate. In these experiments the partial pressure of dissolved
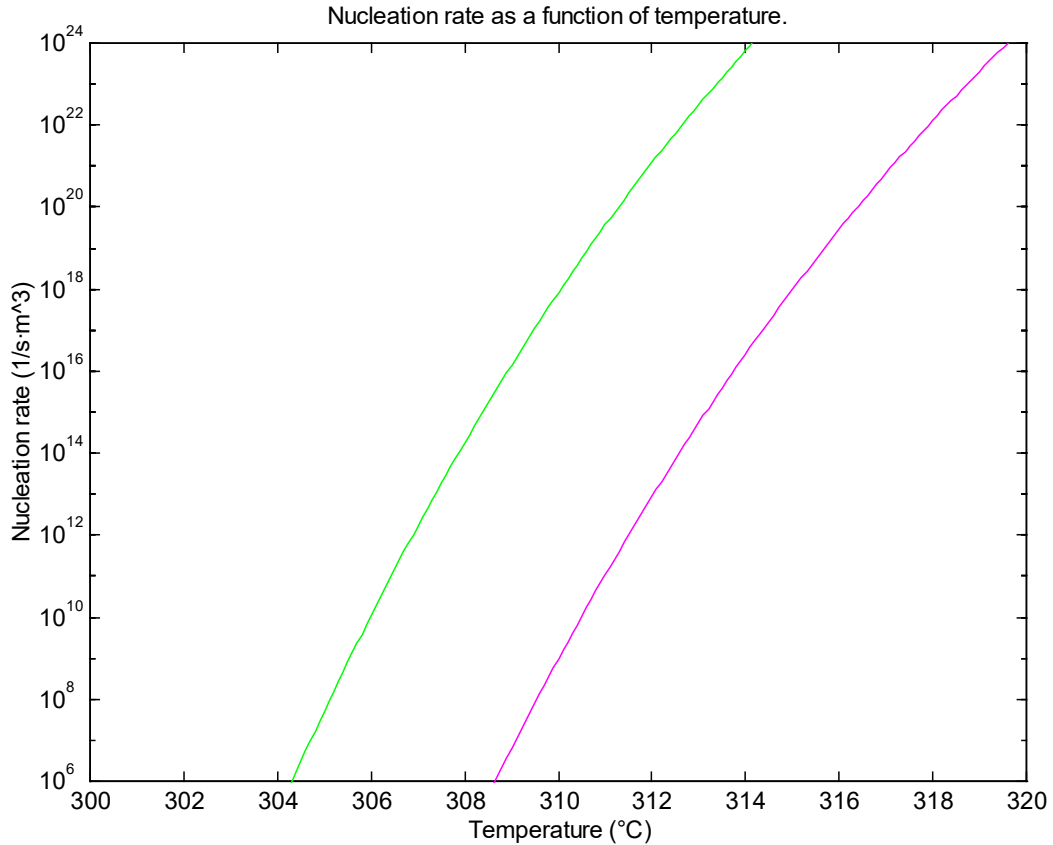
Figure 2.7: Plot of theoretical nucleation rates with restricted range. The nucleation rate ignoring the change in surface tension with radius is shown in green, and the nucleation rate taking account of this is shown in red.

gas in the liquid is unknown, but if we assume that it is the same as the ambient liquid pressure then the corrected nucleation rates are as in figure 2.8. From this graph we can see that even assuming a partial pressure of dissolved gas equal to the ambient liquid pressure only reduces the nucleation temperature by about 0.2°C, which is far less than other uncertainties. It is therefore reasonable to ignore dissolved gases when considering the nucleation.

The highest measured superheat for water was about 302.1°C in the experiments of Skripov and Pavlov in 1970 [28], which is well below the range of temperatures predicted by the homogeneous nucleation formula. The experimental technique which was used for these measurements was pulse heating, where a very short current pulse is sent through a very thin wire immersed in the liquid. Other common techniques for measuring the limits of superheat of liquids are heating the liquid in very fine capillary tubes and heating a droplet of the liquid in a surrounding liquid with a much higher boiling point. The method involving heating of a droplet of the liquid has the advantage that it removes the problem of nucleation at the solid-
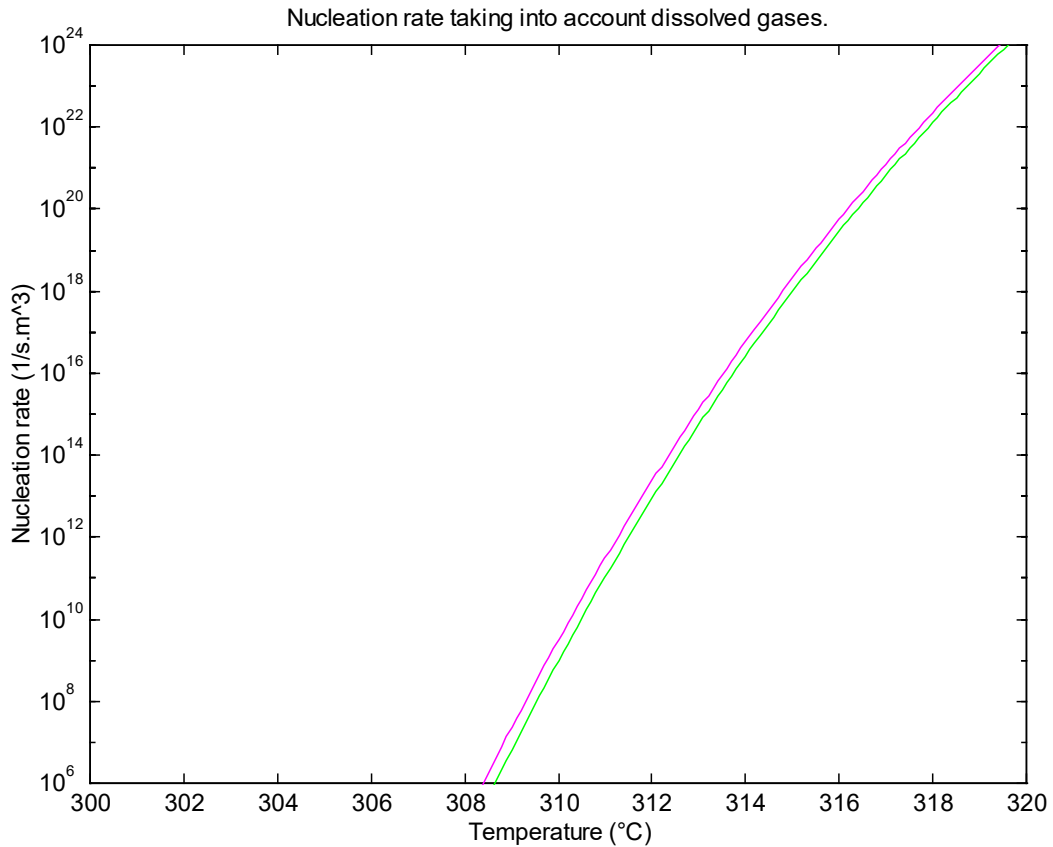
Figure 2.8: The nucleation rates per unit volume correcting for and ignoring dissolved gases. The nucleation rate assuming no dissolved gases is shown in green and the nucleation rate assuming a partial pressure of dissolved gases equal to the ambient liquid pressure is shown in red.

liquid interface, but it has the disadvantage that larger volumes are involved, so the temperature cannot be increased as high. For a more thorough description of the experimental methods involved, see Avedisan [29].

2.7 Temperature Distribution

It is important to calculate the temperature distribution in and around the particle for two reasons. Firstly, due to the low thermal conductivity of the toner, the temperature in the interior of a heated toner particle varies greatly, so some parts of the toner can be above the melting point while other parts are well below. This means that the temperature distribution must be calculated for any comparison between the theoretical temperature at melting and the melting point of the toner. Even then it is not possible to make precise predictions, as it is not known what proportion of the particle should be above the melting point before the melting

becomes visible. For quantitative calculations it will be assumed that the particle is visibly melted when the maximum surface temperature is at the melting point.

Secondly, in order to more accurately determine the temperature at which we can expect homogeneous nucleation to occur, it is necessary to determine the temperature distribution. The nucleation rate is then given by the integral

$$\frac{dN}{dt} = \int J(T)dV \tag{2.22}$$

where J(T) is the nucleation rate per unit volume as given by equation (2.10).

The temperature distribution in the case of a point heat source at the interface between the water and the glass has the analytic solution (ignoring the variation in thermal conductivity with temperature)

$$T(r) = \frac{P}{2\pi r (h_w + h_s)} + T_0 \tag{2.23}$$

where P is the power of the heat source, r is the distance from the heat source, and h_w and h_s are the thermal conductivities of the water and the slide, respectively, and T_0 is the ambient temperature. This solution is not intuitively obvious, as it might be expected that the temperature distribution in the slide is different to that in the water. It obviously satisfies the differential equations and boundary conditions for the temperature (see (2.25) and (2.31g)), however.

In the case of a particle heated by a laser beam, the temperature distribution will approach this at a large distance from the particle, however this is a very poor estimate of the temperature close to the particle. The temperature close to the particle can be estimated more accurately by assuming some shape of the particle and heating pattern, and solving for the temperature distribution numerically.

The shapes of unmelted toner particles tend to be very irregular, however calculations were performed only for the case that the toner particle has the shape of a hemispherical blob resting on the slide. Once a particle has been melted it will tend to assume this shape, and in addition assuming this shape simplifies the calculations greatly. The toner particles are partially transparent, so they absorb the laser power throughout their bulk rather than at the surface. The beams used had either Gaussian or Gauss-Laguerre profiles, and the laser intensity should fall off exponentially with depth into the particle. Since the heating is proportional to the intensity, this is also the heating pattern. The opacity is not known, but it can be roughly estimated from the proportion of the laser light transmitted through and around

the particle, and the geometric configuration. For a given opacity the fraction of power transmitted can be determined by a numerical integration of the intensity at the position of the slide surface. The opacity can then be estimated given the fraction of power transmitted by inverse function solving techniques.

The change in the beam width with propagation was ignored for most calculations. For typical experimental conditions of a beam width of approximately 1 μm and a particle radius of about 2 μm, the change in the beam width in water over a distance equal to the thickness of the particle is only about 4%. In simulations where the change in beam width was assumed to be the same as in water, the maximum temperature obtained was changed by less than 2%, which is negligible as compared to other uncertainties. Determining the exact beam shape in the presence of the particle is a difficult problem, which can only be solved numerically. In addition, the position of the beam waist and the refractive index of the toner particle are unknown, making it impossible to determine the exact intensity distribution anyway. For these reasons the spread of the beam with propagation will be ignored in the following discussion.

In order to solve for the temperature distribution, it is also necessary to know the thermal conductivities of the substances. The toner particles are composed mostly of styrene acrylate copolymer, plus some carbon black pigment [30]. The thermal conductivity of styrene acrylate copolymer is not tabulated, however the thermal conductivities of styrene and acrylic vary from 0.12 $W \cdot K^{-1} m^{-1}$ to 0.25 $W \cdot K^{-1} m^{-1}$ [31]. It will be assumed for the purpose of the simulation that the thermal conductivity is 0.19 $W \cdot K^{-1} m^{-1}$. The microscope slides and coverslips are composed of soda glass. The thermal conductivity of soda glass varies by about 10% with composition and temperature, but is on average about 1 $W \cdot K^{-1} m^{-1}$ [23]. The thermal conductivity of water varies from 0.6071 $W \cdot K^{-1} m^{-1}$ at 25°C (room temperature) to 0.6791 $W \cdot K^{-1} m^{-1}$ at 100°C [23]. The thermal conductivity of water will be assumed to be approximately constant at about 0.68 $W \cdot K^{-1} m^{-1}$, since taking account of the variation in the thermal conductivity with temperature creates a nonlinear problem.

The appropriate differential equation for the temperature is

$$h \nabla^2 T = -q \tag{2.24}$$

where h is the thermal conductivity and q is the heat absorbed per unit volume. In the water and in the slide no energy is absorbed, so this reduces to

$$\nabla^2 T = 0 \tag{2.25}$$

Let us use spherical polar coordinates such that $\theta = 0$ is perpendicular to the slide surface. For a vertical Gaussian beam the intensity is

$$I = \frac{2}{\pi}\frac{P}{\omega^2}\exp\left[-2r^2\sin^2\theta/\omega^2\right] \qquad (2.26)$$

where P is the power and ω is the beam width. For a vertical Gauss-Laguerre beam of order n the intensity is

$$I = \frac{2}{\pi}\frac{2^n}{n!}\frac{P}{\omega^2}\left(\frac{r}{\omega}\right)^{2n}\exp\left[-2r^2\sin^2\theta/\omega^2\right] \qquad (2.27)$$

Note that if we put $n = 0$ in equation (2.27) then we get equation (2.26). Therefore equation (2.27) will be used, and the Gaussian case will be considered as the case $n = 0$.

Now if the radius of the particle is r_p, then the vertical thickness of particle above a point at position (r, θ) (see figure 2.9) is

$$\Delta z = \sqrt{r_p^2 - r^2\sin^2\theta} - r\cos\theta \qquad (2.28)$$
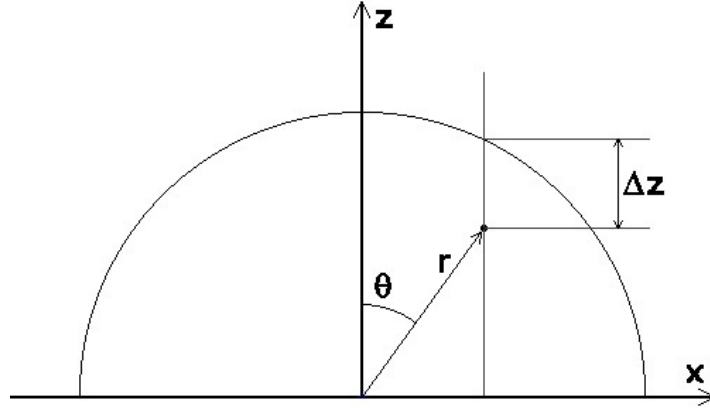
Figure 2.9: Geometric configuration for calculation of thickness of particle above a point.

If the opacity of the particle is κ, then the intensity of the beam taking into account the absorption of light by the particle is

$$I = \frac{2}{\pi}\frac{2^n}{n!}\frac{P}{\omega^2}\left(\frac{r}{\omega}\right)^{2n}\exp\left[-2r^2\sin^2\theta/\omega^2 - \kappa\left(\sqrt{r_p^2 - r^2\sin^2\theta} - r\cos\theta\right)\right] \qquad (2.29)$$

The energy absorbed per unit volume is κI, so the differential equation inside the particle is therefore

$$\nabla^2 T = -\frac{2\kappa P}{\pi h_p\omega^2}\frac{2^n}{n!}\left(\frac{r}{\omega}\right)^{2n}\exp\left[-2r^2\sin^2\theta/\omega^2 - \kappa\left(\sqrt{r_p^2 - r^2\sin^2\theta} - r\cos\theta\right)\right] \qquad (2.30)$$

The boundary conditions that must be satisfied are

$$\left[\frac{\partial T_p}{\partial r}\right]_{r=0} = 0 \tag{2.31a}$$

$$\left[\frac{\partial T_p}{\partial \theta}\right]_{0<r\leq r_p,\theta=0} = 0 \tag{2.31b}$$

$$\left[\frac{\partial T_s}{\partial \theta}\right]_{0<r<\infty,\theta=\pi} = 0 \tag{2.31c}$$

$$\left[\frac{\partial T_w}{\partial \theta}\right]_{r_p<r<\infty,\theta=0} = 0 \tag{2.31d}$$

$$\left[h_p\frac{\partial T_p}{\partial \theta} - h_s\frac{\partial T_s}{\partial \theta}\right]_{0<r<r_p,\theta=\pi/2} = 0 \tag{2.31e}$$

$$\left[h_p\frac{\partial T_p}{\partial r} - h_w\frac{\partial T_w}{\partial r}\right]_{r=r_p,0<\theta\leq\pi/2} = 0 \tag{2.31f}$$

$$\left[h_w\frac{\partial T_w}{\partial \theta} - h_s\frac{\partial T_s}{\partial \theta}\right]_{r_p<r<\infty,\theta=\pi/2} = 0 \tag{2.31g}$$

$$\left[T_w\right]_{r=\infty,0\leq\theta\leq\pi/2} = T_0 \tag{2.31h}$$

$$\left[T_s\right]_{r=\infty,\pi/2<\theta\leq\pi} = T_0 \tag{2.31i}$$

where the subscripts p, w and s refer to the particle, the water and the slide respectively. Equations (2.31a) to (2.31d) are due to bilateral symmetry, equations (2.31e) to (2.31g) are due to continuity of heat flow over the boundaries, and (2.31h) and (2.31i) are based on a uniform temperature distribution at infinity.

In the discretisation, calculations were restricted to the region $0\leq r\leq L$, $0\leq\theta\leq\pi$, with the infinity conditions being applied at $r = L$. Note that the system has rotational symmetry, so the ϕ coordinate can be ignored. An equally spaced mesh was used where

$$r_i = i\Delta r \qquad i = 1,2,...,I \qquad \theta_j = j\Delta\theta \qquad j = 0,1,..., J \tag{2.32}$$

where

$$\Delta r = \frac{L}{I} \qquad \Delta\theta = \frac{\pi}{J} \tag{2.33}$$

The centre of the particle is represented by a single point. In spherical polar coordinates, and ignoring ϕ, $\nabla^2 T$ is

$$\nabla^2 T = \frac{1}{r^2}\frac{\partial}{\partial r}\left(r^2\frac{\partial T}{\partial r}\right) + \frac{1}{r^2\sin\theta}\frac{\partial}{\partial \theta}\left(\sin\theta\frac{\partial T}{\partial \theta}\right) \tag{2.34}$$

23

This is discretised to

$$\nabla^2 T = \frac{r_{i+\frac{1}{2}}^2\left(T_{i+1,j} - T_{i,j}\right) + r_{i-\frac{1}{2}}^2\left(T_{i,j} - T_{i-1,j}\right)}{(\Delta r)^2} + \frac{\sin\theta_{j+\frac{1}{2}}\left(T_{i,j+1} - T_{i,j}\right) + \sin\theta_{j-\frac{1}{2}}\left(T_{i,j} - T_{i,j-1}\right)}{(\Delta\theta)^2 \sin\theta_j} \quad (2.35)$$

For differential boundary conditions we can approximate the derivative by expressions of the form

$$\left.\frac{dy}{dx}\right|_{x=0} \approx \frac{y_1 - y_0}{\Delta x} \quad (2.36)$$

where

$$y_n \equiv y(n\Delta x) \quad (2.37)$$

This approximation is very inaccurate, however, as the error scales as Δx. A more accurate approximation can be made using the first three points. If we fit a quadratic of the form $y = ax^2 + bx + c$ to the first three data points we find that

$$\begin{aligned} y_0 &= c \\ y_1 &= a(\Delta x)^2 + b(\Delta x) + c \\ y_2 &= a(2\Delta x)^2 + b(2\Delta x) + c \end{aligned} \quad (2.38)$$

Solving these equations for a, b, and c, we find that

$$\begin{aligned} a &= \frac{y_0 - 2y_1 + y_2}{2(\Delta x)^2} \\ b &= \frac{-3y_0 + 4y_1 - y_2}{2\Delta x} \\ c &= y_0 \end{aligned} \quad (2.39)$$

The derivative of the fitted polynomial at $x = 0$ is then b. Therefore we can make the approximation

$$\left.\frac{dy}{dx}\right|_{x=0} \approx \frac{-3y_0 + 4y_1 - y_2}{2\Delta x} \quad (2.40)$$

An expression of this form was used to approximate the derivatives for each of the differential boundary conditions. Each of the discretised equations was represented by a line of a sparse matrix in Matlab [32], and solved using the inbuilt matrix routines of Matlab. There must be as many equations as unknowns in order to solve the system, so there must be one equation corresponding to each point where the temperature distribution is represented. This does not present a problem except at corners and at the central point, where the boundary conditions overlap.

The boundary conditions which are used at each of the corners are indicated by the ranges on the boundary conditions in (2.31). At the centre the three adjacent boundary conditions are

(2.31b), (2.31c) and (2.31e). None of these can be used, however, as they involve derivatives with respect to θ. The boundary condition used at the centre was that due to bilateral symmetry, and is given as (2.31a).

There is a further correction which was made in the program. It is more accurate to assume that the temperature distribution is approximately equal to the limiting temperature distribution given by equation (2.23) at the boundary at $r = L$, rather than assuming that the temperature is T_0. This can be accounted for by adding the temperature

$$\Delta T = \frac{P'}{2\pi L\left(h_w + h_s\right)} \tag{2.41}$$

where P' is the total power absorbed (rather than the power at the focus), to the temperature distribution after the uncorrected solution has been found. The complete program for a Gauss-Laguerre beam of order n is listed in appendix B.1. The case of a Gaussian beam is obtained by taking $n = 0$ in this program. This program gives the temperature relative to the ambient temperature, which must be added separately.

2.8 Comparison with Experiment

It is possible to use the program described above to determine the theoretical temperature distribution for configurations observed experimentally. For the example of the particle shown in figure 2.2, the beam power was $P = 1.24$ mW and the particle radius was approximately $r_p = 1.90$ µm. The observed beam width was approximately 1 µm, and the fraction of the beam power that passed through the particle was approximately 27%. The value of κ required for this proportion of the beam to pass through the particle is approximately 7.5×10^5 m^{-1}. Also the ambient temperature in the laboratory was about 22°C. It was found that at the position of the slide the temperature was slightly higher due to the heating from the condenser light, and was approximately 25°C. The theoretical temperature distribution with these values of the various parameters is shown in figure 2.10. The grid parameters for this simulation are $L = 5r_p$, $I = 65$ and $J = 32$.

In the simulation shown in figure 2.10, note that the temperatures are roughly in the right range, with temperatures in the toner above the softening point of the toner of around 80°C, and temperatures in the water well below the homogeneous nucleation temperature of around 310°C. Note, however, that the temperatures in the toner are well above the softening point

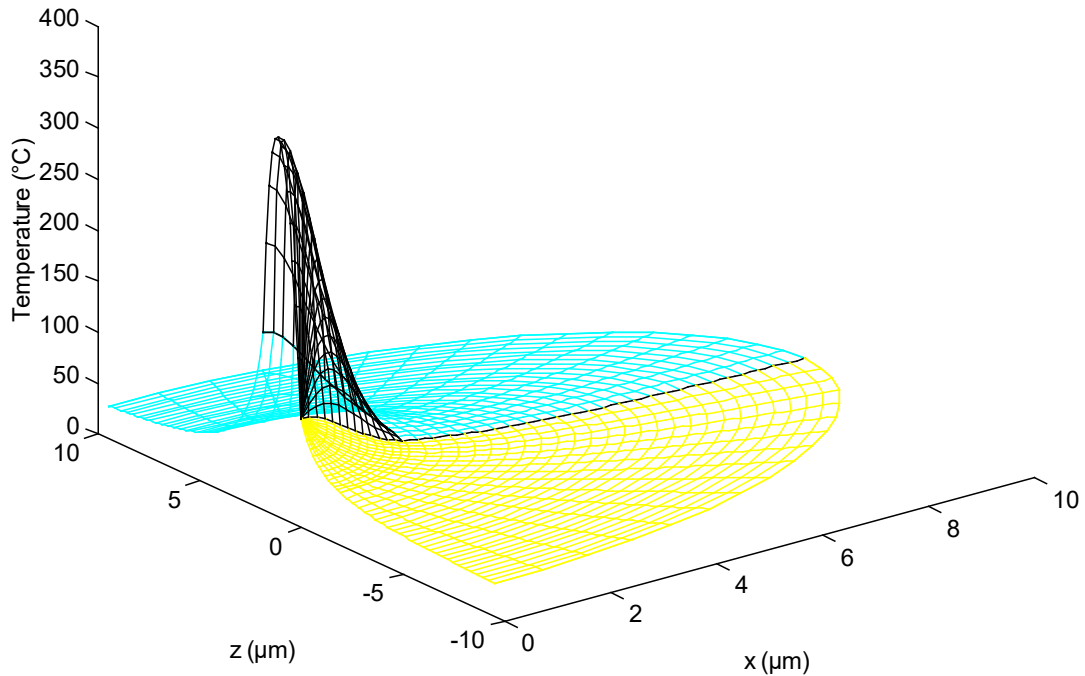Temperature distribution around heated toner particle.

Figure 2.10: Theoretical temperature distribution around hemispherical toner particle heated by a Gaussian beam. The beam power is 1.24 mW, the beam width is 1 μm, the toner particle radius is 1.90 μm, and the opacity is 0.75 μm^{-1}. The temperature distributions in the particle, the water and the slide are shown in black, blue and yellow, respectively.

for the toner. Since the simulation was performed for the power just sufficient to cause some visible softening of the particle, there should only be a fairly small region above 80°C. Instead most of the particle is above 80°C, and the interior temperature reaches a maximum of about 374°C.

Judging from the simulation a power about three times less should be sufficient to cause visible softening of the toner. It must be emphasised that there are many uncertainties in the simulation. The most important are that the thermal conductivity of the toner is only approximately known and the shape of the particle is only roughly hemispherical. Also the shape of the beam is only approximately Gaussian, and the beam width was only roughly estimated. Of these factors the most significant is the uncertainty in the thermal conductivity of the toner.

The predicted temperatures inside the particle are very sensitive to the assumed thermal conductivity, but the surface temperature is not very sensitive. As the assumed thermal

conductivity is changed from about 0.12 W·K^{-1}m^{-1} to 0.25 W·K^{-1}m^{-1}, the maximum predicted temperature inside the particle varies from 525°C to 311°C, while the predicted surface temperature varies by less than 10°C. Therefore even this variation is not great enough to account for the higher than expected temperatures.

There are two further factors that may be significant, other particles above the focal point absorbing a significant portion of the beam, and the reflectance of the toner particles. In order to test the first possibility, samples with far more sparse suspensions of toner particles were tested, and it was found that this had no detectable effect on the power required for melting. Also it was found that the ratio of the power passing through the lower objective of the microscope when the beam was not directed at a particle was entirely consistent with the calibration measurements. The remaining possibility is that a significant fraction of the power was reflected from the toner particles. It can be seen visually that a significant proportion of the beam is reflected, however there is no simple, quantitative way of testing if the reflected light can account for the difference between the theoretical and experimental temperatures.

Now consider the case that the beam is a third order Gauss-Laguerre beam, but all the other parameters are the same. For a Gauss-Laguerre beam the beam width is

$$\omega = \sqrt{\frac{2}{n}}r \qquad (2.42)$$

where r is the radius of the doughnut (i.e. the ring of maximum intensity). Therefore if the radius of the doughnut is about 0.5 μm, then the beam width is $\omega = 0.41$ μm. Using this value for ω, and the same values for the other parameters as before, the theoretical temperature distribution is as shown in figure 2.11.

From these simulations, we can see that there is very little difference between the result for a Gaussian beam and the result for a Gauss-Laguerre beam. The maximum temperature on the surface differs only by about 3°C between the simulations, and the maximum interior temperature only differs by about 16°C. The main difference is that the region of maximum temperature is now a ring rather than a point.

It was noticed that if the size of the particle was increased in the simulation, but all of the other parameters were kept the same, the temperatures of the toner remained fairly constant. For example, if the radius of the toner particle is doubled, the maximum internal temperature and the maximum surface temperature increase by less than 30°C. Doubling the radius again alters the temperatures by less than 10°C. This is in agreement with the experimental observations that above a certain power it was possible to partially melt particles of a wide
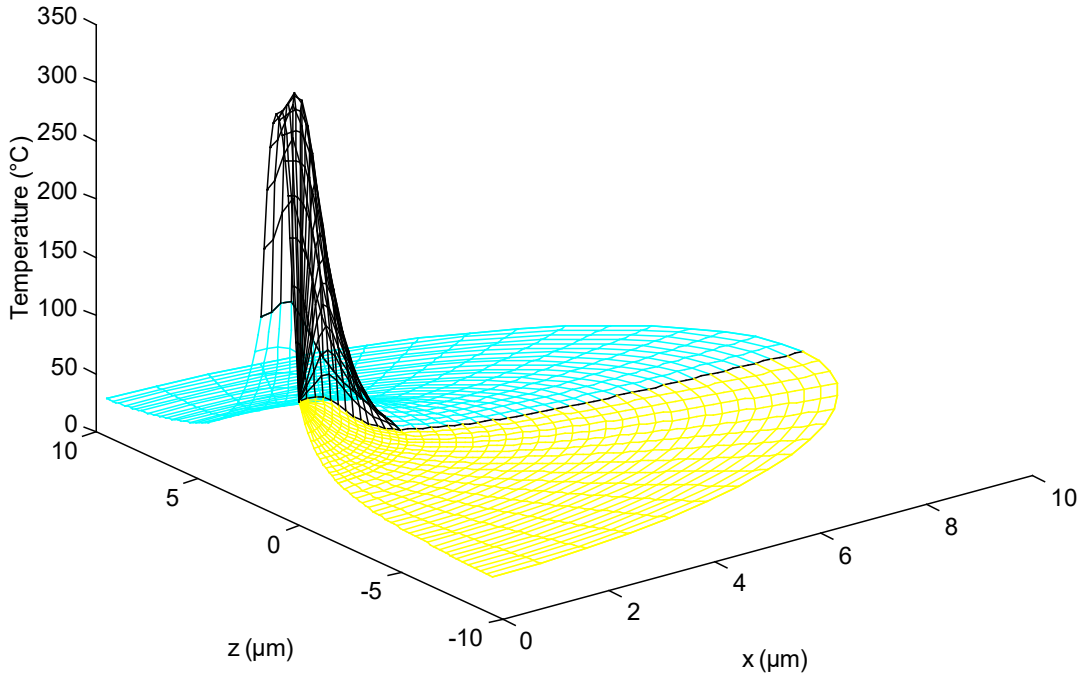
Figure 2.11: Temperature distribution around hemispherical toner particle heated by a third order Gauss-Laguerre beam. The beam power is 1.24 mW, the beam width is 0.41 μm, the toner particle radius is 1 μm, and the opacity is 0.75 μm^{-1}. The temperature distributions in the particle, the water and the slide are shown in black, blue and yellow, respectively.

range of sizes.

2.9 Integration for Nucleation Rate

The temperature distributions calculated using the program described in section 2.6 can be used to determine the total nucleation rate by a numerical integration. Simulations were performed for the Gaussian and third order Gauss-Laguerre modes with $P = 1$ mW, $\kappa = 7.5 \times 10^5$ m^{-1}, $r_p = 2$ μm, and $\omega = 1$ μm in the Gaussian case and $\omega = 0.5$ μm in the Gauss-Laguerre case. These values of the parameters were chosen because these were the typical values in experimental observations. The value of P is unimportant, as the temperature distribution for different powers can be obtained by linearly scaling the results. The grid parameters used were $L = 5r_p$, $I = 255$ and $J = 128$.

When the temperature distribution was scaled so that the maximum temperature at the

surface of the particle was about 315°C (the approximate temperature where the nucleation rate becomes significant), it was found that the nucleation rate per unit volume dropped off by a factor of around 10^{15} between the grid line at the surface of the particle and the next grid line, however the nucleation rate per unit volume dropped off reasonably slowly in the angular direction. In order to perform the integration the region between the grid line at the surface of the particle and the next grid line was divided into 100 segments, with a width of approximately 0.2 nm, and the temperatures at the intermediate segments were interpolated. Similarly the grid was refined in the θ direction by dividing each interval into two segments. The temperatures at the points in this refined grid were then used for the integration for the total nucleation rate. The complete program is listed in appendix B.2.

The calculated nucleation rates for the Gaussian and third order Gauss-Laguerre beams are plotted as functions of the peak water temperature in figure 2.12. From this graph, it can be seen that, in the Gaussian case, bubbles will form when the peak temperature in the water is approximately 319°C. Note that this is about 17°C higher than the highest experimentally measured superheat. This is equivalent to a peak nucleation rate per unit volume of approximately 3×10^{23} m^{-3}s^{-1}, which is 300000 times the order of magnitude estimate given in section 2.5. This far higher peak nucleation rate is due to the very thin region where the nucleation occurs. The nucleation rate falls off by about 50% for a temperature decrease of about 0.26°C, and the temperature drops by about this amount in a radial distance of only 0.54 nm.

For the case of a Gauss-Laguerre beam, bubbles form when the peak temperature in the water is approximately 318°C, equivalent to a peak nucleation rate per unit volume of approximately 7×10^{21} m^{-3}s^{-1}. This is far lower than in the case of a Gaussian beam, and is about 7000 times the order of magnitude estimate given in section 2.5. The reason why the peak nucleation rate does not reach such high levels as in the Gaussian case is that there is a ring of maximum temperature rather than a point. This means that the region that is hot enough for there to be a significant nucleation rate is much larger than the region in the Gaussian case.
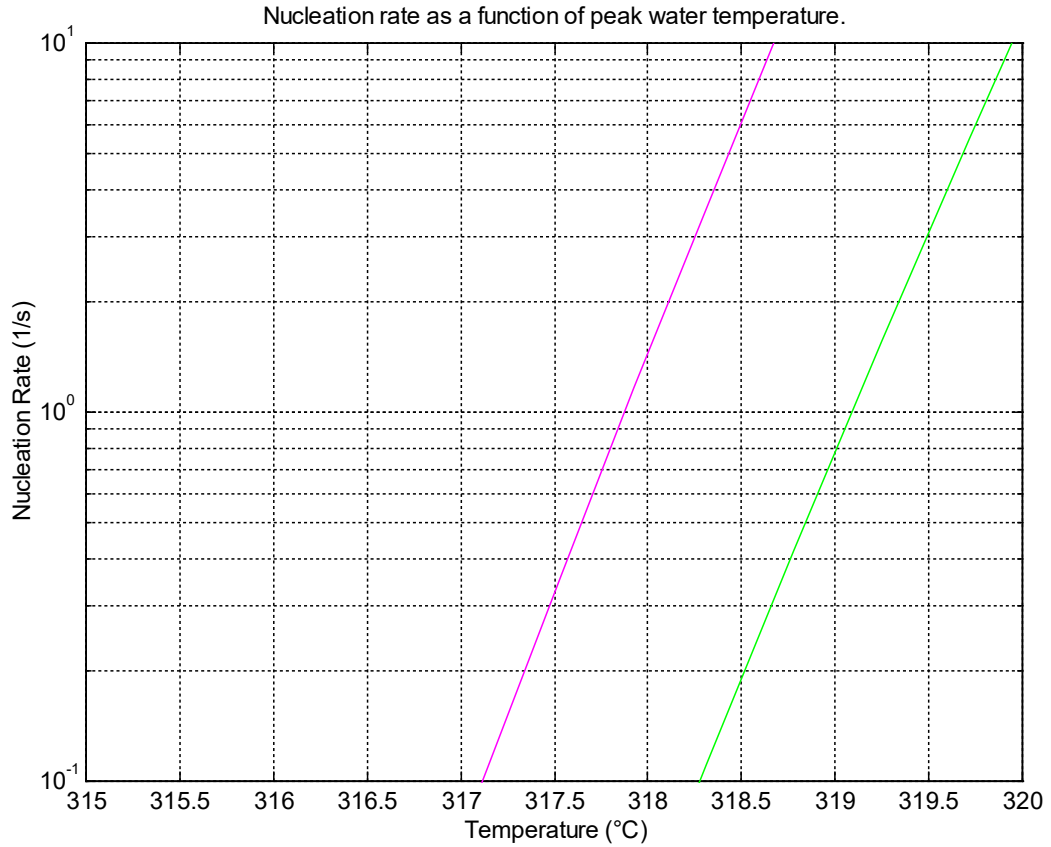
Figure 2.12: Total nucleation rate as a function of peak water temperature for 2 μm radius particle heated by a Gaussian beam (green) and by a third order Gauss-Laguerre beam (red).

The above calculations were repeated for various values of κ, r_p and ω, and it was found that the predicted nucleation temperatures were not sensitive to the exact values of these parameters, with the predicted temperatures varying by less than a degree. This means that the nucleation rates shown in figure 2.12 can be applied to moderately different geometric configurations without any significant loss of accuracy.

The predicted maximum liquid temperature at nucleation can be used to obtain an estimate of the power required for nucleation. In the case of the particle shown in figure 2.3, the predicted power to produce a bubble by homogeneous nucleation is 2.42 mW. This is only about 11% away from the experimentally measured power. Judging from the power required for melting, however, this agreement appears to be accidental, and due to a combination of reflection off the particle and nucleation occurring at a lower temperature than expected.

2.10 Heterogeneous Nucleation

2.10.1 Nucleation at a solid-liquid interface

The other main contribution to nucleation is from heterogeneous nucleation, where the nucleation occurs on the interface. Firstly it will be assumed that the particle is unmelted, so we have a solid-liquid interface. The energy of formation of a critical size bubble can be determined in a similar way as in the case of homogeneous nucleation, and is the same as equation (2.10) except it is multiplied by the factor [33]

$$\omega = \tfrac{1}{4}\left(1+\cos\phi\right)^2\left(2-\cos\phi\right) \tag{2.43}$$

Here ϕ is the angle between the surface of the solid and the surface of the bubble as measured through the liquid (see figure 2.13). This is called the contact angle or wetting angle, and only depends on the wetting of the surface, and not on the size of the bubble. The contact angle lies between 0° and 180°, though in practice ϕ is not usually above 90°. A contact angle of 0° corresponds to complete wetting of the surface, and a contact angle of 180° corresponds to a completely non-wetting surface.
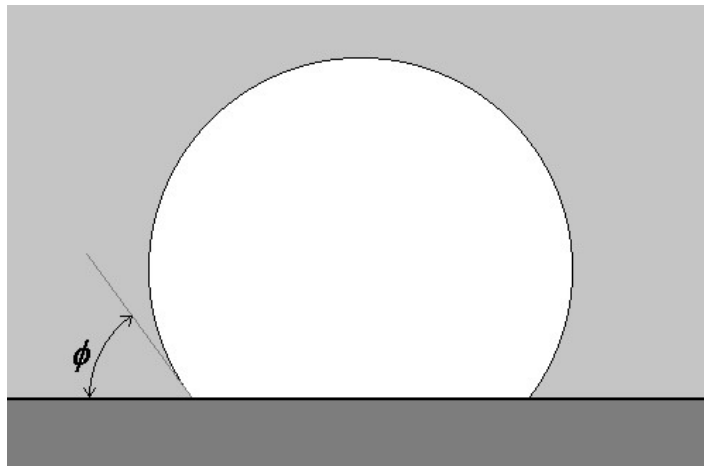
Figure 2.13: Diagram showing wetting angle for a bubble.

Also the number density of nucleation sites is taken as $N_0^{2/3}$ rather than N_0, as nucleation is on the surface rather than in the bulk. The complete formula for the heterogeneous nucleation rate per unit area is

$$J_{het} = N_0^{2/3}\psi\left[\frac{6\sigma}{\pi m\left(3-b\right)\omega}\right]^{\frac{1}{2}} e^{-\lambda/kT}\exp\left[-\frac{16\pi\sigma^3\omega}{3kT\left(P_n-P_L\right)}\right] \tag{2.44}$$

where

$$\psi = \tfrac{1}{2}\left(1 + \cos\phi\right)$$
$$\omega = \tfrac{1}{4}\left(1 + \cos\phi\right)^2\left(2 - \cos\phi\right)$$

(2.45)

and the other quantities are as defined for equation (2.10).

If $\phi = 0°$ (the liquid completely wets the surface) then we have

$$J_{het} = J_{homo} N_0^{-1/3}$$

(2.46)

The total nucleation rate per unit area is then given by

$$J_{tot} = J_{homo}\Delta x + J_{het}$$
$$= J_{homo}\left(\Delta x + N_0^{-1/3}\right)$$

(2.47)

where Δx is the approximate thickness of water at the nucleation temperature on the surface. Since $N_0^{-1/3}$ is approximately equal to the intermolecular distance, this implies that nucleation on the surface is no more likely than nucleation in the bulk. Usually this would mean that the contribution due to heterogeneous nucleation was negligible, however as was found in section 2.8, the approximate thickness of water at the right temperature is about 0.54 nm. Since at the peak water temperature of about 319°C the intermolecular distance is about 0.36 nm, this means that the calculated homogeneous and heterogeneous nucleation rates are very similar.

In order to calculate the heterogeneous nucleation rates a very similar method was used to that used for calculating the homogeneous nucleation rates. The temperature values from the same simulations were used, and the temperatures between the grid points were estimated by interpolation. The nucleation rate was then determined by a numerical integration over the surface. The complete program is listed in appendix B.3. The homogeneous nucleation rate and the total nucleation rate for the case of a Gaussian beam are shown as a function of the peak water temperature in figure 2.14. The same quantities for the case of a third order Gauss-Laguerre beam are shown in figure 2.15.

We see that the relation between the homogeneous and heterogeneous nucleation rates is the same for the Gaussian and Gauss-Laguerre beams, except the temperatures for the Gauss-Laguerre beam are uniformly about 1°C lower than the temperatures for the Gaussian beam, due to the greater area of the surface that is near the nucleation temperature for the case of the Gauss-Laguerre beam.

Figure 2.14: The nucleation rates as a function of peak water temperature for a Gaussian beam. The homogeneous nucleation rate is shown in green, the total nucleation rate assuming a contact angle of 0° is shown in red, and the total nucleation rate assuming a contact angle of 90° is shown in blue.

From figures 2.14 and 2.15, even though the heterogeneous nucleation rate for a contact angle of 0° is comparable to the homogeneous nucleation rate, it only decreases the nucleation temperature by approximately 0.2°C, which is negligible as compared to other uncertainties.

The nucleation rates for the case $\phi = 90°$ are also shown in figures 2.14 and 2.15. From these plots we can see that in both the Gaussian and Gauss-Laguerre cases the nucleation temperature is about 9°C below the nucleation temperature for homogeneous nucleation alone. This is a significant reduction, and the significant difference between the theoretical and experimentally measured nucleation temperatures for water is usually attributed to this.

If larger contact angles are assumed, then the nucleation temperature is reduced even further. In the case $\phi = 180°$ (the surface is completely non-wetting) we find that no superheat is required before nucleation begins. In practice the contact angle is not usually above 90°, however, so we should not expect heterogeneous nucleation to reduce the temperature much more than 9°C.

It must be added that in this case of an extremely thin superheated layer, it is rather
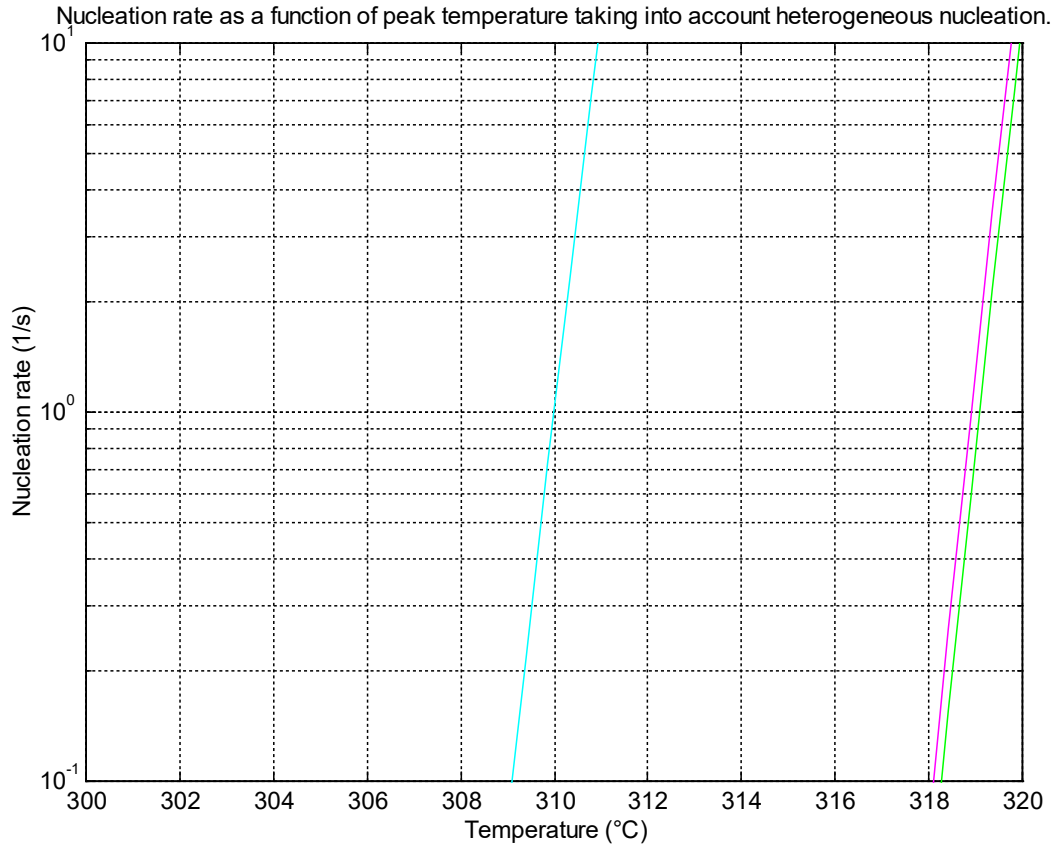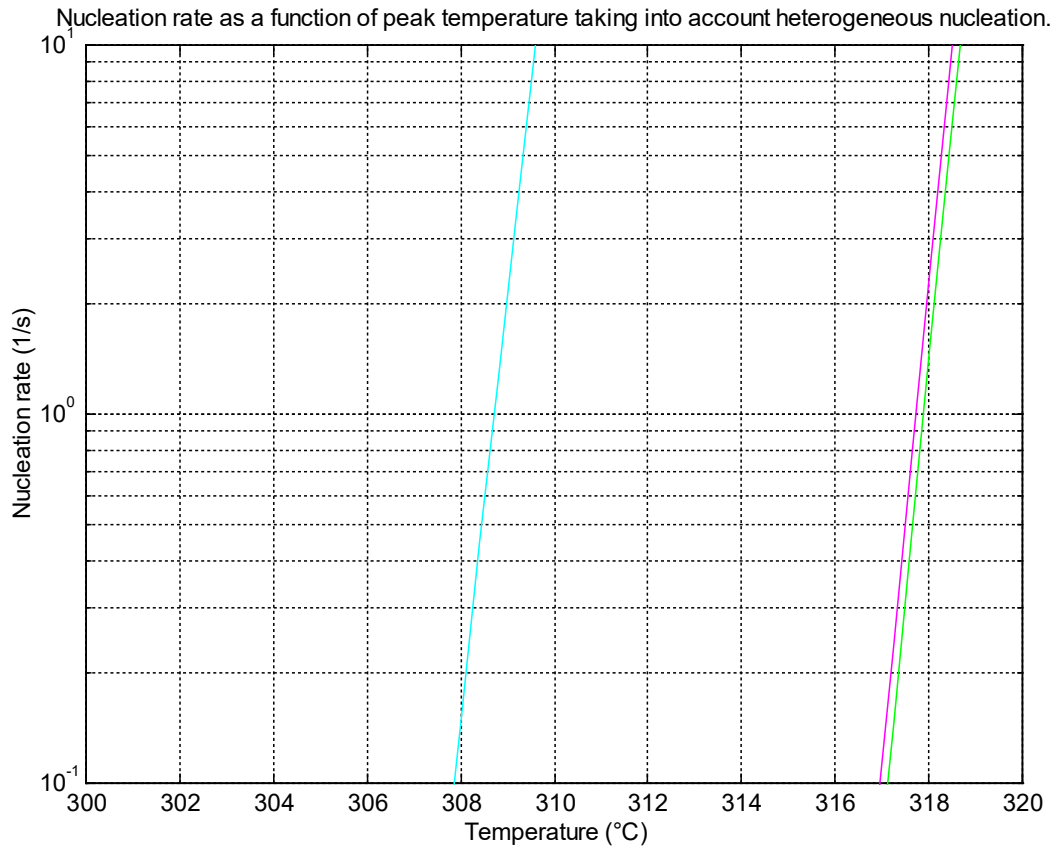
Figure 2.15: The nucleation rates as a function of peak water temperature for a third order Gauss-Laguerre beam. The homogeneous nucleation rate is shown in green, the total nucleation rate assuming a contact angle of 0° is shown in red, and the total nucleation rate assuming a contact angle of 90° is shown in blue.

questionable how valid the formulae for homogeneous and heterogeneous nucleation rates are. The most obvious objection is that the liquid molecules at the surface of the solid are considered as possible centres of nucleation both in the heterogeneous nucleation formula and the homogeneous nucleation formula. Usually this would not be significant, however since the temperature gradient is so great the molecules in the surface layer form a significant contribution to the calculated homogeneous nucleation rate.

This problem cannot be simply eliminated by ignoring the first layer of molecules in the integration for the total homogeneous nucleation rate. This is because the superheated layer is so thin that bubbles that nucleate in the bulk of the liquid will almost always be in contact with the surface of the solid before they reach critical radius. For the simulation above, the homogeneous rate calculated using the formula drops by 50% in about 0.54 nm. This means that most of the bubbles formed by homogeneous nucleation should be centred within a distance of about 1 nm from the surface. Even at 319°C, however, the critical bubble radius is well above this, at about 2.4 nm. This effect is reinforced by the fact that bubbles are attracted

to regions of higher temperature (see section 3.3).

It therefore appears that even nucleation in the bulk simply contributes to the heterogeneous nucleation, and that true homogeneous nucleation is negligible. The problem of how to modify the formula to take account of this is not trivial. One problem is that the contact angle of the bubble may tend to vary depending on where it formed. For example, if the bubble nucleates at about 2.4 nm from the surface, then it will only just be in contact with the surface when it reaches the critical radius. The contact angle will then be zero for this bubble irrespective of how wetted the surface is. A further problem is that the conditions will vary greatly over the width of the bubble. The temperature varies by about 2°C over the width of a critical size bubble, and the homogeneous nucleation rate drops by about 300 times with this drop in temperature.

As a rough estimate of how far these effects influence the nucleation temperature, the radius of the critical size nucleus is about 7 times the width of a molecule, so the effect of molecules away from the interface acting as centres of nucleation should not increase the nucleation rate more than about 7 times, equivalent to a decrease in the nucleation temperature of about 0.7°C. Since the temperature drops by about a degree over the width of the critical size bubble, we should not expect the effect of the temperature gradient to increase the maximum possible superheat by more than about a degree. Since these effects are opposite, we should not expect these effects together to alter the nucleation temperature by more than about 1°C. These effects therefore should not affect the nucleation temperature significantly.

2.10.2 Nucleation at a liquid-liquid interface

Firstly note that the toner softens over a range of temperatures, rather than melting at a specific temperature. It is therefore unclear at what point the interface can be considered a liquid-liquid interface rather than a solid-liquid interface. Using the formula for heterogeneous nucleation at a solid-liquid interface we get nucleation temperatures above 300°C, unless very large contact angles are assumed. At these very high temperatures the toner should be completely liquid. Therefore, at nucleation the toner can be considered to be liquid, and the formula for heterogeneous nucleation at a liquid-liquid interface can be used. In this case the formula for the nucleation rate is the same as equation (2.44), except the parameters ψ and ω are given by [34, 35, 36]

$$\psi = (1 - m_1)/2$$

$$\omega = \left[\left(2 - 3m_1 + m_1^3\right)\sigma_1^3 + \left(2 - 3m_2 + m_2^3\right)\sigma_2^3\right]/4\sigma_1^3 \qquad (2.48)$$

where

$$m_1 = \left(\sigma_1^2 - \sigma_2^2 + \sigma_{12}^2\right)/\left(2\sigma_1\sigma_{12}\right)$$

$$m_2 = \left(\sigma_2^2 - \sigma_1^2 + \sigma_{12}^2\right)/\left(2\sigma_2\sigma_{12}\right) \qquad (2.49)$$

and σ_1, σ_2, and σ_{12} are the surface tensions of the volatile liquid (water), the non-volatile liquid (liquefied toner) and the interfacial tension, respectively.

There are in general three different cases. Firstly, if $\sigma_2 > \sigma_1 + \sigma_{12}$, then the nucleation forms as homogeneous nucleation, since it requires less work to form a bubble in the volatile liquid than at the interface. In the case $\sigma_1 > \sigma_2 + \sigma_{12}$ nucleation occurs most readily inside the non-volatile liquid. Since the vapour consists of molecules of the volatile liquid, there must be some mechanism for injecting molecules of the volatile liquid into the bubble. This occurs either by bubble blowing, where the bubble has a very small opening onto the volatile liquid, or by diffusion of molecules of the volatile liquid into the non-volatile liquid. Only in the case $\sigma_2 - \sigma_{12} < \sigma_1 < \sigma_2 + \sigma_{12}$ does nucleation occur on the interface, so that the above equation holds.

Note that in the case of a liquid-liquid interface the same considerations hold as in the case of a solid-liquid interface, in that bubbles formed by nucleation in the bulk of the volatile liquid merely contribute to the heterogeneous nucleation, because nucleation will almost always occur closer to the interface than the radius of a critical size bubble. This means that even in the case $\sigma_2 > \sigma_1 + \sigma_{12}$, the nucleation will effectively be heterogeneous. In the case of nucleation in the non-volatile liquid, however, the temperature increases with distance from the interface, so nucleation will tend to occur further away from the interface. This is offset, however, by the decreasing diffusion of molecules of the volatile liquid into the non-volatile liquid with distance from the interface.

The surface tension of water is known, however there is no data available for the surface tension of the toner or for the interfacial tension between the toner and water. The measurement of the surface tension and interfacial tension require specialised equipment (see [36] for a summary of the various measurement techniques), especially since the appropriate temperature range is well above the boiling point of water. As the equipment required for these types of measurements was not available, it was not possible to determine theoretical values for the nucleation rate.

We know, however, that the surface tension of water is unusually high, well above the surface tension of all common liquids except for mercury (see [23] pages **6**-147 to **6**-150). It is therefore unlikely that the surface tension of the toner is higher than the surface tension of water, and we can be reasonably confident that the case $\sigma_2 > \sigma_1 + \sigma_{12}$ does not hold.

It is possible that the case $\sigma_2 - \sigma_{12} < \sigma_1 < \sigma_2 + \sigma_{12}$ holds, even if the surface tension of the toner is somewhat lower than the surface tension of water. Since the values of σ_2 and σ_{12} are unknown, values will be guessed and used to obtain an order of magnitude estimate of how much the heterogeneous nucleation affects the nucleation temperature. The surface tension of many liquids is around half that of water [23], so it will be assumed that the surface tension of the toner is half that of water. In figure 2.16 the maximum water temperature when the total nucleation rate (as determined by an integration over the surface) reaches 1 s^{-1} is plotted as a function of the interfacial tension for the case of a Gaussian beam. Note that ψ and ω are unchanged when σ_1, σ_2, and σ_{12} are all multiplied by a constant factor. Therefore the
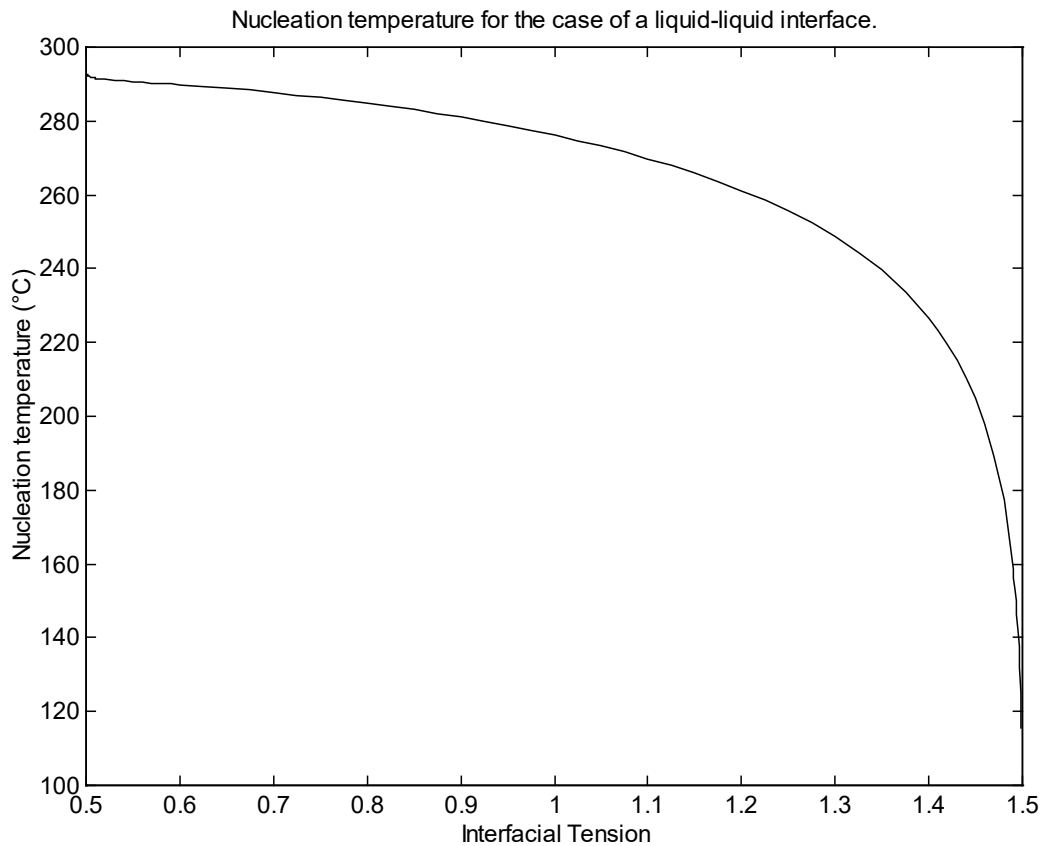

Figure 2.16: The maximum water temperature when the heterogeneous nucleation rate reaches 1 s^{-1} as a function of the ratio between the interfacial tension and the surface tension of water when the surface tension of the toner is assumed to be half the surface tension of the water.

37

interfacial tension is given as a multiple of the surface tension of the water. (The plot for the case of a Gauss-Laguerre beam is identical, except the temperatures are reduced by approximately a degree.)

The full range of σ_{12} from $\sigma_1 - \sigma_2$ to $\sigma_1 + \sigma_2$, is shown in the above plot. It is unlikely that σ_{12} exceeds the surface tension of water, however, so that case will not be discussed. For $\sigma_{12} < \sigma_1$ we can see that the nucleation temperature is reduced by between 30°C and 40°C. This is a significant reduction, and much greater than the reduction in the nucleation temperature due to heterogeneous nucleation at a solid-liquid interface.

Now in the case $\sigma_1 > \sigma_2 + \sigma_{12}$ the bubbles tend to form in the non-volatile liquid rather than the volatile liquid, which is what was observed experimentally with toner. Also the bubbles observed appeared to be entirely within the toner, without any connection with the water, indicating that the water molecules entered the bubble by diffusion rather than a bubble blowing mechanism.

It is not possible to determine theoretical nucleation rates for this form of nucleation, as it requires knowledge of the diffusion rate. In general, the nucleation rate will be increased by the lower surface tension, however the nucleation rate will be reduced by the scarcity of water molecules in the toner. Judging from the results for other forms of heterogeneous nucleation, it should be expected that the nucleation temperature is not greatly changed from the homogeneous nucleation temperature.

If we use the ratio between the powers at melting and at bubble formation, and the relative temperature between the surface of the particle and the interior from the simulation shown in figure 2.10, then the approximate maximum temperature in the interior of the particle at bubble formation is about 300°C. This is fairly close to the homogeneous nucleation temperature, which is what would be expected from nucleation theory.

2.11 Further Experimentation

The experiments with the melting of toner in water are fairly unsatisfactory, as the melting point of the toner is below that of water, and the level of superheat must be inferred from the relative power between melting and the production of bubbles. The best method of determining the temperature would be with a micron size thermocouple, however none were available at the time of writing. Another method of measuring the possible level of superheat

more accurately is to use other substances with higher melting points.

Other types of toner were tested, however none had melting points above the boiling point of water. A variety of substances that have melting points between 100°C and 320°C and are insoluble in water were tested, but it was found that all of these were either transparent or reflective, and did not absorb the laser light sufficiently to melt.

Another method of measuring the level of superheat possible is using the Curie temperatures of ferromagnetic substances. A variety of fine ferrite powders manufactured by Steward were tested. The particles were trapped with a Gaussian laser beam (trapping is necessary in this case because the particles are not sticky, like the toner particles, and are just kicked out of the beam otherwise), and a small magnet was brought near the slide and rotated. In the absence of the beam the ferrite particles rotate when a magnet is rotated near the slide, and if the particles are heated above their Curie points they should stop responding to the magnet.

It was found that when individual particles were trapped it was not possible to heat them sufficiently for them to stop reacting to a magnet. This is partially because the beam must be focussed below the particles for trapping, and then much of the beam passes around the sides of the particles. Also the ferrite particles are fairly reflective, so it is difficult to heat them.

It was found that the particles of the ferrite powder acted as individual domains, and lined up in large strings, especially in the presence of the test magnet. If the laser was directed at these strings and the power was gradually increased, it was found that at sufficiently high power the strings fell apart. This may be due to either the force of the laser beam pushing the particles apart, or the beam heating the particles above their Curie point. The ferrite powder with the highest Curie point tested was the 72500 type with a Curie temperature of 225°C. Therefore the observations may indicate superheating to 225°C.

Experiments with ferrite powders were also performed in a variety of other liquids. It was found that the effect of the strings falling apart was sometimes observed even in liquids with homogeneous nucleation temperatures well below the Curie point. For example, in methanol, which has a homogeneous nucleation temperature listed as 193.1°C [29], a similar effect was observed with the 72500 ferrite powder (with a Curie point of 225°C). This indicates that the effect is probably due to the force of the laser rather than heating above the Curie point in methanol. It is possible that the effect is due to heating over the Curie temperature in water, however the experiments in other liquids demonstrate that a similar effect can be observed just from the force of the laser beam.

Experiments were also performed with toner in a variety of liquids other than water. It was

found that toner dissolved in most of the liquids tested at room temperature, and the toner dissolved in many of the liquids at high temperatures rather than melting. Butanol and kerosene were marginal cases. There appeared to be some melting, however the toner was also partially dissolved at the focus of the beam.

The liquids that the toner did not dissolve at all in were methanol, hexafluorobenzene and ethanol. It was found that the toner melted in all of these liquids before bubble formation. This is especially significant in the case of methanol, as the boiling point of methanol is 64.6°C, which is well below the melting point of the toner, and provides direct evidence of superheating. The powers at the focus required for melting along with various other data for example particles are given in table 2.1.

Table 2.1: Data for example particles melted in various liquids.

Liquid	Power at melting (mW)	Power at bubble production (mW)	Particle radius (μm)	Ratio of power transmitted (%)
CH_4O (Methanol)	0.39	1.2	1.49	18.9
C_6F_6 (Hexafluorobenzene)	0.15	0.41	1.53	12.5
C_2H_6O (Ethanol)	0.28	1.47	1.60	24.0

Similar considerations hold for these power measurements as hold for those with water. The uncertainties in the powers at melting are around 5%, due to factors such as the uncertainty in the calibration and the difficulty in determining the point at which the melting becomes visible. The powers at melting were again virtually independent of the particle sizes, and the powers at bubble formation again varied by around 10% to 20%.

Based on the relative powers between melting and bubble formation for these three liquids we find that the temperatures at bubble formation for these three liquids are as given in table 2.2. The lower temperature is that obtained by assuming that the melting point of the toner is 70°C, and the upper limit corresponds to a melting point of 80°C. The boiling points and the highest experimentally measured nucleation temperatures for these liquids as listed in [23] or [29] are also given in table 2.2. The theoretical nucleation temperatures for all liquids other than water agree well with the experimentally measured nucleation temperatures (as listed in [29]), so it is reasonable to use the experimentally measured nucleation temperatures here.

Table 2.2: Nucleation temperatures based on scaling of power for various liquids.

Liquid	Lower Limit (°C)	Upper Limit (°C)	Boiling Point (°C)	Nucleation Temperature (°C)
CH_4O (Methanol)	168	199	64.6	193.1
C_6F_6 (Hexafluorobenzene)	143	169	80.26	194.8
C_2H_6O (Ethanol)	179	213	78.29	198.4

From table 2.2 we can see that the homogeneous nucleation temperatures are in the range of temperatures indicated by the power scaling for methanol and ethanol, but for hexafluorobenzene the homogeneous nucleation temperature is about 30°C above the temperatures indicated by the power scaling. This temperature difference is a bit too large to be accounted for by the uncertainty in the measurements. Judging from figure 2.16, however, heterogeneous nucleation on a liquid-liquid interface can easily reduce nucleation temperatures by this much. Also, note that these calculations use the approximation that the surface temperature is at the melting point when the melting becomes visible, and it is possible that this is a poor approximation for the case of hexafluorobenzene.

Simulations were performed for the temperature distribution for methanol and ethanol (data for the thermal conductivity of hexafluorobenzene was unavailable). For methanol about 40% of the particle is above 80°C, which is reasonable, however the maximum surface and internal temperatures are about 173°C and 210°C respectively, somewhat higher than would be expected for the toner to be softened. For ethanol only about 28% of the particle is above 80°C, however the maximum surface and internal temperatures are still higher than would be expected, at 129°C and 152°C respectively. The predicted powers for bubble formation are 0.44 mW and 0.47 mW for methanol and ethanol respectively, much lower than the experimental values. The predicted temperatures for methanol and ethanol are around 3 times the experimental values, a similar factor to that obtained with water. This indicates that it should be possible to make estimates of the powers required for bubble formation in other liquids simply by determining the power using the method described in section 2.7 and multiplying the result by 3.

Now the surface tensions of methanol and ethanol are about 20 mN·m^{-1} (data for

hexafluorobenzene was unavailable), which is relatively low compared to the surface tensions of other liquids (see [23] pages **6**-147 to **6**-150), and is about a third of the surface tension of water. Therefore it is fairly unlikely that the condition $\sigma_1 > \sigma_2 + \sigma_{12}$ holds (see section 2.10.1), and therefore according to the standard theory it is unlikely that nucleation will occur in the interior of the toner. It was observed that the nucleation usually occurred at the interface for each of these liquids. In methanol, however, it was found that when the laser was directed at the centres of larger particles (over 10 μm), a bubble was sometimes formed in the interior of the particle (see figure 2.17 (a)).
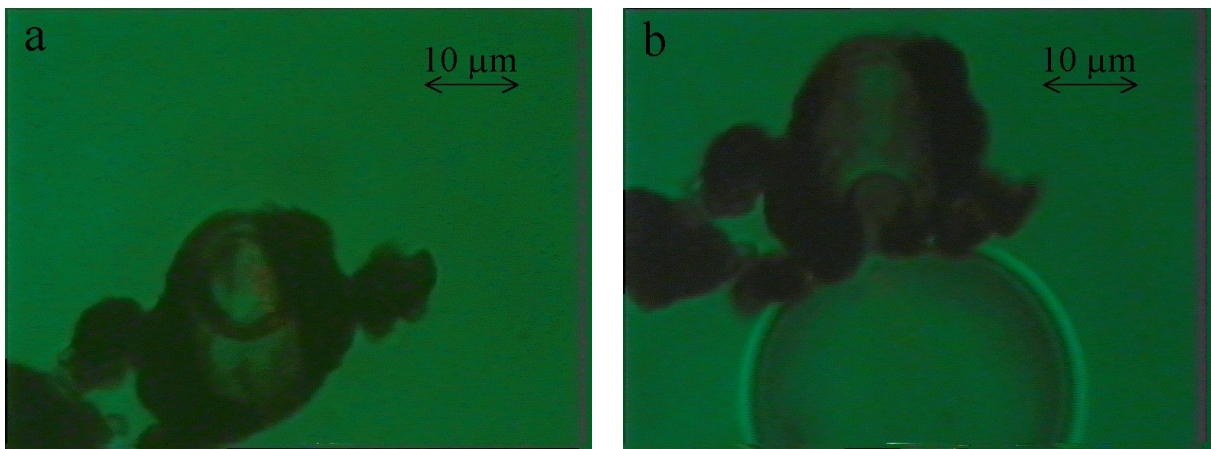

Figure 2.17: A bubble formed in the interior of a toner particle in methanol (a), and a bubble escaping into the surrounding methanol (b).

This appears to be because the interior of the particle is heated to a higher temperature than the surface, rather than because the inequality $\sigma_1 > \sigma_2 + \sigma_{12}$ holds. It was found that if the bubble reached the surface, it escaped out into the water (see figure 2.17 (b)). This would not happen if the inequality $\sigma_1 > \sigma_2 + \sigma_{12}$ held, because then a surface consisting of a thin layer of toner between the liquid and the vapour would have a lower energy than a direct surface between the liquid and the vapour.

In observations with ethanol it was found to be impossible to produce bubbles in the interior of the toner particles. This may be because the surface tension of ethanol is slightly lower than that of methanol, however the difference is only about 1%. Another possibility is that methanol diffuses into the toner far more easily than ethanol.

In hexafluorobenzene it was found that although bubbles could not be seen to form in the interior of the toner particles, the toner particles tended to be destroyed by bubble formation. This may indicate that the bubbles nucleated in the interior of the toner, and immediately

broke into the liquid.

Also it was found that the observations indicating possible decomposition of the toner in water (see figure 2.5) could not be repeated in any of these liquids. In methanol there were some initial observations indicating a similar effect, but after many hours of investigation these observations could not be repeated. This may be due to a slight change in the composition of the toner during the course of the observations (see section 3.1).

The main conclusions that can be drawn from these experiments are firstly that we have direct evidence, from the melting of toner in methanol, that particles can be heated above the boiling point of the surrounding liquid without bubble formation with the laser tweezers apparatus. Secondly the power scaling measurements give reasonable confirmation that the temperature required for bubble formation is fairly close to the homogeneous nucleation temperature in methanol and ethanol, though it may be somewhat lower in hexafluorobenzene. Lastly the calculated temperatures were uniformly around 3 times higher than the experimental values, a similar factor to that obtained in water. This is consistent with about two thirds of the light being reflected from the toner.

Chapter 3: Convection

3.1 Experiment

This study was also prompted by observations that when a bubble was formed next to a copper oxide particle trapped by the laser tweezers apparatus in kerosene, the particles near the trapped particle rapidly moved over to the bubble and came to rest against it. In the absence of a bubble, no motion was observed, except for a very gradual motion when copper oxide particles were trapped in water with detergent added.

Upon further investigation, it was observed that this effect occurred when trapping copper oxide particles in water or kerosene. Some examples of this are shown in figure 3.1. (All experiments are with a Gaussian beam.) This was also observed to a lesser extent with toner particles, but was less noticeable due to the larger size of the toner particles and the tendency of toner particles to stick to the microscope slide.
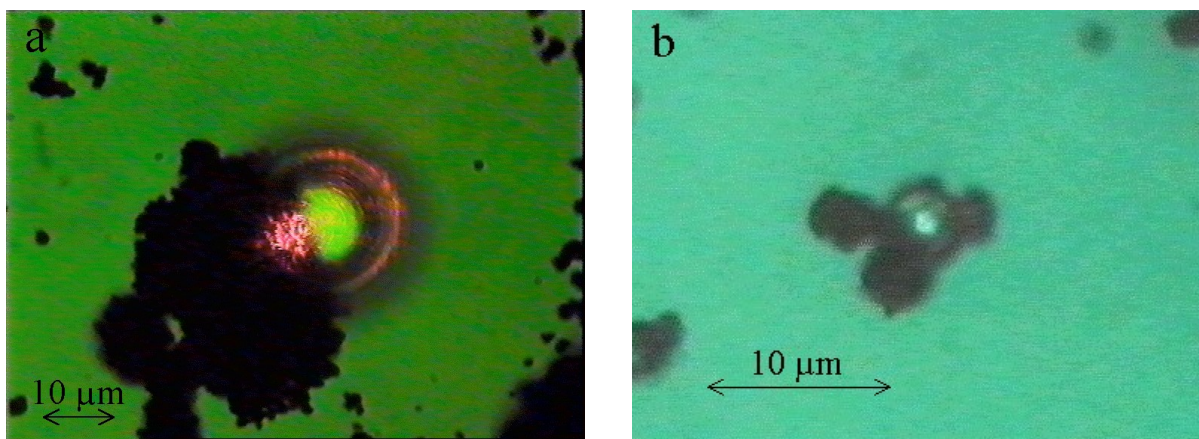
Figure 3.1: Copper oxide particles attracted to a bubble in water (a) and kerosene (b). The power in (a) is about 8.6 mW, and the power in (b) is about 2.6 mW.

Upon further observation the gradual motion in the absence of a bubble was only significant in the case of copper oxide particles in water with detergent added. An example of this is shown in figure 3.2. The power at the focus was approximately 7.8 mW in this case, but the reflectivity must have been high, or else there would have been bubble production. The

maximum velocities of the particles observed was about 10 $\mu\text{m·s}^{-1}$. In the case of copper oxide particles in kerosene or in water without detergent, there was sometimes a very slight motion towards the heated particles, but the velocities observed were less than about 1 $\mu\text{m·s}^{-1}$.
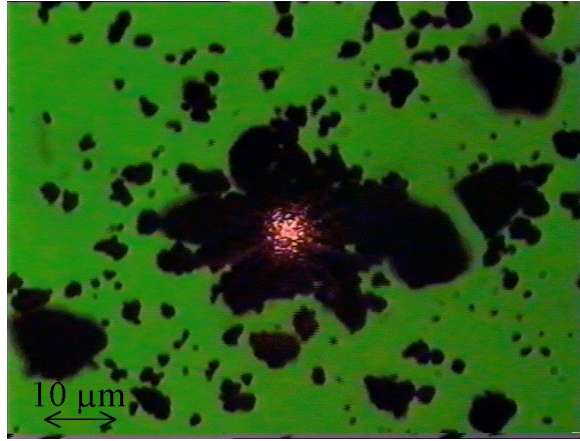
Figure 3.2: Copper oxide particles attracted to a heated particle in water with detergent added.

These observations are apparently due to convection currents that are strong when there is a bubble present, but are very weak otherwise. In order to observe the convection currents, toner particles were dissolved in hexane. The carbon black pigment contained in toner consists of particles on the order of 0.1 μm or less. These particles are sufficiently small that they are moved along with any convection currents, but are sufficiently large for their motion to be detectable. Some debris remaining from the toner was heated and the shape of the convection was observed using the carbon black pigment. An example of this is shown in figure 3.3 (a). The direction of the convection is indicated with arrows. In figure 3.3 (a) the qualitative motion of the fluid is circulation, rather than uniform motion in one direction.

Figure 3.3: Convection currents around a bubble near a heated particle in hexane (a). This image has been processed to enhance the convection currents. A bubble near a heated particle in acetone is shown in (b). The power in (b) is 0.36 mW.

This qualitative feature of the flow was observed independently of the power, the distance between the heat source and the bubble, and the type of fluid.

In later observations the toner dissolved very poorly in hexane, and when it did dissolve it left a large amount of sticky debris. This change is probably due to a change in the formu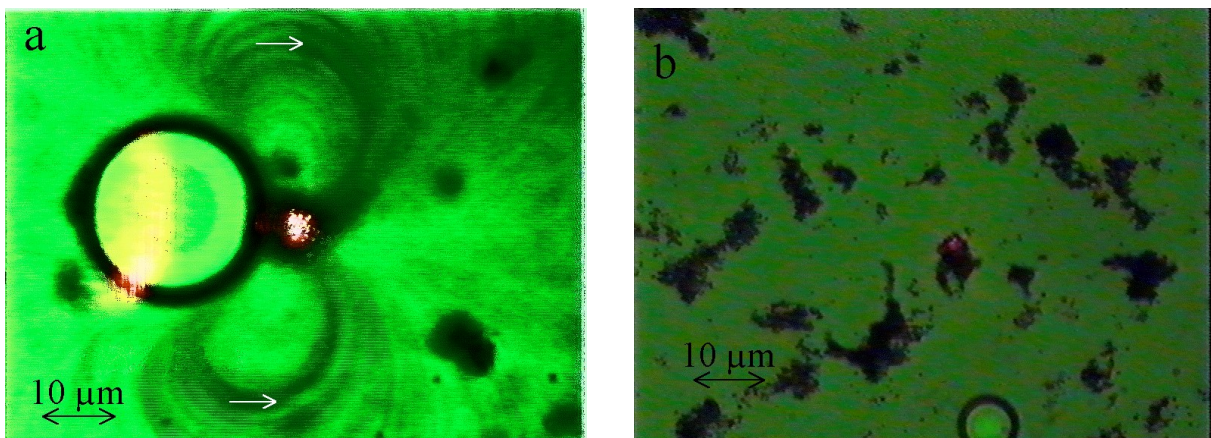lation of the toner that reduces its solubility. Observations were still possible with acetone, however the debris from the toner clumped very quickly, making observations difficult. An example of a bubble in acetone where the convection currents were slow enough to measure is shown in figure 3.3 (b). The bubble is visible at the bottom-centre of the image, but the convection is too slow to be visible. The particles moving the fastest in this image moved about 10 μm between frames, corresponding to a velocity of at least 0.24 mm·s^{-1}.

It was also observed that some convection occurred in the absence of heating from the laser. This was symmetric around the bubbles, and consisted of a rolling motion, with the liquid closest to the bubble moving upwards. The geometry of this is shown in figure 3.4. This convection was far slower than the convection shown in figure 3.3. This convection slowed down when the light from the condenser was reduced, and can therefore be attributed to the light from the condenser.
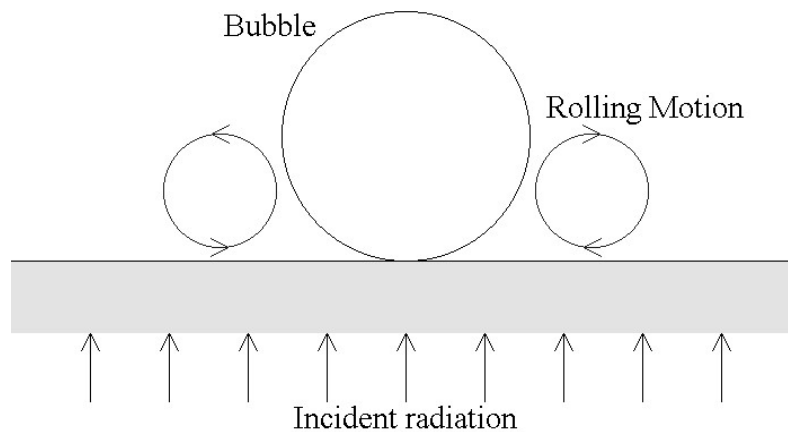
Figure 3.4: Rolling motion around a bubble due to heating by the condenser light.

Also it was observed that the bubbles were attracted to the beam, rather than repelled by it. According to optical trapping theory, it is not possible to trap low-index particles with a Gaussian beam. Previously low-index particles have only been trapped with a scanned Gaussian beam [5] or a Gauss-Laguerre beam [8]. Also it was noticed that small bubbles were attracted to a heated particle even when they were tens of micrometres away. An example of this is shown in figure 3.5. The images shown are successive frames, showing that the bubble has moved about 10 μm in 40 ms or less. This corresponds to a speed of at

least 0.24 mm·s^{-1}.
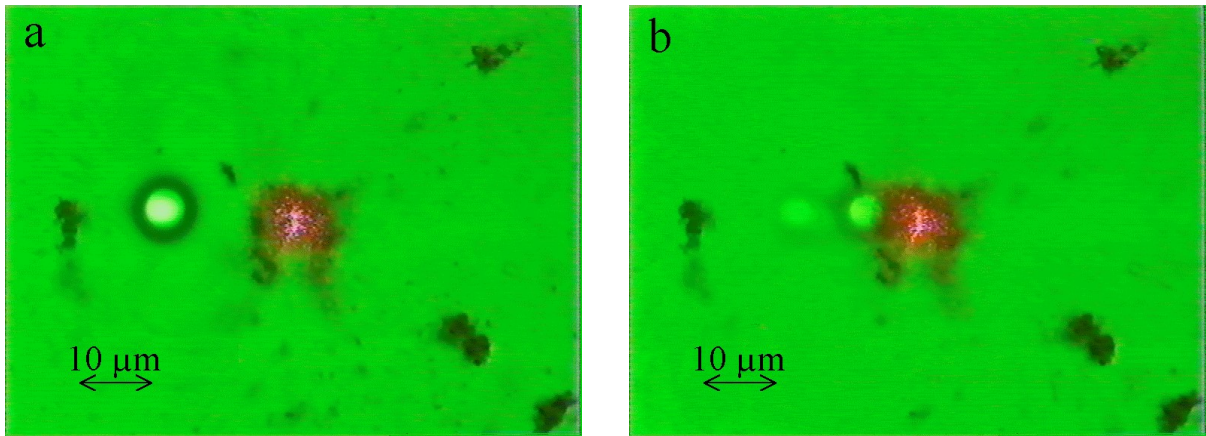
Figure 3.5: A small bubble being drawn towards a heated particle. Images (a) and (b) are successive frames.

The attraction was observed only when a particle was heated, and not when the beam was focussed on the glass. This indicates that the attraction is due to the heat, rather than the optical forces. In order to test how strong this attraction is, a painted slide was used. The paint allows the beam to produce heating regardless of where it is pointed, so the maximum speed the beam can move the bubble can be measured. It was found that bubbles could be moved by the beam almost as fast as it is possible to move the stage, on the order of 1 mm·s^{-1}. This is remarkably fast, an order of magnitude greater than the greatest speeds achieved in optical trapping with a beam of this power [13]. Also the limiting factor to the speed appeared to be due to irregularities in the paint knocking the bubble to the side, rather than viscous drag. The heat produced by the beam therefore appears to provide a much stronger trapping mechanism than normal optical trapping.

3.2 Surface Tension Driven Convection

The reason that substantial convection is observed when there is a bubble, but little or none is observed in the absence of a bubble, is that it is possible for convection to be driven by surface tension. This is known as Marangoni convection. The possibility that convection currents could be driven by surface tension gradients due to thermal gradients was first investigated by Hershey [37]. The importance of surface tension driven convection was first made clear by the interpretation of the convection cells observed by Bénard in 1901 [38]. In 1916 Rayleigh performed an analysis on the stability with respect to buoyancy driven

convection of a fluid layer heated from beneath [39]. According to Rayleigh's analysis, the vertical temperature gradient must attain a certain minimum value for marginal stability and exceed it for instability to occur. The gradients in Bénard's experiments were at least tenfold less than that required by Rayleigh's theory, however this was not noticed until 1925 (see Low and Brunt [40]).

Another conflict between the theory and experiment was that upwelling of the hot liquid was beneath the centres of depression of the free surface of the pool, and in buoyancy driven flows the free surface over an upwelling current is generally elevated, as Jefferys showed in 1951 [41]. In 1956 Block [42] repeated Bénard's experiments, and confirmed that convection occurred when the temperature gradient was about an order of magnitude smaller than that required by theory. In addition he observed convection in a layer of liquid cooled from below, and he also observed that putting a layer of silicone on surface of the pool cut convection to half. He concluded that the convection was driven by surface tension. In 1958 Pearson [43] demonstrated theoretically that surface tension forces are sufficient to cause hydrodynamic instability in a liquid layer with a free surface.

Qualitatively the motion expected in surface tension driven convection should be away from the heated region at the free surface. This is what was observed when heating with the laser (see figure 3.3 (a)). For the convection due to heating by the condenser, the temperature should be highest near the lower slide. Therefore, from figure 3.4, we can see that the convection was moving in the expected direction in this case also.

3.3 Bubble Migration

Since surface tension gradients can induce flows, it is reasonable that there will be a force on a bubble in the presence of a thermal gradient. In 1959 Young *et. al*. [44] showed experimentally that temperature gradients can induce a force on an air bubble, and derived an expression for the relationship between the vertical temperature gradient and the velocity of rise of a bubble (when typographical errors are corrected):

$$v_0 = -\frac{1}{\eta}\left[\eta\gamma' R T_c - (\rho - \rho')gR^2(\eta + \eta')\right](3\eta + 2\eta')^{-1} \qquad (3.1)$$

where $$T_c = 3T_1 / (2 + h'/h)$$

and v_0 is the velocity of rise, η and η' are the viscosities outside and inside the bubble

respectively, γ is the thermal coefficient of surface tension, R is the bubble radius, T_1 is the temperature gradient (dT/dz) at a large distance from the bubble, h and h' are the thermal conductivities outside and inside the bubble respectively, ρ and ρ' are the densities outside and inside the bubble respectively, and g is the gravitational acceleration. This solution is in the approximation of creeping flow, where the quadratic terms can be ignored in the Navier-Stokes equations, and the effect of the flow on the temperature distribution is negligible.

If the viscosity, density and thermal conductivity of the gas inside the bubble are negligible, then the above expression reduces to

$$v_0 = -\frac{1}{3\eta}\left[\tfrac{3}{2}\gamma' R T_1 - \rho g R^2\right]$$

(3.2)

In the absence of gravity we find that the terminal velocity of the bubble is

$$v_0 = \frac{(-\gamma')R T_1}{2\eta}$$

(3.3)

For most liquids and temperature ranges γ is negative, so the velocity has the same sign as T_1. This means that the bubble moves towards the region of higher temperature.

In order to make an estimate of the terminal velocity when heating with the laser, it is necessary to estimate the thermal gradient. The temperature distribution around a point heat source of power P at the interface between the liquid and the glass is

$$T(r) = \frac{P}{2\pi r\left(h_l + h_g\right)} + T_0$$

(3.4)

where r is the distance from the heat source, h_l and h_g are the thermal conductivities of the liquid and the glass respectively, and T_0 is the ambient temperature. The thermal gradient is therefore

$$\frac{dT}{dr} = -\frac{P}{2\pi r^2\left(h_l + h_g\right)}$$

(3.5)

The thermal coefficient of surface tension is given by taking the derivative of (2.14) with respect to T, and is

$$\gamma' = -\frac{1}{T_c}\left(\tfrac{5}{4}a\tau^{1/4} + \tfrac{9}{4}b\tau^{5/4} + \tfrac{13}{4}c\tau^{9/4}\right)$$

(3.6)

The formula used here is (2.14) rather than (2.13), because (2.14) is more accurate for substances other than water. Now consider the example of the bubble shown in figure 3.5. The bubble radius is 3.7 μm and the distance from the heat source is 18.7 μm. For hexane the constants for equation (3.6) are

$$T_c = 507.50 \text{ K}$$

$$a = 52.2937 \text{ mN·m}^{-1}$$

$$b = 6.1685 \text{ mN·m}^{-1}$$

$$c = -3.5869 \text{ mN·m}^{-1}$$

The thermal conductivity of hexane is about 0.120 W·m^{-1}K^{-1} at 25°C. In the example shown in figure 3.4 the power was being varied, so the exact power is unknown, but in order to make an order of magnitude calculation, the power can be estimated at about 1 mW. Then using equation (3.4) the temperature at the position of the bubble should be approximately 45°C. The thermal coefficient of the surface tension is then about -1.06x10^{-4} N·m^{-1}K^{-1}, and the thermal gradient is about 1.12×10^6 K·m^{-1}. The viscosity of hexane varies with temperature and is about 0.300 mPa·s at 25°C and about 0.240 mPa·s at 50°C. The viscosity should therefore be about 0.251 mPa·s at the position of the bubble, giving the terminal velocity as about 0.88 m·s^{-1}. Considering the scale of the system this is a tremendous velocity, and more than enough to account for the movement observed. Judging from these calculations, the trapping due to the thermal force should be on the order of 10^4 times more powerful than the optical trapping.

In more recent work on the problem of the terminal velocity, the corrections to the bubble velocity due to the quadratic terms in the Navier-Stokes equations and the effect of the flow on the temperature distribution have been found. We define the scaled bubble velocity U by

$$U = v_0 \frac{\eta}{(-\gamma')RT_1} \tag{3.7}$$

We also define the Reynolds, Marangoni and Prandtl numbers by

$$Re = \frac{(-\gamma')T_1 R^2}{\eta v}$$

$$Ma = \frac{(-\gamma')T_1 R^2}{\eta \alpha} \tag{3.8}$$

$$Pr = v / \alpha$$

where v and α are the kinematic viscosity and thermal diffusivity respectively, and are given by

$$v = \eta / \rho$$

$$\alpha = \frac{h}{c_p \rho} \tag{3.9}$$

where ρ is the density and c_p is the specific heat capacity. The Reynolds number is large if the

quadratic terms in the Navier-Stokes equations are significant, the Marangoni number is large if the flow has a significant effect on the temperature distribution, and the Prandtl number is just the ratio between the Marangoni and Reynolds numbers.

Subramanian [45] and Merritt [46] (cited in [47]) found the first two terms in the expansion of U in terms of the Marangoni number, and this correction is

$$U = \tfrac{1}{2} - \tfrac{301}{14400} Ma^2 + \tfrac{13}{1440} Ma^3 + O(Ma^4) \tag{3.9}$$

Balasubramaniam et. al. [48] extended the calculation of the terminal velocity numerically to large Reynolds and Marangoni numbers.

For hexane $\rho = 654.8$ kg·m^{-3} and $c_p = 2270$ J·kg^{-1}K^{-1}. Therefore in the example above the Reynolds number is about 17, the Marangoni number is about 86, and the Prandtl number is about 5.1. From figure 2 of [48] the scaled terminal velocity U is reduced by about 46%. This reduces the terminal velocity to about 0.47 m·s^{-1}, which is not sufficient to alter the above conclusions. Note that the Marangoni number is only significant because the terminal velocity is very high. In less extreme cases, where the terminal velocity is on the order of micrometres per second rather than metres per second, the Reynolds and Marangoni numbers will be on the order of 10^{-6}, and therefore negligible.

Now consider the effect of Marangoni convection on the motion of a critical size bubble. Using the same simulation as in section 2.9, the thermal gradient will be approximately 4.1×10^8 K·m^{-1}, and the radius of a critical size bubble is about 2.4 nm. The Reynolds and Marangoni numbers are about 0.050 and 0.052 respectively, and so may be neglected. Using (3.3) the terminal velocity is about 1.3 m·s^{-1}. This is again a tremendous speed, and it is therefore reasonable that bubble migration may have an effect on nucleation.

3.4 Convection Currents Around Bubbles

3.4.1 Convection for Linear Temperature Variation

Now the theoretical flow pattern around the bubble will be considered. Firstly the effect of the slide on the convection will be ignored, as the problem then has rotational symmetry, which simplifies the calculations. In the case that we have Stokes flow (the Reynolds number is negligible) and the heat flow due to convection is negligible (the Marangoni number is negligible), there is a linear temperature gradient at long distances from the bubble and the bubble is stationary, the temperature and flow distributions are given by (see [44]):

$$T = T_0 + T_1\left(r + R^3 / 2r^2\right)\cos\theta$$
$$u_r = 2(a / \eta)\left(r^{-1} - R^2 r^{-3}\right)\cos\theta \tag{3.11}$$
$$u_\theta = -(a / \eta)\left(r^{-1} + R^2 r^{-3}\right)\sin\theta$$

where R is the radius of the bubble, a is a constant, T_1 is the temperature gradient at infinity, and η is the viscosity. Using the boundary conditions a can be found to be

$$a = \tfrac{1}{4} R^2 \gamma' T_1 \tag{3.12}$$

where γ is the thermal coefficient of surface tension.

This solution can be used to obtain an estimate of the convection velocities. The maximum velocity of the fluid is

$$v_{max} = \frac{(-\gamma')RT_1}{2\eta} \tag{3.13}$$

If there is a point heat source of power P at a distance d from the centre of the bubble then the temperature gradient is approximately

$$T_1 = \frac{P}{2\pi\left(h_l + h_g\right)d^2} \tag{3.14}$$

This expression takes account of the effect of the slide on the temperature distribution, however the effect of the slide on the flow distribution will still be ignored. The maximum velocity of the fluid is then

$$v_{max} = \frac{(-\gamma')PR}{4\pi\left(h_l + h_g\right)\eta d^2} \tag{3.15}$$

If the point heat source is n times the radius of the bubble from the centre of the bubble, then

the maximum velocity is

$$v_{max} = \frac{(-\gamma')P}{4n^2\pi\left(h_l + h_g\right)\eta R}$$

(3.16)

Thus the flow velocity scales in proportion to the power and in inverse proportion to the scale of the system. This is the reason why the convection is so noticeable at the size scales involved in optical trapping. Now consider the example of the configuration shown in figure 3.3 (b). The bubble radius is about 3.8 μm, the power is about 0.36 mW and the distance of the heat source is about 24.8 μm. The values of the various constants for acetone are

$$\gamma' = -1.12 \times 10^{-4} \text{ N·m}^{-1}\text{K}^{-1}$$

$$h_l = 0.160 \text{ W·m}^{-1}\text{·K}^{-1}$$

$$\eta = 0.306 \text{ mPa·s}$$

These values lead to a maximum flow rate of about 49 mm·s^{-1}. This is about 200 times the observed flow velocity of about 0.24 mm·s^{-1}, indicating that this level of approximation gives a rather poor estimate of the flow velocities.

The temperature contours and flow lines obtained from equation (3.11) are as in figure 3.6. As you can see, there is no circulation of the fluid, which indicates that this level of approximation is insufficient to give the circulation observed. The next level of approximation is to solve the problem with a point heat source but still ignore the slide.
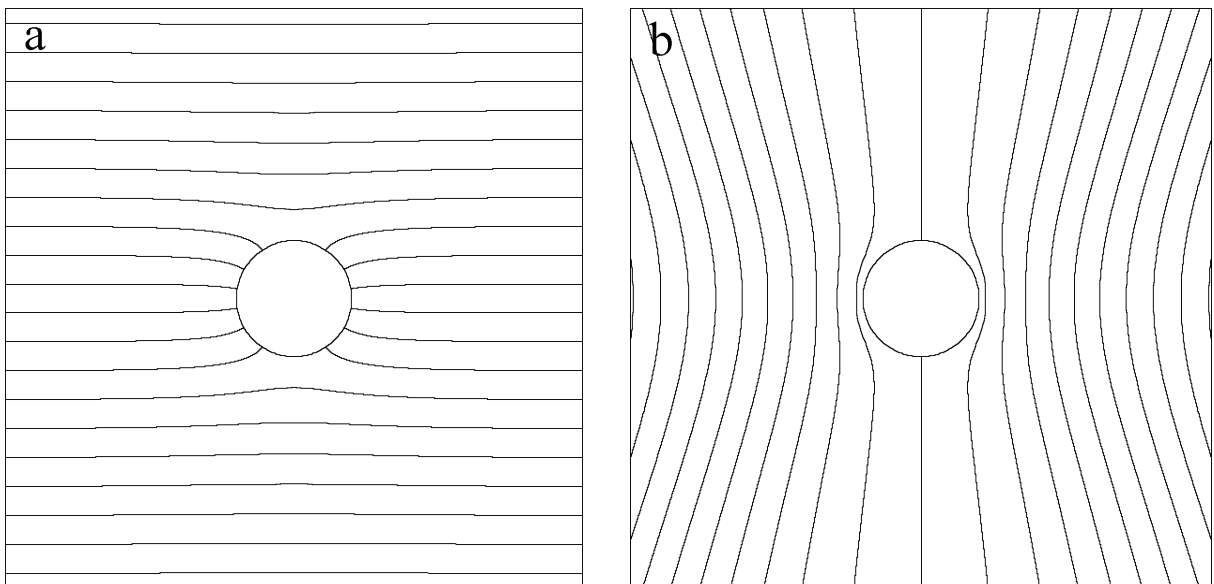
Figure 3.6: The temperature distribution (a) and streamlines (b) around a heated bubble.

3.4.2 Temperature distribution for point heat source near bubble

We can determine the temperature distribution by numerically solving the differential equations in a similar way as in section 2.7. The differential equation for the system is, except at the position of the heat source,

$$\nabla^2 T = 0 \tag{3.17}$$

If we assume that the thermal conductivity of the gas inside the bubble is negligible, and we use spherical polar coordinates with the origin at the centre of the bubble and so that the heat source is at $\theta = 0$, then the boundary conditions are

$$\left. \frac{\partial T}{\partial r} \right|_{r=R} = 0 \tag{3.18a}$$

$$\left. T \right|_{r=\infty} = T_0 \tag{3.18b}$$

$$\left. \frac{\partial T}{\partial \theta} \right|_{\theta=0} = 0 \tag{3.18c}$$

$$\left. \frac{\partial T}{\partial \theta} \right|_{\theta=\pi} = 0 \tag{3.18d}$$

where R is the radius of the bubble. Now the temperature distribution is the sum of the temperature distribution that would exist with just a point heat source, T_a, and a correction due to the bubble, ΔT. In the numerical method it is more accurate to solve for the correction due to the bubble, then add on the analytic solution, because then there is no singularity in the numerical mesh. The temperature distribution that would exist with just the point source is

$$T_a = \frac{P}{4\pi h \left[r^2 + d^2 - 2rd \cos\theta \right]^{\frac{1}{2}}} + T_0 \tag{3.19}$$

where P is the power dissipated, h is the thermal conductivity, d is the distance between the centre of the bubble and the heat source and T_0 is the temperature at infinity. We therefore find for this temperature distribution that

$$\left. \frac{\partial T_a}{\partial r} \right|_{r=R} = \frac{P(d \cos\theta - R)}{4\pi h \left[R^2 + d^2 - 2Rd \cos\theta \right]^{\frac{3}{2}}} \tag{3.20}$$

Therefore, from the boundary condition (3.18a), the boundary condition that the correction to the temperature distribution must obey at the surface of the bubble is

$$\left.\frac{\partial \Delta T}{\partial r}\right|_{r=R} = \frac{P(R - d\cos\theta)}{4\pi h \left[R^2 + d^2 - 2Rd\cos\theta\right]^{3/2}} \tag{3.21a}$$

The boundary condition (3.18b) becomes

$$\left.\Delta T\right|_{r=\infty} = 0 \tag{3.21b}$$

The two other boundary conditions are the same for the correction, so we have

$$\left.\frac{\partial \Delta T}{\partial \theta}\right|_{\theta=0} = 0 \tag{3.21c}$$

$$\left.\frac{\partial \Delta T}{\partial \theta}\right|_{\theta=\pi} = 0 \tag{3.21d}$$

In the discretisation calculations were performed on the annular region $R \leq r \leq L+R$, $0 \leq \theta \leq \pi$, with the infinity conditions being applied at $r = L\text{-}1$. An equally spaced mesh was used where

$$r_i = R + i\Delta r \qquad i=0,1,...,I \qquad \theta_j = j\Delta\theta \qquad j=0,1,...,J \tag{3.22}$$

where

$$\Delta r = \frac{L}{I} \qquad \Delta\theta = \frac{\pi}{J} \tag{3.23}$$

The differential equation for the temperature is discretised to equation (2.35), and the boundary conditions are discretised using an expression of the form of equation (2.40).

  Each of the discretised equations was again represented by a line of a sparse matrix in Matlab, and solved using the inbuilt matrix routines of Matlab. Again the boundary conditions overlap at the corners, and one boundary condition must be ignored at each of the corners. In the program the boundary condition (3.21c) was used at $r = R$, $\theta = 0$, (3.21d) was used at $r = R$, $\theta = \pi$, and (3.21b) was used at $r = \infty$, $\theta = 0$ and $r = \infty$, $\theta = \pi$.

  The correction given by the above method is then added to the analytic solution in the absence of the bubble given by equation (3.19) to give the total temperature distribution. The complete program is listed in appendix B.5. The program was run with the distance of the heat source as $d = 2R$ and the boundary distance as $L = 6.1R$, and the isotherms of the resulting temperature distribution are as shown in figure 3.7.

3.4.3 Flow pattern using Gegenbauer polynomials

Given an arbitrary temperature distribution around the bubble there is an analytic solution for the flow distribution. This was first found by Levan et. al. in 1976 [49], in the context of
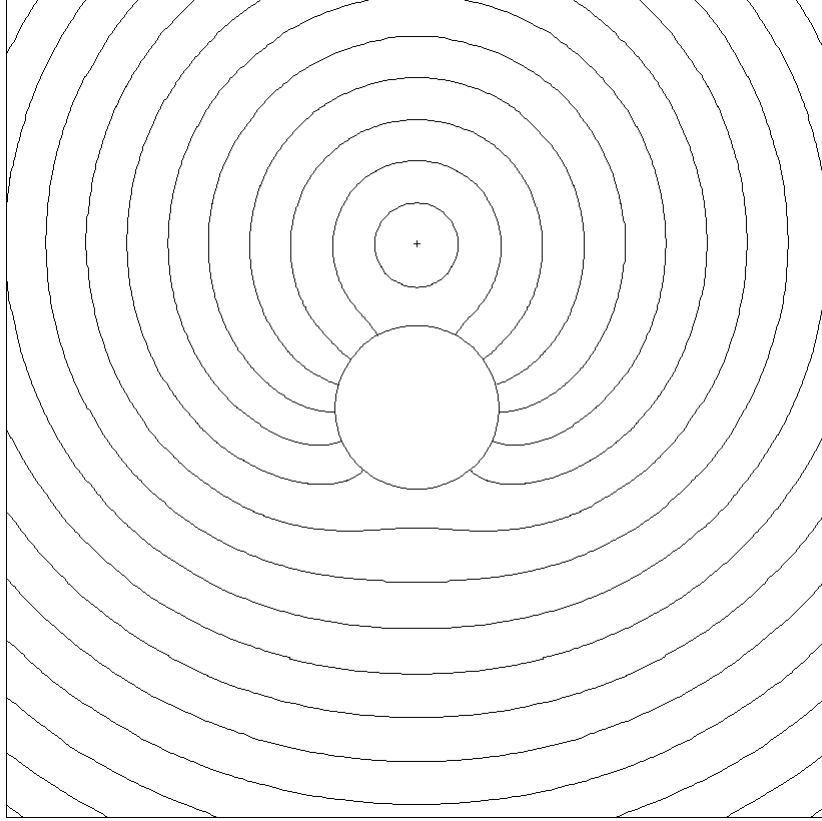
Figure 3.7: Isotherms of the temperature distribution around a heated bubble for a point heat source. The position of the point heat source is shown by a cross. The isotherms are not equally spaced in order to make the effect of the bubble on the temperature distribution more clear.

surfactants, and was applied to the case of thermal gradients by Subramanian in 1981 [45]. The streamfunction is, ignoring scaling factors,

$$\psi(r,\mu) = \frac{1}{4}\left(1-\mu^2\right)I_2\left(\frac{1}{r}-r^2\right) + \frac{1}{4}\sum_{n=3}^{\infty}n(n-1)I_n\left(\frac{1}{r^{n-1}}-\frac{1}{r^{n-3}}\right)C_n^{-\frac{1}{2}}(\mu) \qquad (3.24)$$

where $\mu = \cos(\theta)$, $C_n^{-\frac{1}{2}}(\mu)$ are Gegenbauer polynomials, and the radius r is normalised so that the bubble radius is 1. The radial and tangential velocities are found from the streamfunction as

$$u_r = \frac{1}{r^2\sin\theta}\frac{\partial\psi}{\partial\theta}$$
$$u_\theta = -\frac{1}{r\sin\theta}\frac{\partial\psi}{\partial r} \qquad (3.25)$$

The coefficients I_n are found from the temperature field by the integration

$$I_n = -\int_{-1}^{1}C_n^{-\frac{1}{2}}(\mu)\frac{\partial T}{\partial\mu}(1,\mu)d\mu \qquad n\geq 2 \qquad (3.26)$$

For the properties of the Gegenbauer polynomials see [50]. The Gegenbauer polynomials are

given by

$$C_n^v(z) = \sum_{l=0}^n \frac{(-2)^l \Gamma(v+l)\Gamma(n+2v+l)(1-z)^l}{l!\Gamma(v)\Gamma(2l+2v)(n-l)!}$$

$$= \left[\Gamma(v)\right]^{-1} \sum_{m=0}^{\leq \frac{1}{2}n} \frac{(-1)^m \Gamma(v+n-m)(2z)^{n-2m}}{m!(n-2m)!}$$

(3.27)

The first few Gegenbauer polynomials of degree -½ are

$$C_0^{-\frac{1}{2}}(z) = 1$$

$$C_1^{-\frac{1}{2}}(z) = -z$$

$$C_2^{-\frac{1}{2}}(z) = \tfrac{1}{2}\left(1-z^2\right)$$

$$C_3^{-\frac{1}{2}}(z) = \tfrac{1}{2}z\left(1-z^2\right)$$

$$C_4^{-\frac{1}{2}}(z) = -\tfrac{1}{8}+\tfrac{3}{4}z^2-\tfrac{5}{8}z^4$$

(3.28)

The above solution is for the case that the bubble is travelling at its terminal velocity with respect to the fluid. In the case that the fluid is stationary at a large distance we must use

$$\psi(r,\mu) = \frac{1}{4}\left(1-\mu^2\right)I_2\left(\frac{1}{r}-r\right) + \frac{1}{4}\sum_{n=3}^{\infty} n(n-1)I_n\left(\frac{1}{r^{n-1}}-\frac{1}{r^{n-3}}\right)C_n^{-\frac{1}{2}}(\mu)$$

(3.29)

If we include the scaling constants the streamfunction is

$$\psi(r,\mu) = \frac{R^2\gamma'}{4\eta}\left[\left(1-\mu^2\right)I_2\left(\frac{R}{r}-\frac{r}{R}\right) + \sum_{n=3}^{\infty} n(n-1)I_n\left(\left(\frac{R}{r}\right)^{n-1}-\left(\frac{R}{r}\right)^{n-3}\right)C_n^{-\frac{1}{2}}(\mu)\right]$$

(3.30)

If we perform a numerical integration of the temperature distribution determined in section 2.4.2 to determine the coefficients I_n, then we get the flow distribution as shown in figure 3.8.

This flow distribution again lacks the circulating flow pattern observed experimentally. Now in order for circulation to be observed, the streamfunction must decrease with radius, and then start increasing again. None of the terms in equation (3.30) has this behaviour, so it is not possible to obtain a circulating flow pattern for any temperature distribution on the surface of the bubble.

If we use this method to determine the theoretical convection velocities for the example of the bubble shown in figure 3.3, we get a maximum convection velocity of 50 mm·s⁻¹. This is only about 2% higher than the velocity obtained in the approximation of a linear temperature gradient.
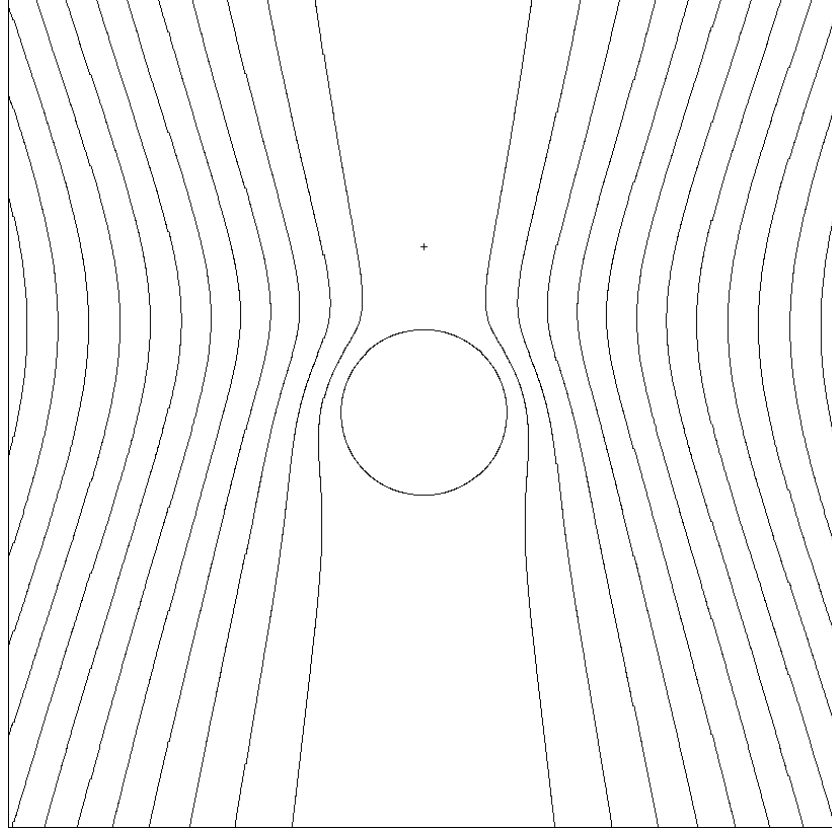
Figure 3.8: The flow distribution around a heated bubble for a point heat source determined using Gegenbauer polynomials. The position of the point heat source is shown by a cross.

3.4.4 Numerically generated flow patterns

The results using Gegenbauer polynomials will now be checked against a numerical flow calculation. Neglecting quadratic terms, the Navier-Stokes equations for the flow are

$$\eta \nabla^2 \boldsymbol{u} = \mathrm{grad}(p)$$
$$\nabla \cdot \boldsymbol{u} = 0 \tag{3.31}$$

where η is the viscosity, $\boldsymbol{u}$ is the flow field and p is the pressure. It is possible to show that these equations are equivalent to the differential equation for the streamfunction

$$\left(\frac{\partial^2}{\partial r^2} + \frac{1}{r^2} \frac{\partial^2}{\partial \theta^2} - \frac{\cot \theta}{r^2} \frac{\partial}{\partial \theta} \right)^2 \psi = 0 \tag{3.32}$$

The appropriate boundary conditions for the streamfunction are

$$\psi \big|_{r=R} = 0 \tag{3.33a}$$

$$\left[\frac{\partial}{\partial r} \left(\frac{1}{r^2} \frac{\partial \psi}{\partial r} \right) \right]_{r=R} = \left[\frac{\sin \theta}{r^2 \eta} \frac{\partial \gamma}{\partial T} \frac{\partial T}{\partial \theta} \right]_{r=R} \tag{3.33b}$$

$$\psi \big|_{\theta=0} = 0 \tag{3.33c}$$

58

$$\left[\frac{\partial \psi}{\partial \theta}\right]_{\theta=0} = 0 \qquad\qquad (3.33\text{d})$$

$$\lim_{r\to\infty}\left[\frac{1}{r^2}\frac{\partial \psi}{\partial \theta}\right] = 0 \qquad\qquad (3.33\text{e})$$

$$\lim_{r\to\infty}\left[\frac{1}{r}\frac{\partial \psi}{\partial r}\right] = 0 \qquad\qquad (3.33\text{f})$$

$$\psi\big|_{\theta=\pi} = 0 \qquad\qquad (3.33\text{g})$$

$$\left[\frac{\partial \psi}{\partial \theta}\right]_{\theta=\pi} = 0 \qquad\qquad (3.33\text{h})$$

The boundary condition (3.33b) above is the term which couples the temperature distribution to the flow distribution. The boundary conditions (3.33e) and (3.33f) do not normally imply that the derivatives of ψ are zero in the limit $r \to \infty$, however in discretising the system the boundary is taken to be at a finite distance rather than infinity, and the derivatives must be zero. The boundary condition (3.33e) is then equivalent to taking $\psi = 0$ at $r = \infty$.

The discretisation was performed in the same manner as for the temperature distribution, as described by (3.22) and (3.23). The derivatives in equation (3.32) were approximated by five point approximations. The five point approximations for derivatives up to fourth order are

$$\frac{dy}{dx}\bigg|_{y=y_n} \approx \frac{1}{\Delta x}\left(\tfrac{1}{12} y_{n-2} - \tfrac{2}{3} y_{n-1} + \tfrac{2}{3} y_{n+1} - \tfrac{1}{12} y_{n+2}\right) \qquad (3.34\text{a})$$

$$\frac{d^2 y}{dx^2}\bigg|_{y=y_n} \approx \frac{1}{(\Delta x)^2}\left(-\tfrac{1}{12} y_{n-2} + \tfrac{4}{3} y_{n-1} - \tfrac{5}{2} y_n + \tfrac{4}{3} y_{n+1} - \tfrac{1}{12} y_{n+2}\right) \qquad (3.34\text{b})$$

$$\frac{d^3 y}{dx^3}\bigg|_{y=y_n} \approx \frac{1}{(\Delta x)^3}\left(-\tfrac{1}{2} y_{n-2} + y_{n-1} - y_{n+1} + \tfrac{1}{2} y_{n+2}\right) \qquad (3.34\text{c})$$

$$\frac{d^4 y}{dx^4}\bigg|_{y=y_n} \approx \frac{1}{(\Delta x)^4}\left(y_{n-2} - 4y_{n-1} + 6y_n - 4y_{n+1} + y_{n+2}\right) \qquad (3.34\text{d})$$

These can be derived by polynomial fitting techniques similar to those used in section 2.7. The derivatives for the boundary conditions were approximated in the same way as in section 2.7. The complete program is listed in appendix B.6. In this program the surface tension is assumed to vary linearly with temperature. Also the program is made more accurate by subtracting the spherically symmetric part of the temperature distribution, and using a numerical derivative for the correction to the temperature distribution, and an algebraic derivative for the spherically symmetric part. The program produces half as many intervals in

the θ direction as is given in the temperature distribution. This is because the calculation of the temperature distribution requires less memory, and more intervals can be used in the θ direction for the temperature distribution to make the numerical derivatives calculated in the program for the velocity distribution more precise.

The program was run with the distance of the heat source as $d = 2R$ and the boundary distance as $L = 9R$, and using a temperature distribution calculated using the program described in section 3.4.2. The resulting flow distribution was as shown in figure 3.9.

Figure 3.9: The flow distribution around a heated bubble for a point heat source determined by numerically solving the differential equation. The position of the point heat source is shown by a cross.

The flow distribution shown in figure 3.8 appears to have the circulating pattern similar to that observed experimentally (see figure 3.3 (a)). It was found, however, that if the boundary was moved further out in the numerical solution, the circulating region also moved further out. It therefore appears that the circulation is an artefact of the discretisation due to the finite boundary.

Note that very close to the bubble the shape of the flow is similar to that obtained using Gegenbauer polynomials. A similar simulation was performed to that above for a boundary diameter 20 times the diameter of the bubble, and the streamlines of the resulting distribution

in the region of the bubble are shown in figure 3.10. The streamlines obtained are very similar to those shown in figure 3.8. Using this method to calculate the theoretical convection velocities for the example of the bubble shown in figure 3.3 (b) gives a maximum convection velocity of about 56 mm·s^{-1}, which is fairly close to that obtained using Gegenbauer polynomials.
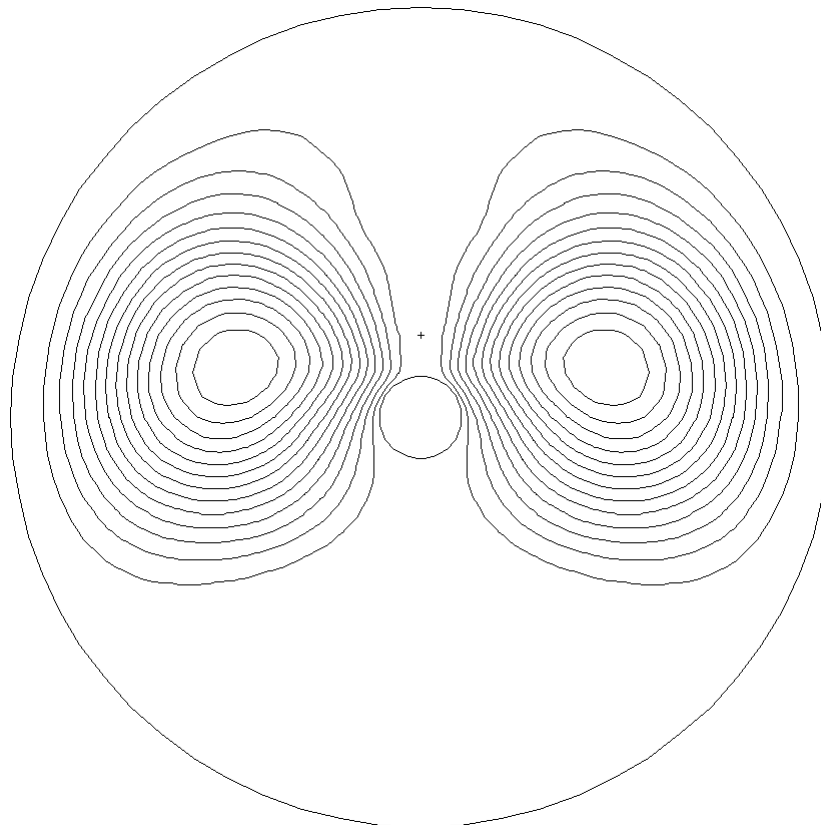

Figure 3.10: The flow distribution around a heated bubble for a point heat source determined by numerically solving the differential equation. The boundary diameter is 20 times the bubble diameter for this simulation. The position of the point heat source is shown by a cross.

Other approximations that have been made are that the variation in the thermal conductivity and thermal coefficient of surface tension with temperature have been ignored. Taking account of these variations with temperature will only alter the coefficients I_n in equation (2.29), however, and will not qualitatively change the flow pattern. The variation of the viscosity with temperature can also taken into account. In the general case the differential equation for the flow velocity is

$$\tfrac{4}{3}\nabla\left(\eta\nabla\cdot\boldsymbol{u}\right)+\nabla\left(\boldsymbol{u}\cdot\nabla\eta\right)-\boldsymbol{u}\nabla^2\eta+\nabla\eta\times\left(\nabla\times\boldsymbol{u}\right)-\left(\nabla\cdot\boldsymbol{u}\right)\nabla\eta-\nabla\times\left(\nabla\times\eta\boldsymbol{u}\right)=\nabla p \qquad (3.35)$$

Expanding this and assuming only the continuity equation $\nabla\cdot\boldsymbol{u}=0$ gives

$$\partial_j\eta\left(\partial_i u_j+\partial_j u_i\right)+\eta\nabla^2 u_i=\partial_i p \qquad (3.36)$$

In spherical polar coordinates the differential equation in terms of the streamfunction is

$$\eta\left(\frac{\partial^2}{\partial r^2}+\frac{1}{r^2}\frac{\partial^2}{\partial\theta^2}-\frac{\cot\theta}{r^2}\frac{\partial}{\partial r}\right)^2\psi+\frac{\partial\eta}{\partial r}\frac{\partial^3\psi}{\partial r^3}+\frac{1}{r^2}\frac{\partial\eta}{\partial\theta}\frac{\partial^3\psi}{\partial r^2\partial\theta}+\frac{1}{r^2}\frac{\partial\eta}{\partial r}\frac{\partial^3\psi}{\partial r\partial\theta^2}+\frac{1}{r^4}\frac{\partial\eta}{\partial\theta}\frac{\partial^3\psi}{\partial\theta^3}$$

$$+\left(\frac{\partial^2\eta}{\partial r^2}-\frac{1}{r^2}\frac{\partial^2\eta}{\partial\theta^2}-\frac{2}{r}\frac{\partial\eta}{\partial r}-\frac{\cot(\theta)}{r^2}\frac{\partial\eta}{\partial\theta}\right)\frac{\partial^2\psi}{\partial r^2}+\left(\frac{4}{r^2}\frac{\partial^2\eta}{\partial r\partial\theta}-\frac{\cot(\theta)}{r^2}\frac{\partial\eta}{\partial r}-\frac{4}{r^3}\frac{\partial\eta}{\partial\theta}\right)\frac{\partial^2\psi}{\partial r\partial\theta}$$

$$+\left(\frac{-1}{r^2}\frac{\partial^2\eta}{\partial r^2}+\frac{1}{r^4}\frac{\partial^2\eta}{\partial\theta^2}-\frac{2}{r^3}\frac{\partial\eta}{\partial r}-\frac{2\cot(\theta)}{r^4}\frac{\partial\eta}{\partial\theta}\right)\frac{\partial^2\psi}{\partial\theta^2}\qquad(3.37)$$

$$+\left(\frac{-2}{r^2}\frac{\partial^2\eta}{\partial r^2}-\frac{2\cot(\theta)}{r^4}\frac{\partial^2\eta}{\partial r\partial\theta}+\frac{2}{r^3}\frac{\partial^2\eta}{\partial\theta^2}+\frac{2}{r^2}\frac{\partial\eta}{\partial r}+\frac{2\cot(\theta)}{r^3}\frac{\partial\eta}{\partial\theta}\right)\frac{\partial\psi}{\partial r}$$

$$+\left(\frac{\cot(\theta)}{r^2}\frac{\partial^2\eta}{\partial r^2}-\frac{6}{r^3}\frac{\partial^2\eta}{\partial r\partial\theta}-\frac{\cot(\theta)}{r^4}\frac{\partial^2\eta}{\partial\theta^2}+\frac{2\cot(\theta)}{r^3}\frac{\partial\eta}{\partial r}+\frac{2+5\sin^2(\theta)}{r^4\sin^2(\theta)}\frac{\partial\eta}{\partial\theta}\right)\frac{\partial\psi}{\partial\theta}=0$$

The program for solving this differential equation (with the same boundary conditions as previously) is given in appendix B.7. This program also takes into account the nonlinear dependence of the surface tension on temperature.

An example simulation is shown in figure 3.11. In this example the power of the heat source is 1 mW, the bubble radius is 1 μm, and the medium is water. As can be seen, the circulation is brought closer to the bubble, however it was found that the circulating pattern still expanded indefinitely as the radius of the simulation was increased.

Note that if any dependences on temperature produced the circulation, then the circulation would only be observed at higher powers, which was not what was found experimentally. Another approximation that has been made is that the inertial terms have been ignored in the Navier-Stokes equation. This factor is also strongly dependent on the power, and at moderate convection velocities the inertial terms are completely negligible.

The remaining approximation that has been made is that the slide has been ignored. The slide changes the geometry of the system significantly, possibly enough to produce the circulation patterns. Also the boundary conditions at the slide are that the flow velocity is zero. This will slow down the flow, and this may be the reason why the flow velocities observed were far less than the velocities predicted from the theory ignoring the slide.

If the slide is included in the calculations, then the rotational symmetry of the problem is broken, and the calculations must be performed in three dimensions. The problem is far more difficult then, as there are far more points in the calculation requiring more memory and longer calculation times. In addition it is not possible to represent the flow by a single streamfunction variable, further increasing the size of the problem, and it is not possible to use
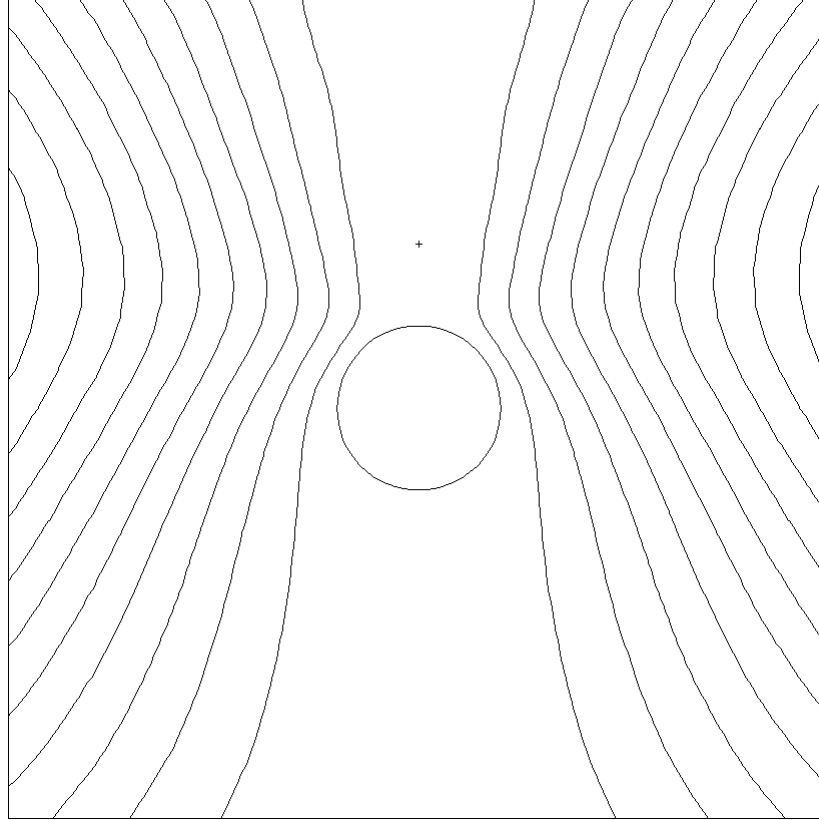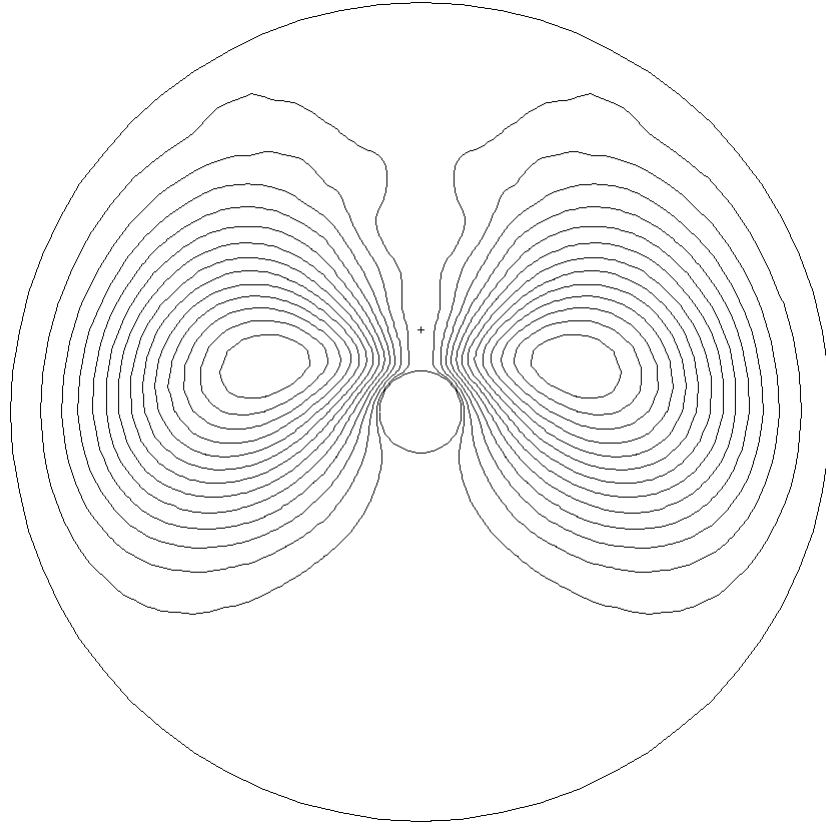
Figure 3.11: The flow distribution around a heated bubble for a point heat source determined by numerically solving the differential equation and taking into account the thermal variation in the viscosity. The position of the point heat source is shown by a cross.

a simple, regular mesh due to the geometry of the problem. In order to overcome these problems simulations were attempted using FIDAP. FIDAP will not automatically mesh regions of this type, however, and although there have been indications that meshing may be possible, the region has not yet been successfully meshed.

3.5 Convection in the Absence of a Bubble

Now the convection in the absence of a bubble will be considered. In this case it is reasonable to make the approximation of convection from a point heat source. There are closed form analytic solutions if we assume that

$$
\frac{\partial^2 u}{\partial z^2} << \frac{1}{r}\frac{\partial}{\partial r}\left(r\frac{\partial u}{\partial r}\right)
$$
$$
\frac{\partial^2 T}{\partial z^2} << \frac{1}{r}\frac{\partial}{\partial r}\left(r\frac{\partial T}{\partial r}\right)
$$

(3.38)

and the Prandtl number is either 1 or 2 [51]. It was found, however, that at the scale of the

problem the analytic solutions give flow that is directly upwards from the slide. In addition the form of the temperature distribution is not close to spherically symmetric in the region of the point heat source. This strongly indicates that the assumption (3.38) is not justified.

Therefore the flow without assuming (3.38) will be considered. It is reasonable to ignore the nonlinear terms in the differential equation for the velocity, as the convection is at very low velocity. The equations for the flow in this approximation are

$$\eta \nabla^2 \boldsymbol{u} = \nabla p + \rho g \hat{\boldsymbol{k}}$$
$$\nabla \cdot \boldsymbol{u} = 0 \tag{3.39}$$

The equation of motion in cylindrical coordinates is

$$\eta \left(\frac{1}{R} \left(\frac{\partial^2}{\partial R^2} + \frac{\partial^2}{\partial z^2} \right)^2 \psi - \frac{2}{R^2} \frac{\partial}{\partial R} \left(\frac{\partial^2 \psi}{\partial R^2} + \frac{\partial^2 \psi}{\partial z^2} \right) + \frac{3}{R^3} \frac{\partial^2 \psi}{\partial R^2} - \frac{3}{R^4} \frac{\partial \psi}{\partial R} \right) = g \frac{\partial \rho}{\partial R} \tag{3.40}$$

where ψ is the streamfunction for cylindrical coordinates such that

$$u_z = \frac{1}{R} \frac{\partial \psi}{\partial R}$$
$$u_R = -\frac{1}{R} \frac{\partial \psi}{\partial z} \tag{3.41}$$

Now the water can be assumed to be incompressible, so the pressure has a negligible effect on the density. The density is therefore only dependent on the temperature. The flow will have very little effect on the temperature distribution, so the temperature distribution can be taken to be

$$T = \frac{P}{2\pi \left(h_l + h_g \right) \left(R^2 + z^2 \right)^{1/2}} + T_0 \tag{3.42}$$

The term on the right of equation (3.40) then becomes

$$g \frac{\partial \rho}{\partial R} = g \frac{\partial \rho}{\partial T} \frac{\partial T}{\partial R}$$
$$= -g \frac{\partial \rho}{\partial T} \frac{P}{2\pi \left(h_l + h_g \right)} \frac{R}{\left(R^2 + z^2 \right)^{3/2}} \tag{3.43}$$

Therefore the equation of motion is

$$R^3 \left(\frac{\partial^2}{\partial R^2} + \frac{\partial^2}{\partial z^2} \right)^2 \psi - 2R^2 \frac{\partial}{\partial R} \left(\frac{\partial^2 \psi}{\partial R^2} + \frac{\partial^2 \psi}{\partial z^2} \right) + 3R \frac{\partial^2 \psi}{\partial R^2} - 3 \frac{\partial \psi}{\partial R} = -\frac{\partial \rho}{\partial T} \frac{gP}{2\pi \eta \left(h_l + h_g \right)} \frac{R^5}{\left(R^2 + z^2 \right)^{3/2}} \tag{3.44}$$

The boundary conditions are

$$\psi\big|_{R=0,\infty} = 0 \tag{3.45a}$$

$$\psi\big|_{z=0,\infty} = 0 \tag{3.45b}$$

$$\frac{\partial \psi}{\partial R}\bigg|_{R=0,\infty} = 0 \tag{3.45c}$$

$$\frac{\partial \psi}{\partial z}\bigg|_{z=0,\infty} = 0 \tag{3.45d}$$

The complete program for solving the system is given in appendix B.8. An example of a calculated streamfunction is shown in figure 3.12.

Figure 3.12: The convection pattern around a point heat source determined by numerically solving the differential equation. The boundary radius is 64 μm for this simulation.

When the power is 1 mW and the liquid is water, the maximum velocity calculated is about 0.97 μm·s^{-1}, however the maximum inward velocity (which is all that can be observed from above) is only about 0.15 μm·s^{-1}. These figures are in agreement with the observations that in pure water the velocities were detectable, but below about 1 μm·s^{-1}. This velocity is perhaps a little higher than might be expected, however, as the motion was virtually undetectable in pure

water. In water with detergent added the viscosity is decreased, which increases the convection velocity. Since the viscosity is not known, however, it is not possible to make more quantitative comparisons.

It is also possible to take account of the variation of viscosity with temperature. The general formula in the case of variable viscosity is given in equation (3.36). Converting this equation into cylindrical coordinates gives

$$
\begin{aligned}
&\eta\left[R^3\left(\frac{\partial^2}{\partial R^2}+\frac{\partial^2}{\partial z^2}\right)^2\psi - 2R^2\frac{\partial}{\partial R}\left(\frac{\partial^2\psi}{\partial R^2}+\frac{\partial^2\psi}{\partial z^2}\right) + 3R\frac{\partial^2\psi}{\partial R^2} - 3\frac{\partial^2\psi}{\partial R^2}\right] + \frac{1}{R}\frac{\partial\eta}{\partial R}\frac{\partial^3\psi}{\partial R^3} \\[2mm]
&+\frac{1}{R}\frac{\partial\eta}{\partial z}\frac{\partial^3\psi}{\partial R^2\partial z}+\frac{1}{R}\frac{\partial\eta}{\partial R}\frac{\partial^3\psi}{\partial R\partial z^2}+\frac{1}{R}\frac{\partial\eta}{\partial z}\frac{\partial^3\psi}{\partial z^3}+\left[-\frac{2}{R^2}\frac{\partial\eta}{\partial R}+\frac{1}{R}\left(\frac{\partial^2\eta}{\partial R^2}-\frac{\partial^2\eta}{\partial z^2}\right)\right]\frac{\partial^2\psi}{\partial R^2} \\[2mm]
&+\left[-\frac{1}{R}\frac{\partial\eta}{\partial z}+\frac{4}{R}\frac{\partial^2\eta}{\partial R\partial z}\right]\frac{\partial^2\psi}{\partial R\partial z}+\left[-\frac{1}{R^2}\frac{\partial\eta}{\partial R}+\frac{1}{R}\left(\frac{\partial^2\eta}{\partial z^2}-\frac{\partial^2\eta}{\partial R^2}\right)\right]\frac{\partial^2\psi}{\partial z^2} \\[2mm]
&+\left[\frac{2}{R^3}\frac{\partial\eta}{\partial R}+\frac{1}{R^2}\left(\frac{\partial^2\eta}{\partial z^2}-\frac{\partial^2\eta}{\partial R^2}\right)\right]\frac{\partial\psi}{\partial R}-\frac{2}{R^2}\frac{\partial^2\eta}{\partial R\partial z}\frac{\partial\psi}{\partial z}=-\frac{\partial\rho}{\partial T}\frac{gP}{2\pi\eta\left(h_l+h_g\right)}\frac{R^5}{\left(R^2+z^2\right)^{3/2}}
\end{aligned}
\tag{3.46}
$$

The program that solves this equation is given in appendix B.9, and an example simulation is shown in figure 3.13. The maximum velocity in this case is about 0.34 $\mu\text{m}\cdot\text{s}^{-1}$, and the maximum inward velocity is only about 0.05 $\mu\text{m}\cdot\text{s}^{-1}$. These are significantly less than the velocities obtained when the variation of viscosity with temperature was ignored. These figures are perhaps a little more realistic considering how difficult the effect was to observe in pure water.

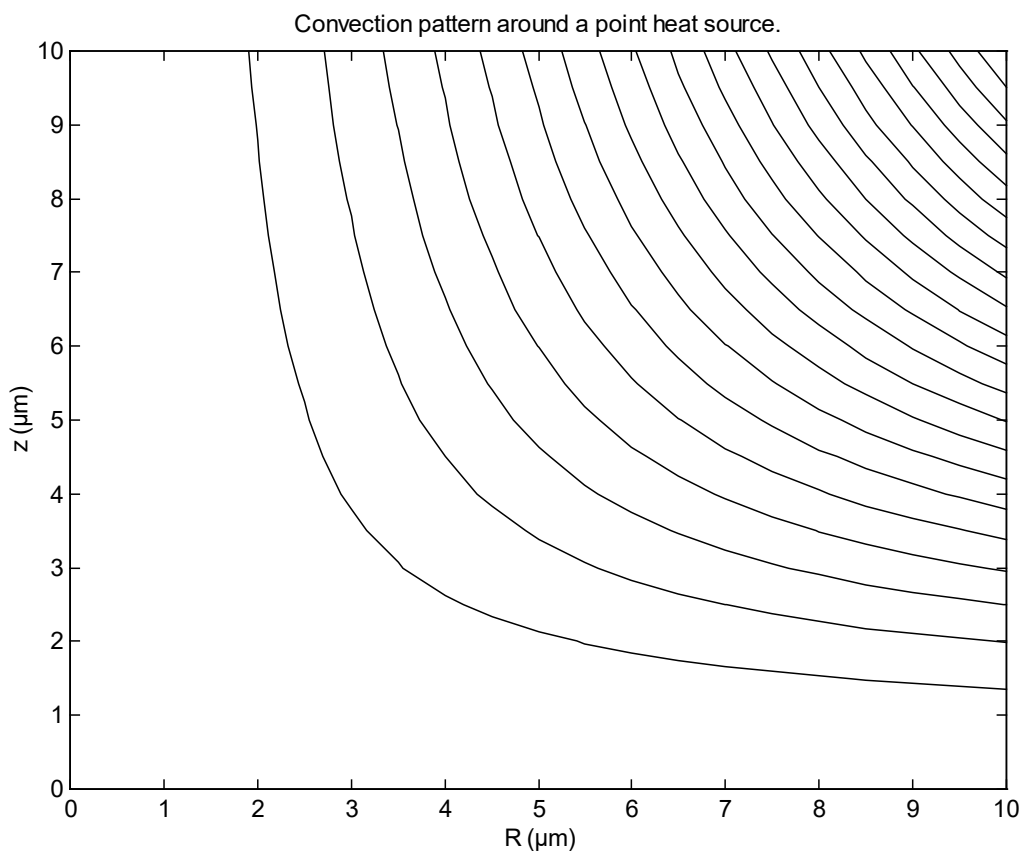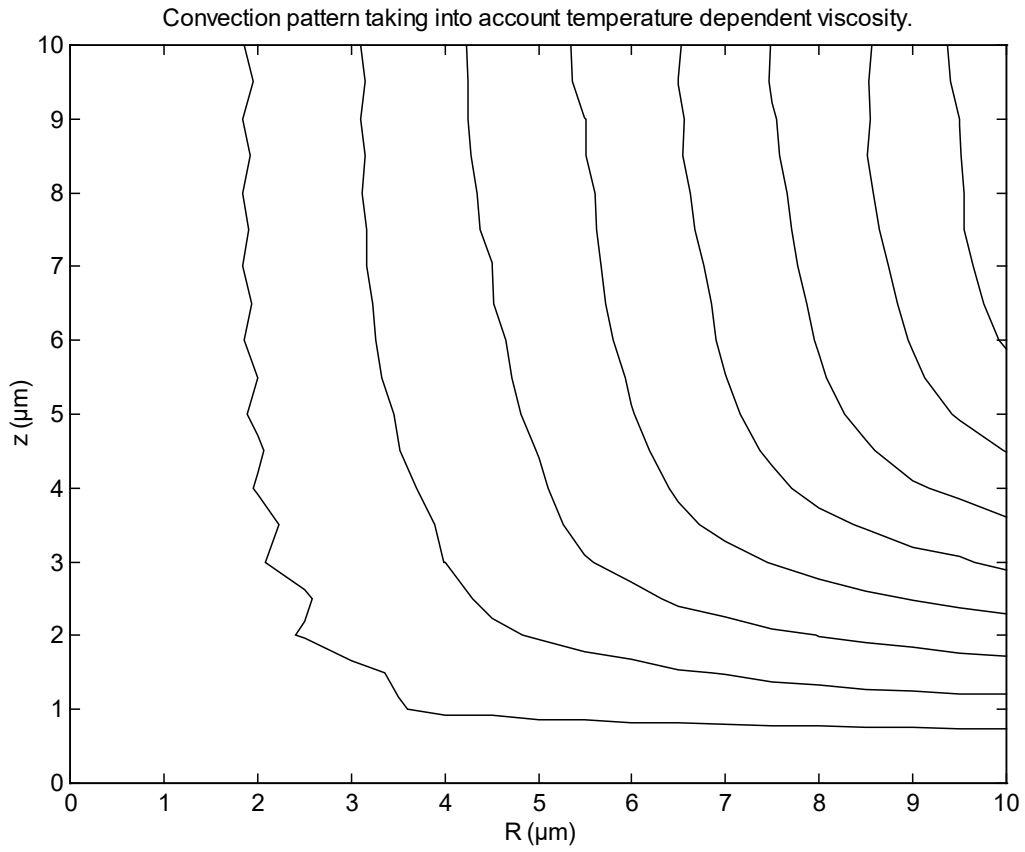**Figure 3.13:** The convection pattern around a point heat source determined by numerically solving the differential equation and assuming a temperature dependent viscosity. The boundary radius is 64 µm for this simulation and the power is 1 mW.

Chapter 4: Conclusion

The results of the experiments with melting toner conclusively show that bubble formation occurs above the boiling point in each of the liquids tested. In methanol and ethanol, the temperatures required for bubble formation were close to the homogeneous nucleation temperatures, as given by equation (2.10) or by the tables in [19]. The temperature obtained in hexafluorobenzene was slightly lower than the homogeneous nucleation temperature, however not more than can be accounted for by heterogeneous nucleation at the interface. The temperature obtained in water was much lower than the homogeneous nucleation temperature. This appears to be due to nucleation within the interior of the toner particles, and the calculated temperature in the interior of the toner particles was fairly close to the homogeneous nucleation temperature.

This is a potential method of measuring the homogeneous nucleation temperatures of liquids. The very small region heated means that there is no problem with pre-existing nuclei, and also that the nucleation rate per unit volume must be very high before nucleation occurs. The main drawback is the uncertainty in the temperature at melting. This problem can be overcome by using a micron-size thermocouple.

In the case of heating toner in water, bubbles of water vapour form in the interior of the toner particles by diffusion; an effect that is normally very difficult to observe. When heating toner particles in methanol it is possible to produce bubbles in the interior of the toner, which is unusual because the surface tension of methanol is less than the combined surface tension of the toner and the interfacial tension. This is only possible due to the high temperature gradient.

The temperature rises predicted from the thermal conductivities of the media and the input power were of the same order of magnitude as the temperature rises observed experimentally. The theoretical temperature rises were fairly uniformly about 3 times greater, however, due to reflection of light off the toner.

The results of using the Curie points of ferrite powders were inconclusive. When focussing the beam on individual particles the reflection of the beam off the particles prevented

sufficient heating taking place. When focussing the beam on strings of particles the effects of heating and the effects of the beam momentum were indistinguishable.

The convection currents seen in the presence of bubbles have been qualitatively explained, and the convection currents are in the direction expected. It was found that the carbon black pigment contained in the toner particles provided a very useful means for visualising the convection patterns around the bubbles. Circulating convection patterns were seen in virtually all configurations. This has not yet been reproduced theoretically. This is probably due to the effect of the slide, which could not be taken into account in the simulations. The predicted flow velocities were of a similar order of magnitude to those observed, but were much faster. This is probably also due to the effect of the slide.

The attraction of bubbles to the focus of the beam has also been qualitatively explained as due to Marangoni convection. This provides a means of trapping bubbles, which cannot normally be trapped due to their low refractive index. The terminal bubble migration velocities calculated were on the order of a metre per second, which is more than enough to account for the high bubble velocities observed. This corresponds to a strength of the thermal trap on the order of 10^4 times greater than the strength of optical bubble trapping. In experiments estimating the strength of the thermal trap by the speed a trapped bubble can be moved, the only observed limit to the bubble speed appeared to be due to irregularities in the paint on the slide.

Lastly the theoretical convection velocities in the absence of a bubble have also been calculated by numerical simulations both ignoring and taking account of the thermal variation in viscosity. Though the very low thermal convection velocities in pure water prevented accurate numerical measurements, the observed convection velocities were of the same order of magnitude as those calculated.

Appendix A: Raw Data

Table A.1: Reflectance measurements for IF550 filter.

Measurement	Input (mW)	Output (mW)	Reflectance
1	0.757	0.731	0.9657
2	0.768	0.741	0.9648
3	0.733	0.700	0.9550
4	0.759	0.724	0.9539
5	0.748	0.714	0.9545
6	0.764	0.731	0.9568
7	0.793	0.754	0.9508
8	0.764	0.725	0.9490
9	0.789	0.760	0.9632
10	0.811	0.771	0.9507
11	0.793	0.751	0.9470
12	0.785	0.744	0.9478
13	0.773	0.733	0.9483
14	0.775	0.730	0.9419
15	0.793	0.759	0.9571
16	0.816	0.779	0.9547
17	0.770	0.730	0.9481
18	0.789	0.744	0.9430
19	0.830	0.793	0.9554
20	0.762	0.736	0.9659
21	0.755	0.720	0.9536
22	0.757	0.720	0.9511
23	0.780	0.749	0.9603
24	0.782	0.753	0.9629

Table A.2: Transmittance measurements for total system.

Measurement	Input (mW)	Output (mW)	Transmittance
1	0.491	0.332	0.6762
2	0.466	0.317	0.6803
3	0.478	0.323	0.6757
4	0.475	0.324	0.6821
5	0.505	0.340	0.6733
6	0.515	0.348	0.6757
7	0.480	0.321	0.6688
8	0.476	0.323	0.6786
9	0.475	0.321	0.6758
10	0.472	0.323	0.6843
11	0.480	0.325	0.6771
12	0.488	0.328	0.6721
13	0.477	0.322	0.6751
14	0.469	0.321	0.6844
15	0.474	0.323	0.6814
16	0.476	0.328	0.6891

Table A.3: Calibration measurements for Scientech power meter.

Head	Measurement	Current (mA)	Voltage (V)	Power (mW)*
1	1	17.63	0.723	25.25
	2	17.60	0.722	25.5
2	1	15.85	0.657	9.1
	2	15.84	0.657	9.1
3	1	17.49	0.714	24
	2	17.48	0.715	23.75

* The powers were measured to the nearest quarter milliwatt for heads 1 and 3.

Table A.4: Calibration measurements for Spectramet power meter.

Head	Measurement	Spectramet (mW)	Scientech (mW)*
1	1	13.94	22.5
	2	14.65	23.5
2	1	13.41	9.1
	2	13.72	9.4
3	1	14.29	21.5
	2	15.01	22.5

* The powers were measured to the nearest quarter milliwatt for heads 1 and 3.

Appendix B: Programs

B.1 TempDist

function [T, Tc]=TempDist(I,J,L,hp,hg,hw,kappa,P,omega,rp,n,opt);
% Calculates the temperature distribution around a hemispherical, semitransparent toner particle being
% heated by an n'th order Gauss-Laguerre beam, up to a distance of L*, by solving Laplace's equation with*
% initial conditions imposed on the derivative at the surface of the bubble. The temperature is taken to be 0 at
% infinity.
% [T Tc] = TempDist(I,J,L,hp,hg,hw,kappa,P,omega,rp,n,opt); returns the temperature distribution T *and the*
% temperature at the centre Tc*. I is the number of intervals in the* r *direction,* J *is the number of intervals in*
% the theta *direction,* L *is the distance the outer wall is away,* hp*,* hg *and* hw *are the thermal conductivities of*
% the particle, glass and water respectively, kappa *is the opacity,* P *is the laser power,* omega *is the beam*
% width, rp *is the radius of the particle,* n *is the order of the beam and* opt *is 1 if a progress indicator is*
% required.

% Check if opt *had been passed as an argument, and set it to 0 if it has not.*
if nargin<12,
  opt=0;
end

% Normalise variables to units where rp*=1.*
L=L/rp;
kappa=kappa*rp;
omega=omega/rp;

% Initialise the various variables required for the program.
Ip=I+1;
Jp=J+1;
dr=L/I;
dth=pi/J;
thj=dth*(0:J);
sth=sin(thj);
cth=cos(thj);
sthm=sin(thj-dth/2);
ri=dr*(1:I);
rim=ri-dr/2;
dr2=dr*dr;
dth2=dth*dth;
rim2=rim.*rim;

% Initialise matrices for solving distribution.
s=sparse(I*Jp+1,I*Jp+1);
an=zeros(I*Jp+1,1);

disp('Constructing s matrix...');
l=1;
% Boundary condition at r*=0 (2.31a).*
s(l,I*Jp+1)=-1.5;
s(l,J/2+1)=2;
s(l,Jp+J/2+1)=-0.5;

73

```
l=l+1;

% Initialise variables for speeding up differential equation construction.
tmp1=rim2(2:I)/dr2;
tmp2=rim2(1:I-1)/dr2;
tmp3=sthm(1:J)./(sth(1:J)*dth2);
tmp4=sthm(2:Jp)./(sth(1:J)*dth2);
tmp5=-(tmp3+tmp4);
tmp6=-(tmp1+tmp2);
im=round(1/dr)-1;

% Construct s matrix for r<1.
for i=1:im,
  iJp=(i-1)*Jp;
  % Boundary condition at theta=0 (2.31b).
  s(l,iJp+1)=1.5;
  s(l,iJp+2)=-2;
  s(l,iJp+3)=0.5;
  l=l+1;
  % Differential equation inside particle (2.30).
  for j=2:J/2,
    s(l,iJp+Jp+j)=tmp1(i);
    if i==1,
      s(l,Jp+J/2+1)=tmp2(i);
    else
      s(l,iJp-Jp+j)=tmp2(i);
    end
    s(l,iJp+j-1)=tmp3(j);
    s(l,iJp+j+1)=tmp4(j);
    s(l,iJp+j)=tmp5(j)+tmp6(i);
    rs=ri(i)*sth(j);
    % Heating due to beam.
    an(l)=-ri(i)*ri(i)*rs^(2*n)*exp(-2*(rs/omega)^2-kappa*(sqrt(1-rs*rs)-ri(i)*cth(j)));
    l=l+1;
  end
  % Boundary condition at theta=pi/2 (2.31e).
  s(l,iJp+J/2-1)=hp*0.5;
  s(l,iJp+J/2)=-hp*2;
  s(l,iJp+J/2+1)=(hp+hg)*1.5;
  s(l,iJp+J/2+2)=-hg*2;
  s(l,iJp+J/2+3)=hg*0.5;
  l=l+1;
  % Differential equation in slide (2.25).
  for j=J/2+2:J,
    s(l,iJp+Jp+j)=tmp1(i);
    if i==1,
      s(l,Jp+J/2+1)=tmp2(i);
    else
      s(l,iJp-Jp+j)=tmp2(i);
    end
    s(l,iJp+j-1)=tmp3(j);
    s(l,iJp+j+1)=tmp4(j);
    s(l,iJp+j)=tmp5(j)+tmp6(i);
    l=l+1;
  end
  % Boundary condition at theta=pi (2.31c).
  s(l,iJp+Jp)=1.5;
  s(l,iJp+J)=-2;
  s(l,iJp+J-1)=0.5;
```

```
  l=l+1;
  if opt,
    home
    disp(i);
  end
end


% Boundary condition at r=rp, theta=0 (2.31b).
iJp=im*Jp;
s(l,iJp+1)=1.5;
s(l,iJp+2)=-2;
s(l,iJp+3)=0.5;
l=l+1;

% Boundary condition at r=rp (2.31f).
for j=2:J/2+1,
  s(l,(im-2)*Jp+j)=hp*0.5;
  s(l,(im-1)*Jp+j)=-hp*2;
  s(l,im*Jp+j)=(hp+hw)*1.5;
  s(l,(im+1)*Jp+j)=-hw*2;
  s(l,(im+2)*Jp+j)=hw*0.5;
  l=l+1;
end

% Differential equation within glass (2.25).
for j=J/2+2:J,
  s(l,iJp+Jp+j)=tmp1(i);
  s(l,iJp-Jp+j)=tmp2(i);
  s(l,iJp+j-1)=tmp3(j);
  s(l,iJp+j+1)=tmp4(j);
  s(l,iJp+j)=tmp5(j)+tmp6(i);
  l=l+1;
end

% Boundary condition at r=rp, theta=pi (2.31c).
s(l,iJp+Jp)=1.5;
s(l,iJp+J)=-2;
s(l,iJp+J-1)=0.5;
l=l+1;

% Construct s matrix for r>rp.
for i=im+2:I-1,
  iJp=(i-1)*Jp;
  % Boundary condition at theta=0 (2.31d).
  s(l,iJp+1)=1.5;
  s(l,iJp+2)=-2;
  s(l,iJp+3)=0.5;
  l=l+1;
  % Differential equation inside water (2.25).
  for j=2:J/2,
    s(l,iJp+Jp+j)=tmp1(i);
    s(l,iJp-Jp+j)=tmp2(i);
    s(l,iJp+j-1)=tmp3(j);
    s(l,iJp+j+1)=tmp4(j);
    s(l,iJp+j)=tmp5(j)+tmp6(i);
    rs=ri(i)*sth(j);
    l=l+1;
  end
  % Boundary condition at theta=pi/2 (2.31g).
```

75

```
   s(l,iJp+J/2-1)=hw*0.5;
   s(l,iJp+J/2)=-hw*2;
   s(l,iJp+J/2+1)=(hw+hg)*1.5;
   s(l,iJp+J/2+2)=-hg*2;
   s(l,iJp+J/2+3)=hg*0.5;
   l=l+1;
   % Differential equation inside slide (2.25).
   for j=J/2+2:J,
     s(l,iJp+Jp+j)=tmp1(i);
     s(l,iJp-Jp+j)=tmp2(i);
     s(l,iJp+j-1)=tmp3(j);
     s(l,iJp+j+1)=tmp4(j);
     s(l,iJp+j)=tmp5(j)+tmp6(i);
     l=l+1;
   end
   % Boundary condition at theta=pi (2.31c).
   s(l,iJp+Jp)=1.5;
   s(l,iJp+J)=-2;
   s(l,iJp+J-1)=0.5;
   l=l+1;
   if opt,
     home
     disp(i);
   end
end

% Boundary condition at r=inf (2.31h, 2.31i).
for j=1:Jp,
  s(l,(I-1)*Jp+j)=1;
  l=l+1;
end

% Multiply an by various scaling constants.
an=an*(2*kappa*P)/(pi*hp*omega^2*rp);
an=an*(2^n/(gamma(n+1)*omega^(2*n)));

% Solve system.
disp('Solving...');
Tvec=s\an;

% Correct the temperature distribution for the temperature at the edges.
rat=1-ratio(kappa,omega,1,n,eps);
Tvec=Tvec+rat*P/(2*pi*L*rp*(hw+hg));
T=[];
for i=0:I-1,
  T=[T Tvec((i*Jp+1):((i+1)*Jp))];
end
T=T';
Tc=Tvec(I*Jp+1);
*******************************************************************************
```

Functions used by TempDist.m

```
function ra=ratio(kappa,omega,rp,n,er);
% Determines the ratio of the power of a Gauss-Laguerre beam of order n and width omega transmitted
% through a hemispherical particle of radius rp and opacity kappa to accuracy er.
rp=rp/omega;
kappa=kappa*omega;
ra=0;
for m=0:n,
```

```
  ra=ra+(2*rp*rp)^(n-m)/gamma(n-m+1);
end
ra=ra*exp(-2*rp*rp);
ra=ra+2^(n+2)/gamma(n+1)*quad8('intensit',0,rp,er,0,kappa,rp,n);
```

B.2 HomDisNu

```
function Ja=HomDisNu(T,L,rp);
```
% Calculates the homogeneous nucleation rate around a particle given the temperature distribution.
% Ja = HomDisNu(T,L,rp); returns the nucleation rate Ja. T is the temperature distribution, L is the
% distance the outer wall is away and rp *is the radius of the particle.*

% Calculate various variables required.
```
[I J]=size(T);
J=J-1;
dr=L/I;
im=round(rp/dr);
dth=pi/J;
Jh=round(J/2);
```
% Now interpolate intermediate values for the new mesh.
```
T1=T(im:im+1,1:Jh);
T=[];
for i=0:100,
  for j=1:Jh,
    T(i+1,j*2-1)=T1(2,j)*i/100+T1(1,j)*(1-i/100);
  end
  T(i+1,2)=T(i+1,1)*9/16+T(i+1,3)/2-T(i+1,5)/16;
  for j=2:Jh-1,
    T(i+1,j*2)=(T(i+1,j*2-1)+T(i+1,j*2+1))/2;
  end
end
```
% Now rescale the variables.
```
Jh=Jh*2-1;
L=dr;
dr=dr/100;
dth=dth/2;
```
% Now calculate the various quantities required for integration.
```
thh=dth*(0:Jh)+dth/2;
cth=cos(thh);
```
% Calculate nucleation rate for each point on grid.
```
J1=homnucl(T(1:101,1:Jh));
```
% Add nucleation rate at surface.
```
da=dr*pi*(rp+dr/4)^2;
Ja=J1(1,1)*(1-cth(1));
for j=2:Jh,
  Ja=Ja+J1(1,j)*(cth(j-1)-cth(j));
end
Ja=da*Ja;
```
% Add nucleation rate in bulk.
```
for i=2:101,
  dJa=J1(i,1)*(1-cth(1));
  for j=2:Jh,
    dJa=dJa+J1(i,j)*(cth(j-1)-cth(j));
  end
  Ja=Ja+dJa*dr*pi*(rp+i*dr)^2;
end
```
****

Functions used by HomDisNu.m

```
function J=homnucl(T);
% Calculates the homogeneous nucleation rate per unit volume for water at temperature T.
T1=T+273.15;
m=2.99151962867e-26;
k=1.380658E-23;
PL=101325;
N0=density(T)/m;
delta=0.5*N0.^(-1/3);
Pn=pressure(T).*exp((PL-pressure(T))./(k*N0.*T));
s=tension(T);
s1=s+delta.*(Pn-PL);
b=(Pn-PL)./Pn;
J=N0.*sqrt(6*s1./(pi*m*(3-b))).*exp(-(heat(T)+(16*pi*s1.^3)./(3*(Pn-PL).^2))./(k*T1));

function d=density(T);
% Gives the density of water at temperature T.
d=(999.83952+16.945176*T-7.9870401E-3*T.^2-46.170461E-6*T.^3+105.56302E-9*T.^4
                                                -280.54253E-12*T.^5)./(1+16.879850E-3*T);

function p=pressure(T);
% Gives the vapour pressure of water at temperature T.
T=T+273.15;
Tc=647.126;
pc=22064000;
tau=1-T/Tc;
a=[-7.85823 1.83991 -11.7811 22.6705 -15.9393 1.77516];
p=pc*exp(Tc*(a(1)*tau+a(2)*tau.^1.5+a(3)*tau.^3+a(4)*tau.^3.5+a(5).*tau.^4+a(6)*tau.^7.5)./T);

function s=tension(T);
% Gives the surface tension of water at temperature T.
T=T+273.15;
X=(647.126-T)/647.126;
s=0.2358*X.^1.256.*(1-.625*X);

function h=heat(T);
% Gives the molecular heat of vaporisation of water at temperature T.
T=T+273.15;
Tc=647.126;
X=(Tc-T)/Tc;
h=44.457979*X.^0.375+14.635863*X.^1.375-27.945633*X.^2.375+13.985176*X.^3.375;
h=h/6.0221367E20;
```

B.3 HetDisNu

```
function Ja=HetDisNu(T,L,rp,phi);
% Calculates the heterogeneous nucleation rate around a particle given the temperature distribution.
% Ja = HetDisNu(T,L,rp,phi);  returns the nucleation rate Ja.  T is the temperature distribution, L is the
% distance the outer wall is away, rp is the radius of the particle and phi is the contact angle.

% Calculate various variables required.
[I J]=size(T);
J=J-1;
dr=L/I;
im=round(rp/dr);
dth=pi/J;
```

```
Jh=round(J/2);
% Now interpolate intermediate values for the new mesh.
T1=T(im,1:Jh);
T=[];
for j=1:Jh,
  T(j*2-1)=T1(j);
end
T(2)=T(1)*9/16+T(3)/2-T(5)/16;
for j=2:Jh-1,
  T(j*2)=(T(j*2-1)+T(j*2+1))/2;
end
% Now rescale the variables.
Jh=Jh*2-1;
L=dr;
dth=dth/2;
% Now calculate the various quantities required for integration.
thh=dth*(0:J)+dth/2;
cth=cos(thh);
J1=hetnucl(T,phi);
% Calculate nucleation rate.
da=2*pi*rp^2;
Ja=J1(1)*(1-cth(1));
for j=2:Jh,
  Ja=Ja+J1(j)*(cth(j-1)-cth(j));
end
Ja=Ja*da;
```
****

Functions used by HetDisNu.m

```
function J=hetnucl(T,phi)
% Calculates the heterogeneous nucleation rate per unit area at a solid-liquid interface at temperature T for
% wetting angle phi.
T1=T+273.15;
m=2.99151962867e-26;
k=1.380658E-23;
PL=101325;
N0=density(T)/m;
delta=0.5*N0.^(-1/3);
Pn=pressure(T).*exp((PL-pressure(T))./(k*N0.*T));
s=tension(T);
s1=s+delta.*(Pn-PL);
b=(Pn-PL)./Pn;
phi=phi*pi/180;
psi=0.5*(1+cos(phi));
omega=psi*psi*(2-cos(phi));
J=psi*N0.^(2/3).*sqrt(6*s1./(pi*m*(3-b)*omega))
                                     .*exp(-(heat(T)+(16*pi*omega*s1.^3)./(3*(Pn-PL).^2))./(k*T1));
```

B.4 LiqDisNu

```
function Ja=LiqDisNu(T,L,rp,sig1,sig2,sig12);
% Calculates the heterogeneous nucleation rate around a liquefied particle given the temperature distribution.
% Ja = LiqDisNu(T,L,rp,sig1,sig2,sig12);  returns the nucleation rate Ja.  T is the temperature distribution, L %
is the distance the outer wall is away, rp is the radius of the particle and sig1, sig2 and sig12 are surface
% tensions of the particle, the water and the interfacial tension.
```

```
% Calculate various variables required.
[I J]=size(T);
J=J-1;
dr=L/I;
im=round(rp/dr);
dth=pi/J;
Jh=round(J/10);
% Now interpolate intermediate values for the new mesh.
T1=T(im,1:Jh);
T=[];
for j=1:Jh,
  T(j*2-1)=T1(j);
end
T(2)=T(1)*9/16+T(3)/2-T(5)/16;
for j=2:Jh-1,
  T(j*2)=(T(j*2-1)+T(j*2+1))/2;
end
% Now rescale the variables.
Jh=Jh*2-1;
L=dr;
dth=dth/2;
% Now calculate the various quantities required for integration.
thh=dth*(0:J)+dth/2;
cth=cos(thh);
J1=liqnucl(T,sig1,sig2,sig12);
% Calculate nucleation rate.
da=2*pi*rp^2;
Ja=J1(1,1)*(1-cth(1));
for j=2:Jh,
  Ja=Ja+J1(1,j)*(cth(j-1)-cth(j));
end
Ja=Ja+J1(1,Jh)*cth(J/2);
Ja=da*Ja;
**************************************************************************************
```

Functions used by LiqDisNu.m


```
function J=hetnucl(T,sig1,sig2,sig12)
% Calculates the heterogeneous nucleation rate per unit area at a liquid-liquid surface at temperature T
% between liquids with surface tensions sig1 and sig2 and interfacial tension sig12.
T1=T+273.15;
m=2.99151962867e-26;
k=1.380658E-23;
PL=101325;
N0=density(T)/m;
delta=0.5*N0.^(-1/3);
Pn=pressure(T).*exp((PL-pressure(T))./(k*N0.*T));
s=tension(T);
s1=s+delta.*(Pn-PL);
b=(Pn-PL)./Pn;
m1=(sig1^2-sig2^2+sig12^2)/(2*sig1*sig12);
m2=(sig2^2-sig1^2+sig12^2)/(2*sig2*sig12);
psi=0.5*(1-m1);
omega=((2-3*m1+m1^3)*sig1^3+(2-3*m2+m2^3)*sig2^3)/(4*sig1^3);
J=psi*N0.^(2/3).*sqrt(6*s1./(pi*m*(3-b)*omega))
                                        .*exp(-(heat(T)+(16*pi*omega*s1.^3)./(3*(Pn-PL).^2))./(k*T1));
```

B.5 Temp

```
function T=Temp(I,J,L,d,R,hw,P,opt);
% Calculates the temperature distribution around a bubble up to a distance of L with a point heat source at a
% distance d by solving Laplace's equation for the correction to the temperature distribution and adding this
% to the analytic solution in the absence of the bubble.
% T = Temp(I,J,L,d,R,hw,P,opt);  returns the temperature distribution T.  I is the number of intervals in the r
% direction, J is the number of intervals in the theta direction, L is the distance the outer wall is away, d is the
% distance the heat source is away, R is the radius of the bubble, hw is the thermal conductivity of the water, P
% is the power, and opt is 1 if a progress indicator is required.

% Check if opt had been passed as an argument, and set it to 0 if it has not.
if nargin<8,
  opt=0;
end

% Normalise variables to units where R=1.
L=L/R;
d=d/R;

% Initialise the various variables required for the program.
Ip=I+1;
Jp=J+1;
dr=L/I;
dth=pi/J;
thj=dth*(0:J);
sth=sin(thj);
cth=cos(thj);
sthm=sin(thj-dth/2);
ri=1+dr*(0:I);
rim=ri-dr/2;
dr2=dr*dr;
dth2=dth*dth;
rim2=rim.*rim;

% Initialise matrices for solving distribution.
s=sparse(Ip*Jp,Ip*Jp);
an=zeros(Ip*Jp,1);

disp('Constructing s matrix...');
l=1;
% Boundary condition at r=R, theta=0 (3.21c).
s(l,1)=-1.5;
s(l,2)=2;
s(l,3)=-0.5;
l=l+1;

% Derivative boundary condition at r=R (3.21a).
for j=2:J,
  s(l,j)=-1.5;
  s(l,Jp+j)=2;
  s(l,2*Jp+j)=-0.5;
  l=l+1;
end
an(2:J)=dr*(1-d*cth(2:J)).*(d^2+1-2*d*cth(2:J)).^(-1.5);

% Boundary condition at r=R, theta=pi (3.21d).
s(l,Jp)=-1.5;
```

```
s(l,J)=2;
s(l,J-1)=-0.5;
l=l+1;

% Initialise variables for speeding up differential equation construction.
tmp1=rim2(2:I)/dr2;
tmp2=rim2(1:I-1)/dr2;
tmp3=sthm(1:J)./(sth(1:J)*dth2);
tmp4=sthm(2:Jp)./(sth(1:J)*dth2);
tmp5=-(tmp3+tmp4);
tmp6=-(tmp1+tmp2);

% Construct s matrix in bulk.
for i=2:I,
  iJp=(i-1)*Jp;
  % Boundary condition at theta=0 (3.21c).
  s(l,iJp+1)=0.75;
  s(l,iJp+2)=-1;
  s(l,iJp+3)=0.25;
  l=l+1;
  % Differential equation in water (3.17).
  for j=2:J,
    s(l,iJp+Jp+j)=tmp1(i-1);
    s(l,iJp-Jp+j)=tmp2(i-1);
    s(l,iJp+j-1)=tmp3(j);
    s(l,iJp+j+1)=tmp4(j);
    s(l,iJp+j)=tmp5(j)+tmp6(i-1);
    l=l+1;
  end
  % Boundary condition at theta=pi (3.21d).
  s(l,iJp+Jp)=0.75;
  s(l,iJp+J)=-1;
  s(l,iJp+J-1)=0.25;
  l=l+1;
  if opt,
    home
    disp(i);
  end
end

% Boundary condition at r=inf (3.21b).
for j=1:Jp,
  s(l,I*Jp+j)=1;
  l=l+1;
end

% Solve for distribution.
disp('Solving...');
Tvec=s\an;
% Construct T matrix out of vector for T.
T=[];
for i=0:I,
  T=[T Tvec((i*Jp+1):((i+1)*Jp))];
end
% Add on analytic part of solution.
vec1=ones(1,Jp);
T=T'+(d*d+(ri.*ri)'*vec1-2*d*ri'*cth).^(-0.5);
% Scale T.
T=T*P/(4*pi*hw*R);
```

B.6 Stream

```
function p=Stream(L,d,R,hw,P,T,gd,visc,opt);
% Calculates the streamfunction given the temperature distribution on the surface of the bubble and the
% thermal coefficient of surface tension.
% p = Stream(L,d,R,hw,P,T,gd,visc,opt);  returns the streamfunction p.  L is the distance the outer wall is
% away, d is the distance the heat source is away, R is the radius of the bubble hw is the thermal conductivity
% of the water, P is the power, T is the temperature distribution, gd is the thermal coefficient of surface
% tension, visc is the viscosity, and opt is 1 if a progress indicator is required.

% Check if opt had been passed as an argument, and set it to 0 if it has not.
if nargin<9,
  opt=0;
end

% Normalise variables to units where R=1.
L=L/R;
d=d/R;

% Determine J from size of T.
[Ip Jp]=size(T);
I=Ip-1;
J=Jp-1;

% Change T to get unscaled correction.
dr=L/I;
dth=pi/J;
thj=dth*(0:J);
cth=cos(thj);
vec1=ones(1,J+1);
ri=1+dr*(0:I);
T=T*(4*pi*hw*R)/P;
T=T-(d*d+(ri.*ri)'*vec1-2*d*ri'*cth).^(-0.5);
J=J/2;

% Initialise the various variables required for the program.
Jp=J+1;
dth=pi/J;
thj=dth*(0:J);
sth=sin(thj);
cth=cos(thj);

% Initialise variables for speeding up differential equation construction.
deriv=[0 0 1 0 0
     1/12 -2/3 0 2/3 -1/12
     -1/12 4/3 -5/2 4/3 -1/12
     -1/2 1 0 -1 1/2
      1 -4 6 -4 1];
ri2=ri.^(-2);
ri3=ri.^(-3);
ri4=ri.^(-4);
cotj=cth./sth;
cot2=cotj.*cotj;
sth2=sth.*sth;
tmpa=6+2*sth.^(-2)+cotj.^2;
tmpb=6*cotj+3*cth.*sth.^(-3);
tm1=-2*ri2*dr^2/dth^2;
tm2=ri4*dr^4/dth^4;
```

```
tm3=-2*ri2'*cotj*dr^2/dth;
tm4=-4*ri3*dr^3/dth^2;
tm5=-2*ri4'*cotj*dr^4/dth^3;
tm6=4*ri3'*cotj*dr^3/dth;
tm7=ri4'*tmpa*dr^4/dth^2;
tm8=-ri4'*tmpb*dr^4/dth;
der1=deriv(5,:)'*deriv(1,:);
der2=deriv(3,:)'*deriv(3,:);
der3=deriv(1,:)'*deriv(5,:);
der4=deriv(3,:)'*deriv(2,:);
der5=deriv(2,:)'*deriv(3,:);
der6=deriv(1,:)'*deriv(4,:);
der7=deriv(2,:)'*deriv(2,:);
der8=deriv(1,:)'*deriv(3,:);
der9=deriv(1,:)'*deriv(2,:);

% Initialise matrices for solving distribution.
s=sparse(Ip*Jp,Ip*Jp);
an=zeros(Ip*Jp,1);

l=1;
disp('Constructing s matrix...');
% Boundary conditions at r=R (3.33a).
for j=1:Jp,
  s(l,j)=1;
  l=l+1;
end;

% Boundary condition at theta=0 (3.33c).
s(l,Jp+1)=1;
l=l+1;

% Derivative boundary condition at r=R (3.33b).
for j=2:J,
  s(l,Jp+j)=2+4*dr;
  s(l,2*Jp+j)=-(1+dr);
  an(l)=dr*dr*(-d* sth2(j)*(d*d+1- 2*d*cth(j)).^(-1.5)+sth(j)*(T(1,2*j)-T(1,2*j-2))/dth);
  l=l+1;
end

% Boundary condition at theta=pi (3.33g).
s(l,2*Jp)=1;
l=l+1;
for i=3:I-1,
  % Boundary condition at theta=0 (3.33c).
  iJp=i*Jp;
  s(l,iJp+1)=1;
  l=l+1;
  % Derivative boundary condition at theta=0 (3.33d).
  s(l,iJp+2)=2;
  s(l,iJp+3)=-0.5;
  l=l+1;
  % Navier-Stokes equations (3.32).
  for j=3:J-1,
    matr=der1+tm1(i)*der2+tm2(i)*der3+tm3(i,j)*der4+tm4(i)*der5+tm5(i,j)*der6+tm6(i,j)*der7
                                                    +tm7(i,j)*der8+tm8(i,j)*der9;
    k=iJp-2*Jp+j-2;
    s(l,k:k+4)=matr(1,:);
    k=k+Jp;
```

```matlab
    s(l,k:k+4)=matr(2,:);
    k=k+Jp;
    s(l,k:k+4)=matr(3,:);
    k=k+Jp;
    s(l,k:k+4)=matr(4,:);
    k=k+Jp;
    s(l,k:k+4)=matr(5,:);
    l=l+1;
  end
```
% Derivative boundary condition at theta=pi *(3.33h).*
```matlab
  s(l,iJp+J)=2;
  s(l,iJp+J-1)=-0.5;
  l=l+1;
```
% Boundary condition at theta=pi *(3.33g).*
```matlab
  s(l,iJp+Jp)=1;
  l=l+1;
  if opt,
    home;
    disp(i);
  end
end
```
% Boundary condition at theta=0 *(3.33c).*
```matlab
s(l,I*Jp-J)=1;
l=l+1;
```
% Derivative boundary condition at r=inf *(3.33f).*
```matlab
for j=2:J,
  s(l,I*Jp-Jp+j)=2;
  s(l,I*Jp-2*Jp+j)=-0.5;
  l=l+1;
end
```
% Boundary condition at theta=pi *(3.33g).*
```matlab
s(l,I*Jp)=1;
l=l+1;
```
% Boundary condition at r=inf *(3.33e).*
```matlab
for j=1:Jp,
  s(l,I*Jp+j)=1;
  l=l+1;
end
```

% Solve system.
```matlab
disp('Solving...');
psi=s\an;
```

% Pack vector psi *into matrix* p.
```matlab
p=[];
for i=0:I,
  p=[p psi((i*Jp+1):((i+1)*Jp))];
end
```
% Multiply p *by scaling constants.*
```matlab
p=p'*(gd*R*P)/(4*pi*hw*visc);
```

B.7 StreamV

```matlab
function p=StreamV(L,d,R,hw,P,T,opt);
```
% Calculates the streamfunction given the temperature distribution on the surface of the bubble taking account
% of the nonlinear dependence of the surface tension on temperature and the temperature dependence of
% viscosity.
% p = StreamV(L,d,R,hw,P,T,opt); returns the streamfunction p. L *is the distance the outer wall is away,* d *is*

% the distance the heat source is away, R *is the radius of the bubble,* hw *is the thermal conductivity of the*
% water, P *is the power,* T *is the temperature distribution, and* opt *is 1 if a progress indicator is required.*

% Check if opt *had been passed as an argument, and set it to 0 if it has not.*
if nargin<7,
  opt=0;
end

% Normalise variables to units where R=1.
L=L/R;
d=d/R;

% Determine I *and* J *variables from size of* T.
[Ip Jp]=size(T);
I=Ip-1;
J=Jp-1;

% Calculate viscosity and temperature coefficient of surface tension.
for j=1:J/2+1,
  vis(:,j)=visc(T(:,j*2-1));
  gd(j)=dtension(T(1,j*2-1));
end

% Change T *to get unscaled correction.*
dr=L/I;
dth=pi/J;
thj=dth*(0:J);
cth=cos(thj);
vec1=ones(1,J+1);
ri=1+dr*(0:I)';
T=T*(4*pi*hw*R)/P;
T=T-(d*d+(ri.*ri)*vec1-2*d*ri*cth).^(-0.5);
J=J/2;
Jp=J+1;

% Initialise the various variables required for the program.
dth=pi/J;
thj=dth*(0:J);
sth=sin(thj);
cth=cos(thj);
sth2=sth.*sth;
% Initialise variables for speeding up differential equation construction.
onr=ones(Ip,1);
onz=ones(1,Jp);
deriv=[0 0 1 0 0
     1/12 -2/3 0 2/3 -1/12
     -1/12 4/3 -5/2 4/3 -1/12
     -1/2 1 0 -1 1/2
     1 -4 6 -4 1];
der1=deriv(5,:)'*deriv(1,:);
der2=deriv(3,:)'*deriv(3,:);
der3=deriv(1,:)'*deriv(5,:);
der4=deriv(4,:)'*deriv(1,:);
der5=deriv(3,:)'*deriv(2,:);
der6=deriv(2,:)'*deriv(3,:);
der7=deriv(1,:)'*deriv(4,:);
der8=deriv(3,:)'*deriv(1,:);
der9=deriv(2,:)'*deriv(2,:);
der10=deriv(1,:)'*deriv(3,:);

```matlab
der11=deriv(2,:)'*deriv(1,:);
der12=deriv(1,:)'*deriv(2,:);
tma1=zeros(Ip,Jp);
tma2=tma1;
tma3=tma1;
tma4=tma1;
tma5=tma1;
for i=3:I-1,
  for j=3:J-1,
    tma1(i,j)=sum(sum(der11.*vis(i-2:i+2,j-2:j+2)));
    tma2(i,j)=sum(sum(der12.*vis(i-2:i+2,j-2:j+2)));
    tma3(i,j)=sum(sum(der8.*vis(i-2:i+2,j-2:j+2)));
    tma4(i,j)=sum(sum(der10.*vis(i-2:i+2,j-2:j+2)));
    tma5(i,j)=sum(sum(der9.*vis(i-2:i+2,j-2:j+2)));
  end
end

ri1=ri.^(-1);
ri2=ri.^(-2);
ri3=ri.^(-3);
ri4=ri.^(-4);
cotj=cth./sth;
cot2=cotj.*cotj;
tmpa=6+2*sth.^(-2)+cotj.^2;
tmpb=6*cotj+3*cth.*sth.^(-3);

rij=ri*onz;
tm1=1/dr^4;
tm2=-2*ri2/(dr^2*dth^2);
tm3=ri4/dth^4;
tm4=tma1/dr^4;
tm5=(-2*ri2*cotj/(dr^2*dth)).*vis+(ri2*onz).*tma2/(dr*dth)^2;
tm6=(-4*(ri3*onz)/(dr*dth^2)).*vis+(ri2*onz).*tma1/(dr*dth)^2;
tm7=(-2*ri4*cotj/dth^3).*vis+(ri4*onz).*tma2/dth^4;
tm8=-(ri2*onz).*tma4/(dr*dth)^2-(ri2*cotj).*tma2/(dr^2*dth)-2*(ri1*onz).*tma1/dr^3+(onr*sth).*tma3/dr^4;
tm9=(4*ri3*cotj/(dr*dth)).*vis-(ri2*cotj).*tma1/(dr^2*dth)-4*(ri3*onz).*tma2/(dr*dth^2)
                                                            +4*(ri2*onz).*tma5/(dr*dth).^2;
tm10=(ri4*tmpa/dth^2).*vis-2*(ri4*cotj).*tma2/dth^3+(ri4*onz).*tma4/dth^4-(ri2*onz).*tma3/(dr*dth)^2
                                                            -2*(ri2*onz).*tma1/(dr*dth^2);
tm11=2*(ri3*onz).*tma4/(dr*dth^2)-2*(ri1*onz).*tma3/dr^3-2*(ri2*cotj).*tma5/(dr^2*dth)
                                                            +2*(ri3*cotj).*tma2/(dr*dth)+2*(ri2*onz).*tma1/dr^2;
tm12=(-ri4*tmpb/dth).*vis-(ri4*cotj).*tma4/dth^3+(ri2*cotj).*tma3/(dr^2*dth)-6*(ri3*onz).*tma5/(dr*dth^2)
                                                            +2*(ri3*cotj).*tma1/(dr*dth)+(ri4*((2+5*sth.^2).*sth.^(-2))).*tma2/dth^2;

% Initialise matrices for solving distribution.
s=sparse(Ip*Jp,Ip*Jp);
an=zeros(Ip*Jp,1);

l=1;
disp('Constructing s matrix...');
% Boundary conditions at r=R (3.33a).
for j=1:Jp,
  s(l,j)=1;
  l=l+1;
end;

% Boundary condition at theta=0 (3.33c).
s(l,Jp+1)=1;
l=l+1;
```

```matlab
% Derivative boundary condition at r=R (3.33b).
for j=2:J,
  s(l,Jp+j)=2+4*dr;
  s(l,2*Jp+j)=-(1+dr);
  an(l)=dr^2*gd(j)*(-d* sth2(j)*(d*d+1- 2*d*cth(j))).^(-1.5)+sth(j)*(T(1,2*j)-T(1,2*j-2))/dth);
  l=l+1;
end

% Boundary condition at theta=pi (3.33g).
s(l,2*Jp)=1;
l=l+1;
for i=3:I-1,
  % Boundary condition at theta=0 (3.33c).
  iJp=(i-1)*Jp;
  s(l,iJp+1)=1;
  l=l+1;
  % Derivative boundary condition at theta=0 (3.33d).
  s(l,iJp+2)=2;
  s(l,iJp+3)=-0.5;
  l=l+1;
  % Navier-Stokes equations (3.37).
  for j=3:J-1,
    matr=vis(i,j)*(der1*tm1+der2*tm2(i)+der3*tm3(i))+der4*tm4(i,j)+der5*tm5(i,j)+der6*tm6(i,j)
                 +der7*tm7(i,j)+der8*tm8(i,j)+der9*tm9(i,j)+der10*tm10(i,j)+der11*tm11(i,j)+der12*tm12(i,j);
    k=iJp-2*Jp+j-2;
    s(l,k:k+4)=matr(1,:);
    k=k+Jp;
    s(l,k:k+4)=matr(2,:);
    k=k+Jp;
    s(l,k:k+4)=matr(3,:);
    k=k+Jp;
    s(l,k:k+4)=matr(4,:);
    k=k+Jp;
    s(l,k:k+4)=matr(5,:);
    l=l+1;
  end
  % Derivative boundary condition at theta=pi (3.33h).
  s(l,iJp+J)=2;
  s(l,iJp+J-1)=-0.5;
  l=l+1;
  % Boundary condition at theta=pi (3.33g).
  s(l,iJp+Jp)=1;
  l=l+1;
  if opt,
    home;
    disp(i);
  end
end
% Boundary condition at theta=0 (3.33c).
s(l,I*Jp-J)=1;
l=l+1;
% Derivative boundary condition at r=inf (3.33f).
for j=2:J,
  s(l,I*Jp-Jp+j)=2;
  s(l,I*Jp-2*Jp+j)=-0.5;
  l=l+1;
end
% Boundary condition at theta=pi (3.33g).
```

```
s(l,I*Jp)=1;
l=l+1;
```
% Boundary condition at r=inf *(3.33e).*
```
for j=1:Jp,
  s(l,I*Jp+j)=1;
  l=l+1;
end
```

% Solve system.
```
disp('Solving...');
psi=s\an;
```

% Pack vector psi *into matrix* p*.*
```
p=[];
for i=0:I,
  p=[p psi((i*Jp+1):((i+1)*Jp))];
end
```
% Multiply p *by scaling constants.*
```
p=p'*(R*P)/(4*pi*hw);
```
****

Functions used by StreamV.m

```
function d=dtension(T);
```
% Gives the thermal coefficient of surface tension of water at temperature T*.*
```
T=T+273.15;
X=(647.126-T)/647.126;
d=-0.2358*(1.256*X.^0.256-1.41*X.^1.256)/647.126;
```

```
function mu=visc(T);
```
% Gives the viscosity of water at temperature T*. Interpolates from a table.*
```
w=[273.15 1.750e-3;  275  1.652e-3;  280  1.422e-3;  285  1.225e-3;  290  1.080e-3;  295  9.59e-4
 300  8.55e-4;  305  7.69e-4;  310  6.95e-4;  315  6.31e-4;  320  5.77e-4;  325  5.28e-4;  330  4.89e-4
 335  4.53e-4;  340  4.20e-4;  345  3.89e-4;  350  3.65e-4;  355  3.43e-4;  360  3.24e-4;  365  3.06e-4
 370  2.89e-4;  373.15 2.79e-4;  375  2.74e-4;  380  2.60e-4;  385  2.48e-4;  390  2.37e-4;  400  2.17e-4
 410  2.00e-4;  420  1.85e-4;  430  1.73e-4;  440  1.62e-4;  450  1.52e-4;  460  1.43e-4;  470  1.36e-4
 480  1.29e-4;  490  1.24e-4;  500  1.18e-4;  510  1.13e-4;  520  1.08e-4;  530  1.04e-4;  540  1.01e-4
 550  0.97e-4;  560  0.94e-4;  570  0.91e-4;  580  0.88e-4;  590  0.84e-4;  600  0.81e-4;  610  0.77e-4
 620  0.72e-4;  625  0.70e-4;  630  0.67e-4;  635  0.64e-4;  640  0.59e-4;  645  0.54e-4;  647.3 0.45e-4];
w(:,2)=log(w(:,2));
[I J]=size(T);
T=T+273.15;
for i=1:I,
  for j=1:J,
    in=min([sum(w(:,1)<T(i,j)) 54]);
    mu(i,j)=w(in,2)+(w(in+1,2)-w(in,2))*(T(i,j)-w(in,1))/(w(in+1,1)-w(in,1));
  end
end
mu=exp(mu);
```

B.8 PStream

```
function p=PStream(I,L,hw,hg,P,g,nu,drho,opt);
```
% Calculates the streamfunction for convection from a point heat source in a cylinder of height and radius L*.*
% p = PStream(I,L,hw,hg,P,g,nu,drho,opt); *returns the streamfunction* p*.* I *is the number of intervals in the* R
% and z *directions,* L *is the height and radius of the container,* hw *is the thermal conductivity of the water,* hg *%*
is the thermal conductivity of the glass, P *is the power of the point heat source,* g *is the acceleration of*
% gravity, nu *is the viscosity,* drho *is the thermal coefficient of density, and* opt *is 1 if a progress indicator is*

```
% Check if opt had been passed as an argument, and set it to 0 if it has not.
if nargin<9,
  opt=0;
end

% Initialise the various variables required for the program.
J=I;
dr=L/I;
dz=L/J;
Ip=I+1;
Jp=J+1;
ri=dr*(0:I)';
zj=dz*(0:J);
onr=ones(Ip,1);
onz=ones(1,Jp);
an1=dr^4*(ri.^5*onz).*(ri.^2*onz+onr*zj.^2).^(-1.5);

% Initialise variables for speeding up differential equation construction.
deriv=[0 0 1 0 0
     1/12 -2/3 0 2/3 -1/12
     -1/12 4/3 -5/2 4/3 -1/12
     -1/2 1 0 -1 1/2
     1 -4 6 -4 1];
tm1=-ri.^3;
tm2=-2*ri.^3*dr^2/dz^2;
tm3=-ri.^3*dr^4/dz^4;
tm4=2*ri.^2*dr;
tm5=2*ri.^2*dr^3/dz^2;
tm6=-3*ri*dr^2;
tm7=3*dr^3;
der1=deriv(5,:)'*deriv(1,:);
der2=deriv(3,:)'*deriv(3,:);
der3=deriv(1,:)'*deriv(5,:);
der4=deriv(4,:)'*deriv(1,:);
der5=deriv(2,:)'*deriv(3,:);
der6=deriv(3,:)'*deriv(1,:);
der7=deriv(2,:)'*deriv(1,:);

% Initialise matrices for solving distribution.
s=sparse(Ip*Jp,Ip*Jp);
an=zeros(Ip*Jp,1);

l=1;
disp('Constructing s matrix...');

% Boundary conditions at R=0 (3.45a).
for j=1:Jp,
  s(l,j)=1;
  l=l+1;
end;
% Boundary condition at z=0 (3.45b).
s(l,Jp+1)=1;
l=l+1;
% Derivative boundary conditions at R=0 (3.45c).
for j=2:J,
  s(l,Jp+j)=2;
  s(l,2*Jp+j)=-0.5;
```

```matlab
  l=l+1;
end
% Boundary conditions at z=inf (3.45b).
s(l,2*Jp)=1;
l=l+1;
for i=3:I-1,
  iJp=(i-1)*Jp;
  % Boundary condition at z=0 (3.45b).
  s(l,iJp+1)=1;
  l=l+1;
  % Derivative boundary condition at z=0 (3.45d).
  s(l,iJp+2)=2;
  s(l,iJp+3)=-0.5;
  l=l+1;
  for j=3:J-1,
    matr=der1*tm1(i)+der2*tm2(i)+der3*tm3(i)+der4*tm4(i)+der5*tm5(i)+der6*tm6(i)+der7*tm7;
    k=iJp-2*Jp+j-2;
    s(l,k:k+4)=matr(1,:);
    k=k+Jp;
    s(l,k:k+4)=matr(2,:);
    k=k+Jp;
    s(l,k:k+4)=matr(3,:);
    k=k+Jp;
    s(l,k:k+4)=matr(4,:);
    k=k+Jp;
    s(l,k:k+4)=matr(5,:);
    an(l)=an1(i,j);
    l=l+1;
  end
  % Derivative boundary condition at z=inf (3.45d).
  s(l,iJp+J)=2;
  s(l,iJp+J-1)=-0.5;
  l=l+1;
  % Boundary condition at z=inf (3.45b).
  s(l,iJp+Jp)=1;
  l=l+1;
  if opt,
    home;
    disp(i);
  end
end
% Boundary condition at z=0 (3.45b).
s(l,I*Jp-J)=1;
l=l+1;
% Derivative boundary condition at R=inf (3.45c).
for j=2:J,
  s(l,I*Jp-Jp+j)=2;
  s(l,I*Jp-2*Jp+j)=-0.5;
  l=l+1;
end
% Boundary condition at z=inf (3.45b).
s(l,I*Jp)=1;
l=l+1;
% Boundary condition at R=inf (3.45a).
for j=1:Jp,
  s(l,I*Jp+j)=1;
  l=l+1;
end
```

```
% Solve system.
disp('Solving...');
psi=s\an;

% Pack vector psi into matrix p.
p=[];
for i=0:I,
  p=[p psi((i*Jp+1):((i+1)*Jp))];
end

% Multiply p by scaling constants.
p=p'*P*g/(2*pi*(hw+hg))*drho/nu;
```

B.9 PStreamV

```
function p=PStreamV(I,L,hw,hg,P,g,opt);
% Calculates the streamfunction for convection from a point heat source in a cylinder of height and radius L,
% taking into account the thermal variation in viscosity and the nonlinear dependence of density on
% temperature.
% p = PStreamV(I,L,hw,hg,P,g,opt);  returns the streamfunction p.  I is the number of intervals in the R and z
% directions, L is the height and radius of the container, hw is the thermal conductivity of the water, hg is the
% thermal conductivity of the glass, P is the power of the point heat source, g is the acceleration of gravity,
% and opt is 1 if a progress indicator is required.

% Check if opt had been passed as an argument, and set it to 0 if it has not.
if nargin<7,
  opt=0;
end

% Initialise the various variables required for the program.
J=I;
dr=L/I;
dz=L/J;
Ip=I+1;
Jp=J+1;
ri=dr*(0:I)';
zj=dz*(0:J);
onr=ones(Ip,1);
onz=ones(1,Jp);
an1=dr^4*(ri.^5*onz).*(ri.^2*onz+onr*zj.^2).^(-1.5);
T=25+P/(2*pi*(hw+hg))*(ri.^2*onz+onr*zj.^2).^(-0.5);
vis=visc(T);
an1=an1.*ddensity(T);
% Initialise variables for speeding up differential equation construction.
deriv=[0 0 1 0 0
     1/12 -2/3 0 2/3 -1/12
    -1/12 4/3 -5/2 4/3 -1/12
    -1/2 1 0 -1 1/2
     1 -4 6 -4 1];
der1=deriv(5,:)'*deriv(1,:);
der2=deriv(3,:)'*deriv(3,:);
der3=deriv(1,:)'*deriv(5,:);
der4=deriv(4,:)'*deriv(1,:);
der5=deriv(3,:)'*deriv(2,:);
der6=deriv(2,:)'*deriv(3,:);
der7=deriv(1,:)'*deriv(4,:);
der8=deriv(3,:)'*deriv(1,:);
der9=deriv(2,:)'*deriv(2,:);
```

```
der10=deriv(1,:)'*deriv(3,:);
der11=deriv(2,:)'*deriv(1,:);
der12=deriv(1,:)'*deriv(2,:);
tma1=zeros(Ip,Jp);
tma2=tma1;
tma3=tma1;
tma4=tma1;
tma5=tma1;
for i=3:I-1,
  for j=3:J-1,
    tma1(i,j)=sum(sum(der11.*vis(i-2:i+2,j-2:j+2)));
    tma2(i,j)=sum(sum(der12.*vis(i-2:i+2,j-2:j+2)));
    tma3(i,j)=sum(sum(der8.*vis(i-2:i+2,j-2:j+2)));
    tma4(i,j)=sum(sum(der10.*vis(i-2:i+2,j-2:j+2)));
    tma5(i,j)=sum(sum(der9.*vis(i-2:i+2,j-2:j+2)));
  end
end
rij=ri*onz;
tm1=ri.^3;
tm2=2*ri.^3;
tm3=ri.^3;
tm4=-2*dr*rij^2.*vis+rij^3.*tma1;
tm5=rij^3.*tma2;
tm6=-2*dr*rij.^2.*vis+rij^3.*tma1;
tm7=rij^3.*tma2;
tm8=3*dr^2*rij.*vis-2*dr*rij.^2.*tma1+rij.^3.*(tma3-tma4);
tm9=-dr*rij.^2.*tma2+4*rij.^3.*tma5;
tm10=-dr*rij.^2.*tma1+rij.^3.*(tma4-tma3);
tm11=-3*dr^3*vis+2*dr^2*rij.*tma1+dr*rij.^2.*(tma4-tma3);
tm12=-2*dr*rij.^2.*tma5;

% Initialise matrices for solving distribution.
s=sparse(Ip*Jp,Ip*Jp);
an=zeros(Ip*Jp,1);

l=1;
disp('Constructing s matrix...');
% Boundary conditions at R=0 (3.45a).
for j=1:Jp,
  s(l,j)=1;
  l=l+1;
end;
% Boundary condition at z=0 (3.45b).
s(l,Jp+1)=1;
l=l+1;
% Derivative boundary conditions at R=0 (3.45c).
for j=2:J,
  s(l,Jp+j)=2;
  s(l,2*Jp+j)=-0.5;
  l=l+1;
end
% Boundary conditions at z=inf (3.45b).
s(l,2*Jp)=1;
l=l+1;
for i=3:I-1,
  iJp=(i-1)*Jp;
  % Boundary condition at z=0 (3.45b).
  s(l,iJp+1)=1;
  l=l+1;
```

```matlab
% Derivative boundary condition at z=0 (3.45d).
 s(l,iJp+2)=2;
 s(l,iJp+3)=-0.5;
 l=l+1;
 for j=3:J-1,
   matr=vis(i,j)*(der1*tm1(i)+der2*tm2(i)+der3*tm3(i))+der4*tm4(i,j)+der5*tm5(i,j)+der6*tm6(i,j)
               +der7*tm7(i,j)+der8*tm8(i,j)+der9*tm9(i,j)+der10*tm10(i,j)+der11*tm11(i,j)+der12*tm12(i,j);
   k=iJp-2*Jp+j-2;
   s(l,k:k+4)=matr(1,:);
   k=k+Jp;
   s(l,k:k+4)=matr(2,:);
   k=k+Jp;
   s(l,k:k+4)=matr(3,:);
   k=k+Jp;
   s(l,k:k+4)=matr(4,:);
   k=k+Jp;
   s(l,k:k+4)=matr(5,:);
   an(l)=an1(i,j);
   l=l+1;
 end
% Derivative boundary condition at z=inf (3.45d).
 s(l,iJp+J)=2;
 s(l,iJp+J-1)=-0.5;
 l=l+1;
% Boundary condition at z=inf (3.45b).
 s(l,iJp+Jp)=1;
 l=l+1;
 if opt,
   home;
   disp(i);
 end
end
% Boundary condition at z=0 (3.45b).
s(l,I*Jp-J)=1;
l=l+1;
% Derivative boundary condition at R=inf (3.45c).
for j=2:J,
  s(l,I*Jp-Jp+j)=2;
  s(l,I*Jp-2*Jp+j)=-0.5;
  l=l+1;
end
% Boundary condition at z=inf (3.45b).
s(l,I*Jp)=1;
l=l+1;
% Boundary condition at R=inf (2.45a).
for j=1:Jp,
  s(l,I*Jp+j)=1;
  l=l+1;
end

% Solve system.
disp('Solving...');
psi=s\an;

% Pack vector psi into matrix p.
p=[];
for i=0:I,
  p=[p psi((i*Jp+1):((i+1)*Jp))];
end
```

94

% Multiply p *by scaling constants.*
p=p*g;
****

Functions used by PStreamV.m

function d=ddensity(T);
% Gives the thermal coefficient of density for water at temperature T.
d=(16.945176-2*7.9870401E-3*T-3*46.170461E-6*T.^2+4*105.56302E-9*T.^3
                                    -5*280.54253E-12*T.^4)./(1+16.879850E-3*T);
d=d-16.879850E-3*(999.83952+16.945176*T-7.9870401E-3*T.^2-46.170461E-6*T.^3+105.56302E-9*T.^4
                                    -280.54253E-12*T.^5)./(1+16.879850E-3*T).^2;

References

[1] A. Ashkin, J. Dziedzic, J. Bjorkholm and C. Chu, "Observation of a single beam gradient force optical trap for dielectric particles", *Optics Letters*, **11** (5), 288-290, 1986.

[2] A. Ashkin and J. Dziedzic, "Optical trapping and manipulation of viruses and bacteria", *Science*, **235**, 1517-1520, 1987.

[3] A. Ashkin, J. Dziedzic and T. Yamane, "Optical trapping and manipulation of single cells using infrared laser beams", *Nature*, **330**, 769-771, 1987.

[4] K. Schütze and A. Clement-Sengewald, "Catch and move - cut or fuse", *Nature*, **368**, 667-669, 1994.

[5] K. Sasaki, M. Koshioka, H. Misawa, N. Kitamura and H. Masuhara, "Optical trapping of a metal particle and a water droplet by a scanning laser beam", *Appl. Phys. Lett.*, **60** (7), 807-809, 1992.

[6] S. Sato, M. Ishigure and H. Inaba, "Optical trapping and rotational manipulation of microscopic particles and biological cells using higher-order mode Nd:YAG laser beams", *Electron. Lett.*, **27** (20), 1831-1832, 1991.

[7] H. He, N. R. Heckenberg and H. Rubinsztein-Dunlop, "Optical particle trapping with higher-order doughnut beams produced using high efficiency computer generated holograms", *J. Mod. Optics*, **42** (1), 217-223, 1995.

[8] K. T. Gahagan and G. A. Swartzlander, Jr., "Optical vortex trapping of particles", *Opt. Lett.*, **21** (11), 827-829, 1996.

[9] M. E. J. Friese, T. A. Nieminen, H. Rubinsztein-Dunlop and N. R. Heckenberg, "Angular momentum transfer from a circularly polarised Gaussian laser beam", QELS/CLEO '97 Conference, Baltimore, USA, QHD34, 108-109, May 18-23, 1997.

[10] H. Rubinsztein-Dunlop, T. A. Nieminen, M. E. J. Friese and N. R. Heckenberg, "Optical trapping of absorbing particles", to appear in *Adv. in Quantum Chemistry*.

[11] S. Sato, Y. Harada and Y. Waseda, "Optical trapping of microscopic metal particles", *Optics Letters*, **19** (22), 1807-1809, 1994.

[12] H. Misawa, M Koshioka, K. Sasaki, N. Kitamura and H. Masuhara, "Three-dimensional

optical trapping and laser ablation of a single polymer latex particle in water", *J. Appl. Phys.*, **70** (7), 3829-3836, 1991.

[13]   C. d'Helon, Optical Tweezers, IVH thesis, Physics Department, The University of Queensland, 1992.

[14]   G. Forgo, M. Ragnetti and A. Stübbe, "Styrene-acrylate copolymers as toner resins: correlations between molecular structure, viscoelastic behavior, and fusing properties", *J. Imag. Sci. Tech.*, **37** (2), 176-186, 1993.

[15]   Y. Iida, K. Okuyama and K. Sakurai, "Boiling nucleation on a very small film heater subject to extremely rapid heating", *Int. J. Heat Mass Transfer*, **37** (17), 2771-2780, 1994.

[16]   M. Volmer., Chapter 4, *Kinetik der Phasenbildung*, Steinkopff, Dresden and Leipzig, 1939.

[17]   W. Porteous and M. Blander, "Limits of superheat and explosive boiling of light hydrocarbons, halocarbons, and hydrocarbon mixtures", *AIChE J.*, **21** (3), 560-566, 1975.

[18]   M. Blander and J. L. Katz, "Bubble nucleation in liquids", *AIChE J.*, **21** (5), 833-848, 1975.

[19]   N. B. Vargaftik, B. N. Volkov, and L. D. Voljak, "International tables of the surface tension of water", *J. Phys. Chem. Ref. Data*, **12** (3), 817-820, 1983.

[20]   G. R. Somayajulu, "A generalised equation for surface tension from the triple point to the critical point", *International Journal of Thermophysics*, **9** (4), 559-566, 1988.

[21]   R. C. Tolman, "The effect of droplet size on surface tension", *J. Chem. Phys.*, **17** (3), 333-337, 1949.

[22]   D. Jayaraaman, C. Subramanian, P. Ramasamy, "Effect of curvature-dependent surface tension on nucleation", *Journal of Materials Science Letters*, **8**, 1399-1401, 1989.

[23]   D. R. Lide, *CRC Handbook of Chemistry and Physics*, CRC Press Inc., Boca Raton, 1996.

[24] A. Saul and W. Wagner, "International equations for the saturation properties of ordinary water substance", *J. Phys. Chem. Ref. Data*, **16** (4), 893-901, 1987.

[25]   G. R. Somayajulu, "New equations for enthalpy of vaporisation from the triple point to the critical point", *International Journal of Thermophysics*, **9** (4), 567-575, 1988.

[26] G. S. Kell, "Density, thermal expansivity, and compressibility of liquid water from 0°C to 150°C: correlations and tables for atmospheric pressure and saturation reviewed and expressed on 1968 temperature scale", *J. Chem. Eng. Data*, **20** (1), 97-105, 1975.

[27] F. P. Incropera and D. P. De Witt, Appendix A, *Fundamentals of Heat and Mass Transfer*, Wiley, New York, 1996.

[28] V. P. Skripov and P. A. Pavlov, "Explosive boiling of liquids and fluctuation nucleus formation", *High Temp.*, **8**, 782-787, 1970.

[29] C. T. Avedisan, "The homogeneous nucleation limits of liquids", *J. Phys. Chem. Ref. Data.*, **14** (3), 695-729, 1985.

[30] *Material Safety Data Sheet*, Toshiba Australia Pty Ltd, 1994.

[31] L. M. Wyatt and U. R. Lenel, *Fulmer Materials Optimiser*, Osco Ltd., Berkshire, 1979.

[32] Matlab for Windows Version 4.2b, The Mathworks Inc., 1994.

[33] S. G. Bankoff, "Ebullition from solid surfaces in the absence of a pre-existing gaseous phase", *Trans. ASME*, **79**, 735-740, 1957.

[34] G. R. Moore, "Vaporisation of superheated drops in liquids", *AIChE J.*, **5** (4), 458-466, 1959.

[35] R. E. Apfel, "Vapour nucleation at a liquid-liquid interface", *J. Chem. Phys.*, **54** (1), 62-63, 1971.

[36] T. J. Jarvis, M. D. Donohue and J. L. Katz, "Bubble nucleation mechanisms of liquid droplets superheated in other liquids", *J. Colloid Interf. Sci.*, **50** (2), 359-368, 1975.

[37] A. V. Hershey, "Ridges in a liquid surface due to the temperature dependence of surface tension", *Physical Review*, **56**, 204-204, 1939.

[38] H. Bénard, "Les tourbillons cellulaires dans une nappe liquide transportant de la chaleur par convection en régime permanent", *Ann. Chem. Phys.*, **23**, 62-144, 1901.

[39] Lord Rayleigh, "On the convection currents in a horizontal layer of fluid when the higher temperature is on the under side", *Phil. Mag.*, **32**, 529-546, 1916.

[40] A. R. Low and D. Brunt, "Instability of viscous fluid motion", *Nature*, **115**, 299-301, 1925.

[41] H. Jeffreys, "The surface elevation in cellular convection", *Quart. J. Mech. Appl. Math.*, **4** (3), 283-288, 1951.

[42] M. J. Block, "Surface tension as the cause of Bénard cells and surface deformation in a liquid film", *Nature*, **178**, 650-651, 1956.

[43] J. R. A. Pearson, "On convection cells induced by surface tension", *J. Fluid. Mech.*, **4**, 489-500, 1958.

[44] N. O. Young, J. S. Goldstein, and M. J. Block, "The motion of bubbles in a vertical

temperature gradient", *J. Fluid Mech.*, **6**, 350-356, 1959.

[45] R. S. Subramanian, "Slow migration of a gas bubble in a thermal gradient", *AIChE J.*, **27** (4), 646-654, 1981.

[46] R. M. Merritt, Term Project Report, Chemical Engineering Analysis Course (unpublished), Department of Chemical Engineering, Clarkson University, 1984.

[47] N. Shankar and R. S. Subramanian, "The Stokes motion of a gas bubble due to interfacial tension gradients at low to moderate Marangoni numbers", *J. Colloid Interf. Sci.*, **123** (2), 512-522, 1988.

[48] R. Balasubramaniam and J. E. Lavery, "Numerical simulation of thermocapillary bubble migration under microgravity for large Reynolds and Marangoni numbers", *Numerical Heat Transfer A*, **16**, 175-187, 1989.

[49] M. D. Levan and J. Newmann, "The effect of surfactant on the terminal and interfacial velocities of a bubble or drop", *AIChE J.*, **22** (4), 695-701, 1976.

[50] A. Erdélyi, Volume 1, Section 3.15.1, *Higher Transcendental Functions*, McGraw-Hill, New York, 1953.

[51] C. Yih, Chapter 8, Part 7, *Fluid Mechanics*, West River Press, Ann Arbor, 1977.